A Weak Lensing Study of Dark Matter Halos

by

Laura C. Parker

A thesis
presented to the University of Waterloo
in fulfilment of the
thesis requirement for the degree of
Doctor of Philosophy
in
Physics

Waterloo, Ontario, Canada, 2005

I hereby declare that I am the sole author of this thesis.

I authorize the University of Waterloo to lend this thesis to other institutions or individuals for the purpose of scholarly research.

I further authorize the University of Waterloo to reproduce this thesis by photocopying or by other means, in total or in part, at the request of other institutions or individuals for the purpose of scholarly research.

Abstract

Gravitational lensing can be used to directly probe the quantity and distribution of dark matter, thus making it a powerful tool in astrophysics. In this thesis, I introduce the basics of gravitational lensing, and in particular weak gravitational lensing. Weak lensing is a statistical tool which allows the study of ensemble-averaged properties for a population of objects. I discuss two observational projects that use weak lensing to map dark matter distributions on different scales. The first project is a study of the mass distribution and mass-to-light ratios of galaxy groups. The second is a galaxy-galaxy lensing study of galaxy-sized dark matter halos.

I find that the mass-to-light ratio for a sample of galaxy groups is independent of radius, but is a function of the halo mass. This may indicate that groups of mass $\sim 10^{13}$ $M_{\odot}$ mark the divide between the actively star forming field environment, and the passively evolving cluster regime. Our study of galaxy halos using early data from the Canada-France-Hawaii Telescope Legacy Survey (CFHTLS) allows us to estimate the characteristic velocity dispersion for galaxy halos at a redshift of $z \sim 0.3$. We also present evidence that galaxy dark matter halos may be elliptical rather than spherical. Future galaxy lensing results from the final CFHTLS data should allow us to determine accurately the dark matter mass profile and halo shape, thus providing important constraints on dark matter properties.

Acknowledgements

I would like to acknowledge the help and guidance of my supervisor, Dr. Michael Hudson. I would also like to thank Henk Hoekstra for showing me the basics of weak lensing analysis, and for his willingness to answer all of my questions and concerns. In addition, I would like to recognize a few special teachers whose confidence in me has been invaluable, particularly Mary Casey, Jean Godin and Dr. Robert Hawkes.

Finally, I would like to thank my friends and family for their continuing support and encouragement. Without them, this work would not have been possible.

Contents

List of Figures

List of Tables

Chapter 1

Introduction

> *Isn't it splendid to think of all the things there are to find out about? It just makes me feel glad to be alive–it's such an interesting world. It wouldn't be half so interesting if we know all about everything, would it? There'd be no scope for imagination then, would there?*
>
> — Lucy Maud Montgomery (Anne of Green Gables)

Our universe is indeed an exciting and mysterious place. While we have slowly been accumulating knowledge of the cosmos for millennia, an incredible amount of progress has taken place in the last century. We now know that we live on a planet in a massive galaxy called the Milky Way, which is only one of many billions of galaxies in this universe. We understand much of the history of the universe in general terms, but there are still many details missing, perhaps most importantly the details of galaxy and large scale structure formation. Understanding these aspects of the universe requires both observational

and theoretical work, as well as detailed numerical simulations to bridge the gap between.

Understanding structures and their formation histories is one of the fundamental goals of modern astrophysics. It has become apparent in the last few decades that the mass in the universe is largely unseen in the form of some mysterious “dark matter”. The exact nature of this component of the universe remains elusive, but slowly we are gleaning details of some of its properties. Structure formation greatly depends on the amount and the distribution of dark matter, as well as its relation to the luminous matter we observe. Understanding the distribution of dark matter in the universe will help us to understand the past and future of the cosmos.

This thesis will introduce the topic of dark matter and then provide details of how it can be detected and studied observationally with weak gravitational lensing.

1.1 State of the Art Cosmology

In the last 50 years, our understanding of cosmology has rapidly increased, benefiting greatly from the discovery of the Cosmic Microwave Background (CMB) radiation in the 1960’s, new ground and space-based telescopes with the ability to peer back billions of years, and a better theoretical footing built upon General Relativity.

Our universe appears to fit a basic model which is spatially flat and homogeneous and isotropic on large scales. It has become evident that we live in

Universe dominated by dark or unseen components. In fact, the normal, baryonic matter of which we, and everything we see, are made accounts for only roughly 4% of the energy density of the universe. There is also a large dark matter component which is still not understood, though it is believed to consist of weakly interacting fundamental particles (as will be discussed in Section 1.3). The final, and largest, piece in the energy budget of the universe is dark energy. This component is the most poorly understood, but appears to be an "anti-gravity" like force which could be a vacuum energy density. Einstein allowed for this type of component in his theory of General Relativity, and called it the cosmological constant. He included this term in order to satisfy the static model of the universe, but once it was discovered that the universe was in fact expanding he claimed that it was his biggest blunder (Gamow, 1970). It is still not known whether this component is truly a cosmological constant or whether it is time-varying. This is an extremely active area of both theoretical and observational research.

In addition to cosmological parameters, a key aspect of modern cosmology is an understanding of structure growth from stars and galaxies to the large scale filamentary structure of the universe. There are two principal ways in which structures could be envisioned to form. Either small structures are formed first and join together to form larger structures hierarchically, or alternatively, large structures form first and then fragment into the small objects we see in the universe today. All the current evidence, as we will discuss, points to a hierarchical picture for structure formation, sometimes referred to as the Cold Dark Matter (CDM) model.

1.1.1 Introduction to Parameters

Our universe originated from a hot big bang and has evolved from a nearly isotropic and homogeneous beginning. The large-scale structure of the universe– galaxies, clusters, and voids– represents the deviations from this overall homogeneity and isotropy. These structures originate from primordial fluctuations that grow with time as a result of gravitational instability. Determining the value of the cosmological parameters, and the correct model of large-scale structure formation, is the most important challenge for cosmology.

With the recent advancements in observational cosmology we now have a fairly precise cosmological model which is constrained with a number of basic parameters. These are outlined in Table 1.1 and we refer to them throughout the thesis. Many observations are now consistent with our universe containing a positive vacuum energy density, but the mechanism that generates this energy is not know. There are many theories which try to explain dark energy, but many of them overestimate the energy density by tens of orders of magnitude. There does not appear, at present, to be a natural solution to the dark energy problem and thus it may require the introduction of new physics.

1.1.2 Recent Results

There are many techniques employed to estimate cosmological parameters, and they each come with their own degeneracies. For example, some techniques are degenerate in the Ω_Λ-Ω_m plane, but if two different measurements are degenerate in these two parameters in different ways then their results can be combined

Symbol	Name	Description
H_0	Hubble constant	Describes the current expansion rate of the universe, in units of km s^{-1} Mpc^{-1}
ρ_c	Critical Density	Density required to make the universe spatially flat $\frac{3H_0^2}{8\pi G}$
Ω_m	Matter Density	The normalized density of dark and luminous matter in the universe. $\Omega_m = \rho_m/\rho_c$
Ω_Λ	Vacuum density	The normalized energy density of vacuum (cosmological constant or dark energy) $\Omega_\Lambda = \rho_\Lambda/\rho_c$
Ω_b	Baryon density	Energy density in "normal matter" (protons etc)
Ω_ν	Neutrino density	Energy density in neutrinos
w	Equation of state	Dark energy equation of state (w=p/ρ)
b	Bias parameter	Ratio of the fluctuation amplitudes of the galaxy and mass distributions
σ_8	Power spectrum normalization	RMS density variation when density field is smoothed with a top hat filter of radius 8 h^{-1}Mpc
n	Spectral index	Slope of the matter power spectrum; determines the relative distribution of power on various scales
τ	Optical depth	Optical depth of CMB photons to Thomson scattering
h	Hubble parameter	Rescaled Hubble constant, in units of 100 km s^{-1}Mpc^{-1}

Table 1.1: Cosmological Parameters

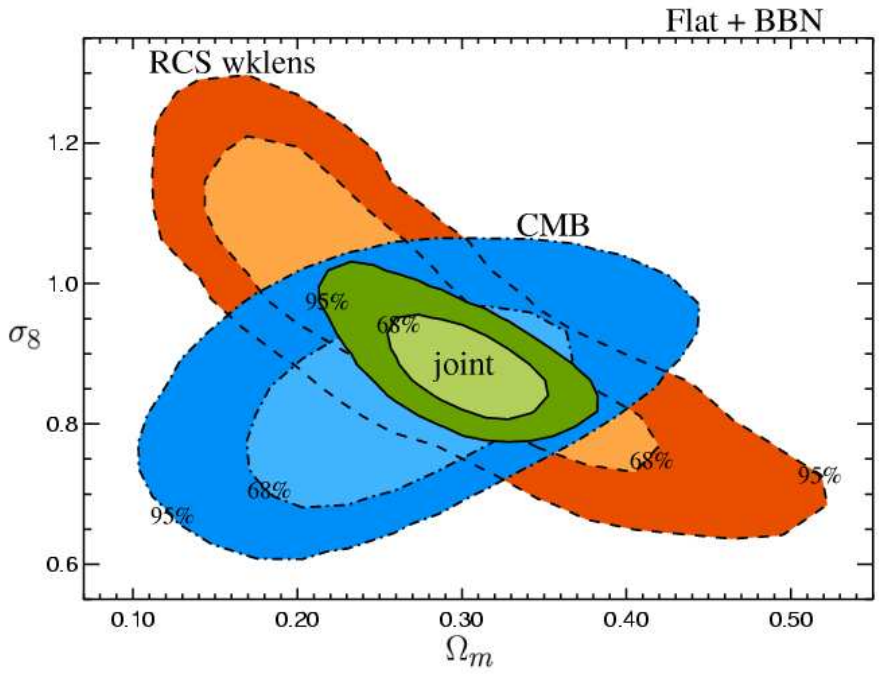

Figure 1.1: Joint contours of σ_8 versus Ω_m using CMB and weak lensing results (Contaldi et al., 2003)

to place much tighter constraints on Ω_Λ and Ω_m. Many of the observations described below are complementary in this fashion as can be seen in Figure 1.1, which shows results from cosmological weak lensing and CMB combined, and clearly indicates that you can achieve reduced error bars on parameters when different measurements are joined. The following is by no means a complete listing of cosmological parameter estimation methods, but will hopefully provide a taste for a few active areas of research.

CMB

The universe is permeated with nearly isotropic radiation of $\sim$3 K. This radiation is predicted by big bang models for the origin of the universe. The early universe was very hot and dense and the photons and baryons were in a plasma state. As the universe expanded and cooled the temperature was eventually sufficiently low to allow for the formation of the first atoms. At this point photons were no longer constantly scattering and they have been able to travel freely, from this surface of last scattering to us today.

In order for the structures that we observe in the universe today to exist there had to be very tiny temperature fluctuations in this "last scattering surface". These small fluctuations, or anisotropies, have grown in time through gravity to be the galaxies and clusters we observe today. The radiation is very nearly a perfect blackbody due to the thermal radiation from the early universe, but there are tiny variations on the order of 1 part in 10^5. These variations in temperature represent the primordial density fluctuations. While the CMB radiation was first detected in 1965 the anisotropies were not observed until 1992 by the COBE satellite (Bennett et al., 1992). There is an abundance of information contained in the CMB fluctuations. The statistical properties of the anisotropies depend on the original primordial perturbations from which they arose, and on the components in our universe which control the evolution of the perturbations between the early universe and today.

The power spectrum of the CMB fluctuations is an effective probe of various combinations of cosmological parameters. In the last decade there have been many successful CMB experiments, but we will mainly discuss the first

year results from the Wilkinson Microwave Anisotropy Probe (WMAP). This satellite is confirming what previous CMB experiments have seen, but is able to determine some parameters more precisely. WMAP was designed to create an all-sky CMB map in 5 bands. The multiple bands allow for better removal of emission from dust and point sources. The resolution of WMAP is many times better than COBE, the previous satellite CMB measurement. It bears mentioning that, because satellite missions take so long to design and launch, many of the WMAP results were just incremental improvements on other CMB experiments such as BOOMERANG, ACBAR, DASI and MAXIMA, which were ground or balloon based.

The small temperature fluctuations observed by CMB experiments can be caused by either density fluctuations or gravitational redshifts (the photons in the CMB could be red- or blue-shifted as they climb out of or fall into potential wells). Furthermore, some processes can act to smooth out the fluctuations. These factors must all be considered when interpreting temperature anisotropy maps for cosmology.

The observed temperature maps can be compared to model predictions in order to estimate fundamental parameters. This is usually done by looking at the angular power spectrum of the temperature anisotropies, which indicates the amplitude of the temperature variations as a function of angular scale. The exact mixture of the material in the early universe (matter, radiation, neutrinos) dictates where the peaks in the angular power spectrum will occur. Figure 1.2 shows the best fit WMAP angular power spectrum, expanded into spherical harmonics. Under the assumption of flatness WMAP has been able to constrain h to be 0.72 ± 0.05, the age of universe to be 13.4 ± 0.3 Gyr, $\Omega_m h^2$ to be

0.14±0.02 and $\sigma_8 = 0.9 \pm 0.1$ (Spergel et al., 2003).

The first peak of the power spectrum (Figure 1.2) is particularly sensitive to the total energy density of the universe (the sum of Ω_m, Ω_Λ). WMAP was able to estimate this at 1.02 ± 0.02, indicating that the universe is very close to flat (there is no curvature component to the universe).

The CMB contains information beyond temperature fluctuations. The CMB is predicted to be polarized due to Thomson scattering. This signal is expected to be an order of magnitude smaller in amplitude than the temperature anisotropies. It is also possible to construct a polarization angular spectrum which contains information on all angular scales. Polarization directly probes conditions at the time of the last scattering, since it is only then that free electrons were available for Thomson scattering. The polarization measurements can substantially improve the accuracy with which parameters are measured by breaking the degeneracies between certain parameter combinations, as well as probing the velocity of the matter at the last scattering surface. In addition, CMB photons can later undergo Thomson scattering from free electrons after the universe has reionized. In models where early reionization is predicted the polarization signal is enhanced on large scales.

There have now been been measurements made of the CMB polarization signal by a few CMB experiments. The WMAP group used their temperature and polarization data and found suggestions that the universe underwent early reionization and has an optical depth to scattering, τ, of 0.17±0.04. If CMB photons had only been scattered by the free electrons created by the star formation we observe to a redshift of ∼6 then τ would be substantially lower (Kogut

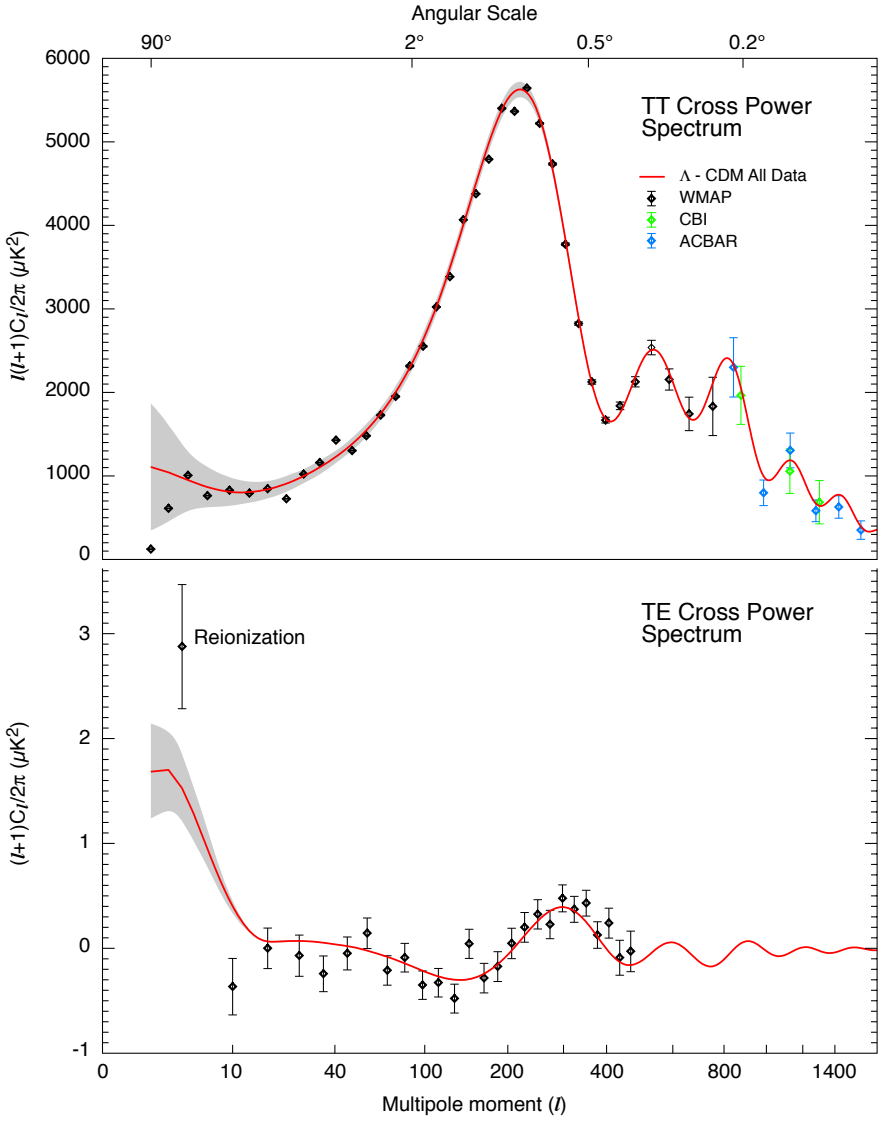

Figure 1.2: WMAP angular power spectrum plotted in spherical harmonics. The position and amplitude of the peaks can be used to constrain cosmological parameters. The first peak is located at $\sim$l=200, corresponding to roughly 1°. Credit: WMAP Science Team

et al., 2003). This exciting result indicates structures formed very early on in the history of universe. Future data from WMAP and other CMB experiments are greatly anticipated to see if this result is robust.

Type Ia Supernovae

Type Ia supernovae are formed when a white dwarf star reaches the Chandrasekhar limit of 1.4 $M_{\odot}$, after accreting mass from a binary companion. The white dwarf star explodes in a supernova explosion. Theory suggests that all type Ia supernovae should have the same intrinsic luminosity (Branch and Tammann, 1992) and therefore they can be used as standard candles. If you measure how bright a type Ia is, its distance can be inferred since they all have the same intrinsic luminosity.

A standard candle has a predictable flux, with very little scatter. The observed flux gives a "luminosity distance" as follows

$$d_L = \sqrt{\frac{L}{4\pi f}} \tag{1.1}$$

$$d_L = (1+z) R_0 S_k(r) \tag{1.2}$$

and expressions for the cosmology dependent $R_0 S_k(r)$ term can be found in Peacock (1999) Section 3.4.

In reality there is some scatter in the luminosity of type Ia supernovae and in their light-curves, even after the correction by the stretch factor to account

for differences in peak luminosity (Perlmutter et al., 1999). These uncertainties can be calibrated at high redshift by examining nearby type Ia supernovae. This method of using supernovae as standard candles has been employed extensively in the past decade and led, in 1998, to clear evidence that the universe is in fact accelerating instead of decelerating.

Two competing groups were able to detect this acceleration signal as a deviation from the standard Hubble diagram (Riess et al., 1998; Perlmutter et al., 1999). They observed that distant supernovae appear fainter at a given distance than they should. In standard big bang models, without a cosmological constant, you would expect the rate of expansion to be slowing down with time, but instead we now know that our universe is in fact undergoing a period of accelerating expansion. It is also hypothesized that the early universe underwent a rapid period of exponential growth known as inflation, but whether the mechanism that caused inflation and the mechanism causing our acceleration today are related is not known.

The best fit model to the Hubble diagram in Figure 1.3 is clearly the one with a positive cosmological constant (negative deceleration parameter). This can also be seen by looking at a plot of Ω_Λ versus Ω_m derived from the same data as shown in Figure 1.4. There is a large degeneracy in these two parameters from the supernovae data, but even from supernovae alone it appears the universe is accelerating. If these results are combined with CMB or lensing results, which do a better job of constraining $\Omega_{\rm total}$ or Ω_m respectively, then the constraints on Ω_Λ become much tighter.

The supernovae results indicate that the universe is accelerating, but there

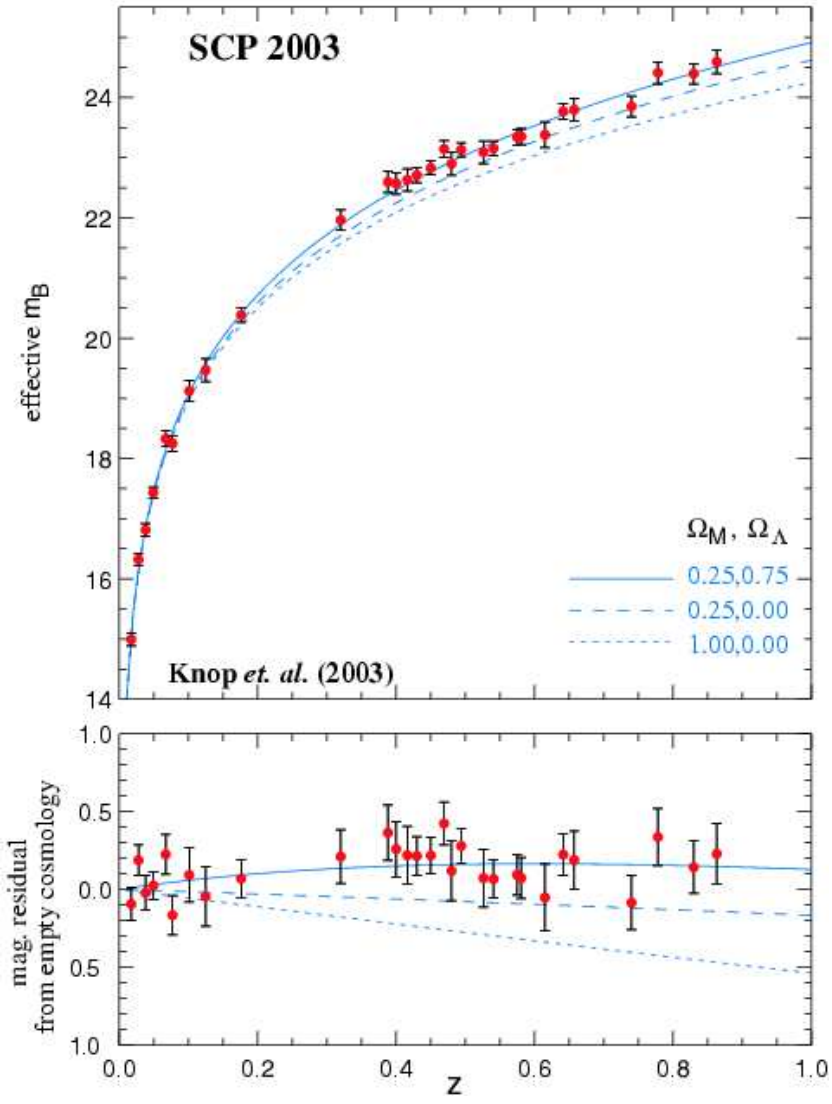

Figure 1.3: Type Ia supernovae Hubble Diagram. Apparent magnitude versus redshift for a sample of type Ia supernovae from the Supernova Cosmology Project. The best fit to the observed magnitudes is a cosmology with a positive cosmological constant. Distant supernovae appear fainter than they would if there were no cosmological constant (Knop et al., 2003)

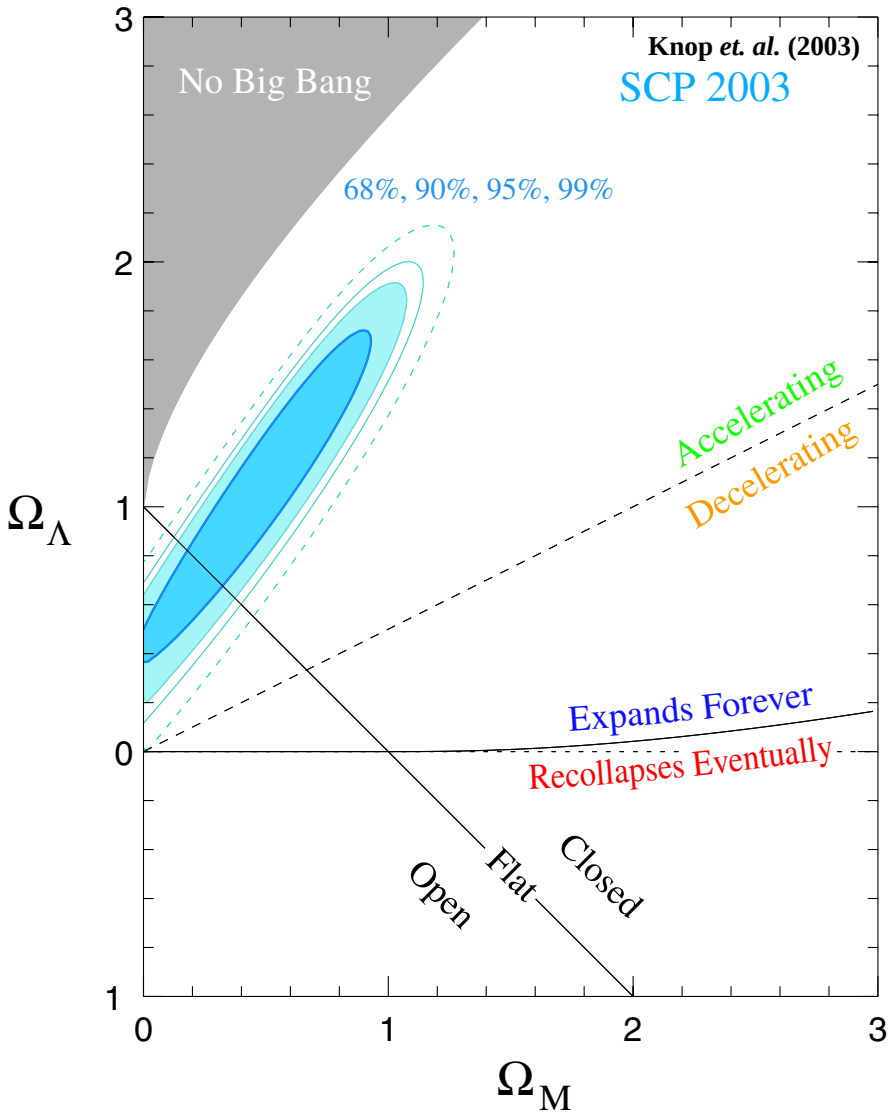

Figure 1.4: Ω_Λ versus Ω_m based on results from the Supernova Cosmology Project (Knop et al., 2003). A universe with no cosmological constant is ruled out by these data.

is a fear that there may be systematic effects masquerading as a cosmological constant. For example, if the high redshift sample of supernovae are fundamentally different than the local ones then they are not good standard candles. This can be tested to some degree by studying in the detail the spectra of type Ia supernovae. Furthermore, there could be dust obscuration causing the supernovae to appear further away than they actually are. However, to date, all astrophysical mechanisms known that could potentially cause the supernovae to appear dimmer have failed to explain the observations. All measurable quantities are the same for distant and nearby supernovae, and dust would have effects on the colours of high-redshift supernovae that are not observed (Knop et al., 2003).

Large Scale Structure

When we look out at the universe we observe objects on various scales, from stars and galaxies to clusters and large scale structure. Large spectroscopic redshift surveys, such as the Two-Degree Field Galaxy Redshift Survey (2dFGRS) and the Sloan Digital Sky Survey (SDSS), are used to measure the precise redshifts of galaxies in the nearby universe. These surveys allow us to map out the universe in 3 dimensions, and they show that galaxies tend to lie in large structures such as clusters and filaments (see Figure 1.5).

The distribution of galaxies in the universe traces the underlying dark matter structure. The observed clustering of this structure can be compared to theoretical models in order to constrain cosmological parameters. This clustering can be measured through the spatial correlation function or the matter power spectrum. The galaxy correlation function is a measure of the degree of

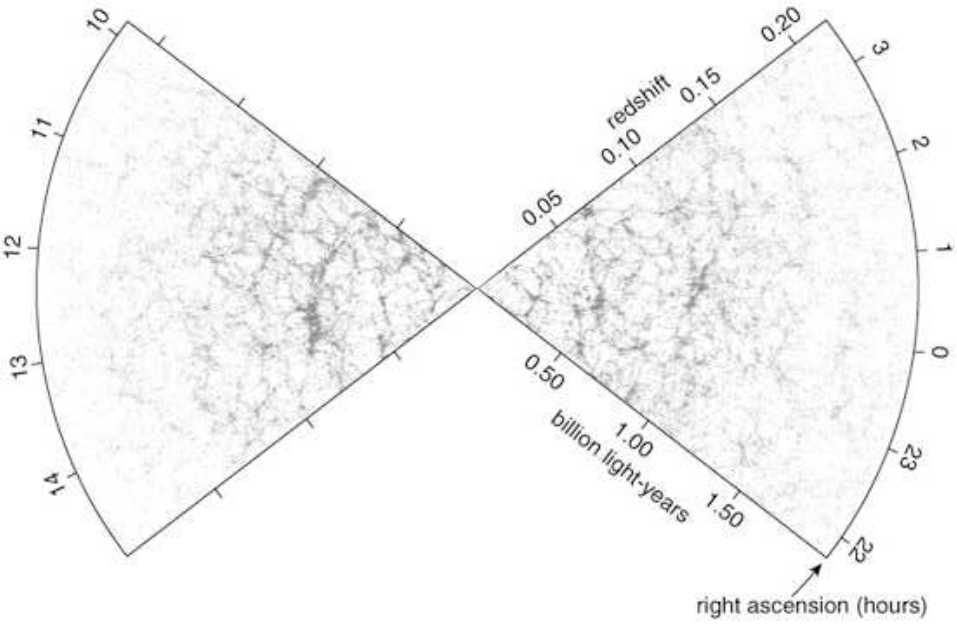

Figure 1.5: 2dFGRS map of local large scale structure. Galaxies appear to lie in a complicated web-like structure including filaments, clusters and voids.

clustering in the distribution of galaxies, and the power spectrum is the Fourier transform of the correlation function.

The power spectrum is given by

$$P(k) = <|\delta_k|^2> = Ak^n \tag{1.3}$$

where $<|\delta_k|^2>$ is the Fourier transform of the initial density fluctuations in the universe, and n is the spectral index which determines the relative power on different scales. The density fluctuations are assumed to be random Gaussian variations, and all measurements to date are consistent with this assumption.

The final cosmological parameter estimates from the 2dFGRS, assuming a perfectly flat universe, were (Cole et al., 2005):

$$\Omega_m = 0.231 \pm 0.021$$

$$\Omega_b = 0.042 \pm 0.002$$

$$h = 0.766 \pm 0.032$$

$$\mathrm{n} = 1.027 \pm 0.050$$

Perhaps the most interesting result of the 2dFGRS parameters is the favouring of a low Ω_m. This survey was able to achieve better than 10% accuracy on Ω_m, and at the 1σ level an Ω_m value of $<$0.25 is favoured over the standard $\Omega_m = 0.3$, which many models assume. Tegmark et al. (2004) used results from the SDSS and WMAP to estimate

$$h^2\Omega_m = 0.148 \pm 0.009$$

$$\sigma_8 = 0.89 \pm 0.02$$

If the value of h is fixed to be 0.72, as was done by Tegmark et al, (2004) this yields an estimate for Ω_m of 0.285$\pm$0.017 which is slightly inconsistent with the value for the 2dFGRS. If, however, the 2dF value for h of 0.766 is used with the SDSS data, the values for Ω_m are no longer discrepant. These results indicate we are indeed entering the era of precision cosmology, where the statistical uncertainties are small and systematic effects must be very well understood.

Gravitational Lensing

The deflection of light around massive objects can also be used to estimate cosmological parameters.. It is clear from Figure 1.1 that gravitational lensing is complementary to CMB measurements in terms of constraining cosmological parameters. Lensing is also complementary to large scale structure and supernovae measurements of various parameters. Lensing is a powerful tool for cosmology because it is a direct probe of the total matter content of objects and can be used to estimate the total matter content of the universe, Ω_m. Furthermore, because the matter distribution detected by lensing can be compared with the observed luminous matter distribution, the bias parameter, b, can be calculated. Gravitational lensing is also ideal for probing scales that are difficult for other cosmological methods, and can help constrain σ_8, the normalization of the power spectrum.

The details of gravitational lensing and its applications can be found in Chapter 2.

Numerical Simulations

An important aspect of using large scale structure to estimate cosmological parameters is the comparison between the observed structure and numerical simulations. Numerical simulations play a critical role is precision cosmology. They are used to implement the theoretical cosmology models, and simulation results are then compared with observations. One of the main difficulties with this process is the fact that the simulations must have an enormous dynamic range in order to sample a sufficiently large cosmological volume. It is too computationally expensive, for example, to simulate high resolution baryonic physics in a large volume. The largest cosmological simulation to date has been the "Millennium Run" (Springel et al., 2005). In this simulation semi-analytic approaches were used to model complicated galaxy formation processes inside the dark matter halos that they were able to simulate numerically with high resolution. In the following section we will discuss some of the important outstanding issues in galaxy formation models. These questions are largely being answered by combining observations data with semi-analytic simulations, rather than numerical simulations.

1.2 Galaxy Formation

The cosmological parameters can explain the universe we observe on large scales, but as we get to smaller and smaller scales baryonic physics plays a more important role. Galaxy formation depends on the formation and merging of dark matter halos, but it also depends critically on the cooling of gas and its

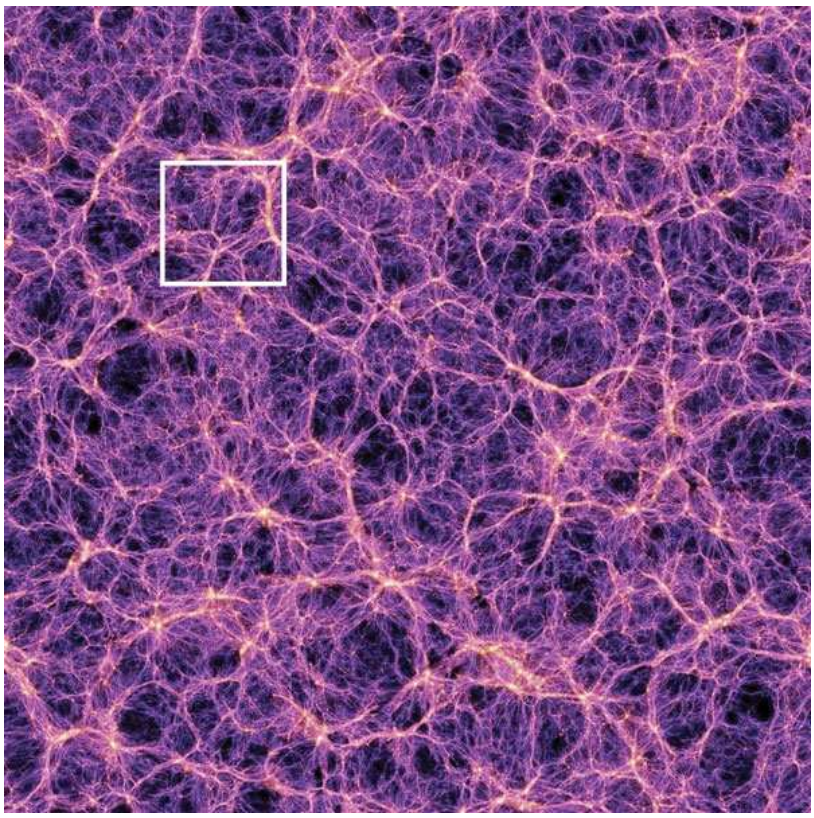

Figure 1.6: Slice of Millennium run (Springel et al., 2005). The density distribution of matter in a slice of the computational volume of the Millennium Run model. The slice is at z=0 and is roughly 1000 h^{-1}Mpc on a side. Clearly visible are high density clusters, low density voids, and the large scale filamentary structure of the universe. The white square shows the size of the computational volume for a full hydrodynamic simulation that would use up the same computational resources as the Millennium Run (Gnedin, 2005).

efficiency of turning into stars, as well as on feedback from active galactic nuclei and supernovae. These processes are extremely complex and much more difficult to model at the required resolutions than dark matter, which interacts only through gravity. While there are hydrodynamical simulations which try to model galaxy formation precisely, they do not appear to produce galaxies exactly like the ones that we observe, as we will see in the following subsections. Another method of modelling galaxy formation is through the use of so-called semi-analytic models. This method utilizes simple prescriptions for the formation of stars from gas and has analytic functions which describe the feedback mechanisms on top of merging dark matter halos generated either analytically or numerically (Cole et al., 1994).

In the local universe galaxies exist in a wide variety of shapes and sizes. We want to know the formation and evolution mechanisms of each type of galaxy, as well as larger structures such as groups and clusters of galaxies. Numerical simulations can map out the distribution of cold dark matter very well, but modelling the complicated "gastrophysics" at high resolution is still not possible in a cosmological volume. Some of the outstanding questions in galaxy formation include: What determines how efficiently galaxies can convert cold gas into stars? Is the initial mass function (IMF) of stars universal? What role do mergers play in determining galaxy morphology? What is the physical origin of the low-scatter correlations such as the Tully-Fisher relation and the fundamental plane? We will outline the basic picture of galaxy formation and then address some of these issues and their potential solutions.

The standard picture of galaxy formation involves the cooling of gas in a population of evolving dark matter halos. The evolution of the dark matter

halos is controlled by the cosmological parameters and can be modelled very well by N-body numerical simulations. If a region of space is overdense it will ultimately collapse into a halo. These halos then can accrete more mass and also merge into larger structures. It is important to note that halos that collapse at high redshift are characteristically more dense than halos which collapse at low redshift. This is because halos virialize at a multiple of the critical density, and the overall density of the universe is higher at large redshift. This means that a given velocity dispersion can be obtained with less mass at high redshift.

When dark matter halos merge, it is usually assumed that any gas inside is heated to the virial temperature (equation 1.4), although this has been questioned by recent work (Birnboim and Dekel, 2003). The gas can then radiatively cool and contract towards the centre of the potential well of the halo. If the cooling time is sufficiently short, then the temperature of the gas can drop quickly enough to facilitate the formation of a disk and fragmentation into stars. There are multiple cooling mechanisms but the most important one for galaxy formation is line cooling, which is dependent on the composition and metallicity of the gas. The gas in galaxy size halos is able to cool efficiently through line cooling and form stars, while the gas in clusters can not cool efficiently. This provides a natural explanation for why clusters are not one massive, monolithic galaxy but instead are a system of individual galaxies. Clusters are made up of galaxies that formed before entering the cluster and the rest of the gas in the halo remains hot as can be seen by its x-ray emission.

$$T_{vir} = 3.68 \times 10^5 (1 + z_{\rm col}) \left(\frac{M}{10^{12} M_\odot} \right)^{2/3} h^{2/3} {\rm K} \qquad (1.4)$$

where $z_{\rm col}$ is the redshift of collapse (Padmanabhan, 1993).

This basic picture is greatly complicated by the details of star formation and feedback. The amount of gas that can cool and turn into stars determines the total luminosity of the galaxy, and the angular momentum of the gas determines the size and surface brightness of a disk galaxy. Calculating the fraction of gas that can cool and the fraction that can turn unto stars is crucially important for modelling galaxy formation and also the significance of scaling laws such as the Tully-Fisher relation. The wide range of physical scales involved in galaxy formation makes simulation extremely challenging.

1.2.1 Issues

Cooling Catastrophe

The cooling scenario described above predicts that low mass halos will cool very efficiently and will quickly use up all of their gas. These halos, which form first in the universe, form stars too easily and according to models would contain much more of the luminosity in the universe than they do. This problem has been referred to as the cooling catastrophe. If star formation is very efficient at high redshift then all of the gas in the universe will quickly be locked up in low-mass objects. This is also very difficult to reconcile with the observation that galaxies contribute a very small fraction of the total baryonic density of the universe, implied by primordial nucleosynthesis constraints and with the existence of x-ray emitting gas in galaxy clusters. Furthermore, since there are young stellar populations in the local universe, star formation did not

exclusively occur at high redshift.

A possible solution to this cooling catastrophe is the rapid merging of systems at high redshift. If the gas is disturbed on a time scale much less than the cooling time scale then the gas will be shock-heated and unable to form stars (White and Rees, 1978). Unfortunately, the cooling time is generally much less than the merging time and therefore the gas can still cool efficiently and form too many stars. There could also be a mechanism that suppresses star formation in small halos. If the first generation of stars in low-mass halos is able to expel much of the gas when they undergo supernova explosions then that gas would no longer be available for future generations of stars. This type of feedback can solve the cooling catastrophe (White and Frenk, 1991), but implementing it in hydrodynamical simulations is difficult due to resolution limitations.

Angular Momentum

The angular momentum of cold gas in galaxies determines the size and surface brightness of galaxy disks, and thus understanding the angular momentum is of crucial importance in understanding the origin of disks and scaling relations such as the Tully-Fisher Relation. Most galaxy formation models predict galaxies with much smaller angular momentum than is observed in local disk galaxies. Our standard picture of galaxy formation involves the merger of galaxies, but numerical simulations indicate that during merger events most of the angular momentum of a galaxy will be transfered to the dark matter halo (Navarro and Benz, 1991). More recent results have indicated that if the gas cools less efficiently because of feedback, then more realistic disks are formed

(Weil et al., 1998). In order to model this problem in detail it is necessary to include accurate feedback into hydrodynamical simulations. It is necessary to understand and model the flow of gas in forming galaxies which requires very high resolution simulations.

Substructure

N-body simulations of galaxy formation find many more small halos than are observed in the local galaxy distribution (Kauffmann et al., 1993; Moore et al., 1999). For example, most simulations predict the Milky Way galaxy should have $\sim$10 times more substructure than can be accounted for with the observed satellites. Therefore, either the simulations are wrong or the observations do not find the satellite galaxies because for some reason their star formation has been suppressed and they are too faint to see. There is now some evidence that the stellar populations of dwarf galaxies are indeed younger than massive galaxies (Cowie et al., 1996). This idea of "downsizing" is relatively new and intuitively contrary to the hierarchical picture of structure formation in which small structures form first and then merge into larger objects. However, downsizing and hierarchical growth need not be in opposition, if star formation is systematically suppressed in dwarf galaxies and not in larger systems.

The solution to the substructure problem appears to be squelching by a photoionizing background (Benson et al., 1992; Somerville, 2002). In the presence of an ultraviolet background halos with a virial temperature (equation 1.4) less than the background radiation field are unable to accrete gas. This corresponds to dwarf halos with velocity dispersion of 30-50 km s^{-1}. Semi-analytic

models incorporating this squelching can reproduce the local group luminosity function (Somerville, 2002). While this may explain the substructure problem for small halos, a problem remains for intermediate mass halos with 50 km $s^{-1} \lesssim \sigma \lesssim 200$ km s^{-1}. If the substructure predicted by CDM is present, but unobserved because of suppressed star formation, then it should still be detectable via its gravitational influence. Gravitational lensing of distant quasars can be used to search for this matter. If there is substructure then the observed fluxes from multiply imaged quasars will be altered. The amount of substructure can be inferred by comparing the observed fluxes to those predicted by models with various substructure assumptions (Chen et al., 2003).

Star Formation

The complicated physics of star formation is difficult to implement in numerical simulations. The importance of star formation, however, can not be underestimated. The luminosity of galaxies, the feedback from supernovae, and the chemical enrichment of the universe are all critically dependent on star formation and its evolution. Semi-analytic models address star formation with simple "recipes" which are physically motivated analytic expressions for the fraction of gas which ends up in stars. All models also have to assume an initial mass function (IMF). Changing the IMF to make it top-heavy, for example, will produce more bright, short-lived stars and more supernovae thus influencing the interstellar medium and future star formation. The IMF is difficult to measure in the local universe because star formation is buried deep in dense molecular clouds and the lifetimes of high mass stars are very short. It is also possi-

ble that not all starbursts have a universal IMF (Kroupa, 2001). Observational constraints on star formation will be very important for future generations of semi-analytic models of galaxy formation.

In semi-analytic models (SAMs) star formation is generally considered in two modes: quiescent star formation in disks and star bursts during major mergers. All SAMs use a simple star formation rate (SFR) of

$$\dot{M}_* = \left(\frac{M_{cold}}{\tau_*} \right) \tag{1.5}$$

where M_{cold} is the mas in cold gas and τ_* is the star formation time scale. Different models assume different prescriptions for τ_*. It is generally assumed that the SFR proceeds with the same efficiency at all redshifts, but in principle it could depend on the redshift or the halo properties.

Feedback

Galaxy formation also depends critically on various feedback mechanisms. As described above it is thought that the cooling catastrophe and the angular momentum problems can be solved with the right prescription for feedback, which makes modelling feedback all the more important. SAMs include simple recipes for feedback generated by supernovae and stellar winds. The mechanisms can heat gas and also eject it from disks and halos. The basic feedback modelling in SAMs is

$$\dot{M}_{\rm reheat} \propto \beta \dot{M}_* \tag{1.6}$$

where $\dot{M}_{\rm reheat}$ is the rate of reheating and β is a parameter that depends on the surrounding galaxy and halo. Supernova feedback also serves to enrich the halo gas and can increase the cooling efficiency (Cole et al., 2000). The change in metallicity will also alter the colour and luminosity of the stellar populations. Recent SAMs (De Lucia et al., 2005) use AGN feedback to suppress cooling in massive, group-sized halos. While feedback appears to solve some of the issues in galaxy formation, the exact mechanism and details of the feedback have to be finely tuned to match the observations. SAMs rely on many free parameters and simplifying assumptions in order to reproduce a few observed properties. Ultimately any galaxy formation theory will have to predict ab initio the star formation and feedback processes, and be able to reproduce the observations of galaxy properties.

Scaling Laws

There are observed global correlations of various galaxy properties such as mass, velocity dispersion, luminosity and size which appear to have very little scatter, but the origin of these scaling laws is not well understood. In disk galaxies there is a relation, called the Tully-Fisher relation, between the luminosity and rotational velocity of the form $\mathrm{L_{gal}} \propto V^{\alpha}$, where α is dependent on the observation band. The Tully-Fisher relation has very little scatter for a wide range of luminosities indicating a conspiracy between the dark and luminous parts of the galaxy. Elliptical galaxies follow a tight correlation between luminosity, surface brightness and velocity dispersion called the fundamental plane. In order for current galaxy formation models to match these observed

correlations, feedback mechanisms must be invoked and tuned (van den Bosch et al., 2003).

Any theory of galaxy formation must be able to reproduce these scaling relations and their scatter.

Mergers

The hierarchical picture of galaxy formation involves dark matter halos merging to form larger structures and the galaxies inside them merging eventually through dynamical friction and tidal forces (see Figure 1.7). When two disks collide the ordered orbital kinetic energy gets converted into random energy allowing the galaxies to merge into a triaxial system resembling an elliptical galaxy (Barnes and Hernquist, 1992). There is also observational evidence of tidal tails and disturbed morphologies which indicate recent mergers.

Numerical simulations can track the particles of two galaxies merging but the final morphology may be dependent on bursts of star formation and feedback, which at present can not be modelled with sufficient resolution (Springel et al., 2005). SAMs use simple prescriptions for star formation and feedback on top of the merging dark matter halos in order to track galaxy properties. Whether or not the merging of spiral galaxies produces elliptical galaxies with precisely the observed properties of ellipticals requires better modelling and higher resolution simulations. The basic picture at present is that minor mergers between spirals and satellites will not greatly alter the morphology of the galaxy, while major mergers between 2 or more nearly equal mass galaxies will result in an elliptical (Cretton et al., 2001).

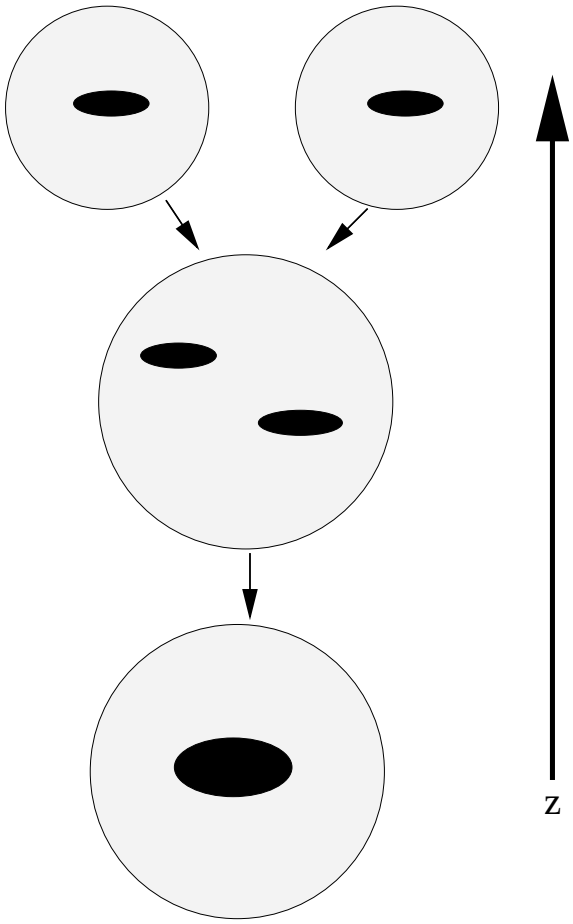

Figure 1.7: Merging galaxy schematic. At high redshifts galaxies are smaller and live in small halos. Over time the halos merge and eventually so do the galaxies within them.

There are still many outstanding questions related to merging and galaxy morphologies. For example, while giant ellipticals should have formed by the merging of smaller galaxies, they appear to have uniformly old stellar populations, favouring an early formation epoch. This seems counter-intuitive to the hierarchical picture in which massive systems should have formed quite recently. Recent results from the Millennium run seem to indicate that that the observed "anti-hierarchical" behaviour can still be consistent with the merging of disk galaxies to form the observed elliptical population (De Lucia et al., 2005), if feedback is tuned to suppress gas cooling in high-mass halos.

1.2.2 Halo Occupation Distribution (HOD)

The halo occupation distribution (HOD) is a model for understanding the relation between dark matter halos and luminous galaxies. The HOD specifies the probability P$(N|M)$ that a halo of virial mass M contains N galaxies of some type. A complete theory of galaxy formation should predict the distributions of galaxies and the relation between the spatial clustering of any type of galaxy and that of the dark matter distribution. In this era of massive redshift surveys it is important to understand the biases of galaxies as a function of their observable properties and for theories to be able to quantify these biases.

The HOD formalism describes which types of galaxies live in which halos. If the HOD at a fixed mass is not a function of the large scale environment, as theory predicts (Bond et al., 1991), then the HOD describes essentially everything that can be known about galaxy bias and galaxy clustering. It is therefore very important to measure the HOD for all populations of galaxies and compare

this to theoretical predictions (Kravstov et al., 2004). Predictions from HOD models can be compared to the observed correlation function between dark matter halos and observed galaxies, ξ_{gm}. This correlation is measured directly with weak gravitational lensing, and thus lensing results and HOD models can be compared.

1.2.3 M/L

The mass-to-light ratio (M/L) of a system, such as a galaxy or cluster, is an important estimate of the ratio of dark to luminous material. The M/L ratio is also related to the global SFR, if it is measured in a blue band, or to the star formation history, if measured in a near-infrared band. It is relatively easy to estimate the luminosity of objects based on observed properties but estimating the total mass of a system is difficult since so much of it is locked up in dark matter. One of the reasons that knowing the total mass, and hence M/L, is so important is that it can help to estimate the matter density of the universe, Ω_m, so shown in the following equation.

$$\Omega_m = \frac{\rho_m}{\rho_c} = \frac{\rho_L}{\rho_c}\frac{M}{L} \tag{1.7}$$

If the M/L were universal then it would suffice to measure it for one object and combine this with the luminosity density, ρ_L, in order to calculate Ω_m. However, as we will see different objects in the universe have different M/L ratios indicating there is a segregation between mass and light at some scale. In order to estimate Ω_m the M/L ratio must be measured on the appropriate scale.

There are a number of ways to estimate the total mass of a system, some of which will be described in section 1.3, including dynamical and lensing methods. The dynamical methods generally require the assumption that the system is in a relaxed, virialized state, which may not be the case for the outer regions of clusters, or in low mass groups, for example. Gravitational lensing, on the other hand, is a more direct way to measure the mass of systems and can estimate masses without making equilibrium assumptions.

The formation of galaxies is critically dependent on the ability of gas to cool. In small halos the gas is easily reheated by feedback processes and in large halos galaxy formation is suppressed because of the long cooling times. This indicates that there should be a minimum in M/L at $\sim 10^{12} M\odot$ (Benson et al., 1992). There is a general trend for M/L ratio values to increase from galaxy to cluster scales from both observations and theory (see Figure 4.8). The observational measurements of M/L ratios require very accurate photometry and corrections in the luminosity for incompleteness, as well as reliable mass estimates. On cluster scales there is indication that the M/L is independent of mass (Bahcall et al., 1995; Carlberg et al., 1996; Rines et al., 2004). This universal value for M/L in clusters indicates that the star formation efficiency in rich clusters must be a well regulated process. Recent models by Tinker et al. (2005) indicate that, while the M/L as a function of mass plateaus on large scales, the amplitude of the M/L plateau is a strong function of cosmological parameters, particularly σ_8. Van den Bosch et al. (2004) found a similar result using data from the 2dFGRS. They showed that either clusters have very high M/L ratios or that σ_8 is relatively low.

Understanding the radial profile of the M/L ratio for a class of objects is

important for understanding where the divide between mass and light occurs. Rotation curves indicate that the outer regions of spiral galaxies are dominated by dark matter, while clusters appear to have M/L profiles that are very flat with radius (Carlberg et al., 1996; Hoekstra et al., 2000). A dynamical study of a sample of intermediate redshift galaxy groups (Carlberg et al., 2001) indicated a steep radial M/L ratio profile, suggesting that groups ($\sim 10^{13} M_{\odot}$) may be at the scale where the segregation between luminous and dark matter occurs. However, our lensing measurement for this sample of groups (Parker et al., 2005) indicated that the M/L ratio was very flat with distance from the group centre. Ideally there would be a large enough sample of groups available so that the radial profile could be estimated using various techniques at a range of redshifts, looking for evolution. The interest in M/L ratios is not only to estimate the quantity of dark matter, and thus Ω_m, but also to understand the dependence of star formation on environment.

Galaxy formation models must be able to predict the observed M/L ratios and be able to explain the physical basis for the differences between actively star forming regions and passively evolving regions.

1.3 Dark Matter

In 1933, Fritz Zwicky observed that the mass-to-light (M/L) ratios of rich clusters of galaxies were anomalously large. In fact, luminous matter fell short of the observed mass by factors of as much as one hundred. Seventy years later, the identity of this dark material remains one of the great mysteries of astro-

physics. A fundamental difficulty in probing the nature of dark matter is the fact that is does not emit or absorb electromagnetic radiation. When studying baryonic astrophysics we can observe stars, galaxies or clusters at various wavelengths of the electromagnetic spectrum and determine how the matter is distributed and of what it is composed. Without this capability for dark matter we generally have to indirectly detect its properties through its gravitational influence. The candidates for this dark matter can be generally separated into two different categories – large, baryonic objects such as planets, stars and black holes, or weakly interacting fundamental particles.

The distribution of dark matter is different depending on which of the above candidates is the correct description. The evidence for the existence of dark matter, as will be discussed in sub-section 1.3.1, all points to a smooth distribution of non-relativistic particles, rather than black holes or planets. There is a further piece of evidence which points to a non-baryonic component to the universe. Early universe predictions of big bang nucleosynthesis (BBN) indicate that there are not enough baryons in the universe to account for the quantity of dark matter observed (Dar, 1995). BBN correctly predicts the abundances of the light elements, but requires a low baryon density in order to do this. Thus, a low baryon density and an exotic dark matter component is the favoured model for the universe.

The missing mass is believed to be in the form of weakly interacting particles. These particles could be neutrinos or they could be ones predicted by supersymmetric extensions to the standard model of particle physics, such as the neutralino. We will introduce how we observe dark matter on galactic and cosmological scales and then discuss the possibility of detecting the dark mat-

ter particle(s) directly using detector physics on Earth.

1.3.1 Evidence for Dark Matter

As mentioned above Zwicky had observations more than 70 years ago that indicated that there was much more mass in rich galaxy clusters than could be explained by the observed luminous material. This did not necessarily indicate the existence of dark matter, since the missing mass could have been locked up in unobserved gaseous components, for example. There are now many independent lines of evidence for the existence of a large quantity of non-baryonic dark matter in the universe. We will review a few of these astrophysical dark matter search techniques.

Rotation Curves

The next big leap in the evidence for the existence of dark matter came in the form of flat rotation curves for spiral galaxies. If a mass is on a stable Keplerian orbit, and the mass distribution is spherical, then you would expect its rotation velocity to go as

$$v(r) \propto \sqrt{M(r)/r}, \tag{1.8}$$

where $M(r)$ is the mass inside radius r. If mass follows light you would then expect at large radii for the rotation velocity to go as

$$v(r) \propto \sqrt{1/r} \tag{1.9}$$

This type of behaviour can be observed in our Solar System where the planet Neptune, for example, orbits much more slowly than Mercury. However, on galactic scales, observations indicate that the rotation velocities of stars and gas are constant with increased distance from the galaxy centre (Rubin, 1983). This indicates there is mass present that we do not observe. In fact, flat rotation curves imply that the density

$$\rho(r) \propto \frac{1}{r^2} \tag{1.10}$$

and

$$M(r) \propto r \tag{1.11}$$

This curious result was first observed by Vera Rubin and collaborators in the 1970's. This is still an active area of research and continues to be one of the most convincing pieces of evidence for the existence of dark matter. The drawback to this technique is that it requires visible tracers to map out the rotation curve, and thus is not effective beyond where the visible part of the galaxy fades away. In addition, fitting rotation curves requires assumptions about the shape of the dark matter halo, the size of the baryonic components of the galaxy and the orbits of the objects used to measure the rotation curve.

Dynamical Evidence

Rich galaxy clusters are the largest gravitationally collapsed objects in the universe. The study of galaxy clusters is important because their physical properties and spatial distribution can be used to constrain cosmological parameters

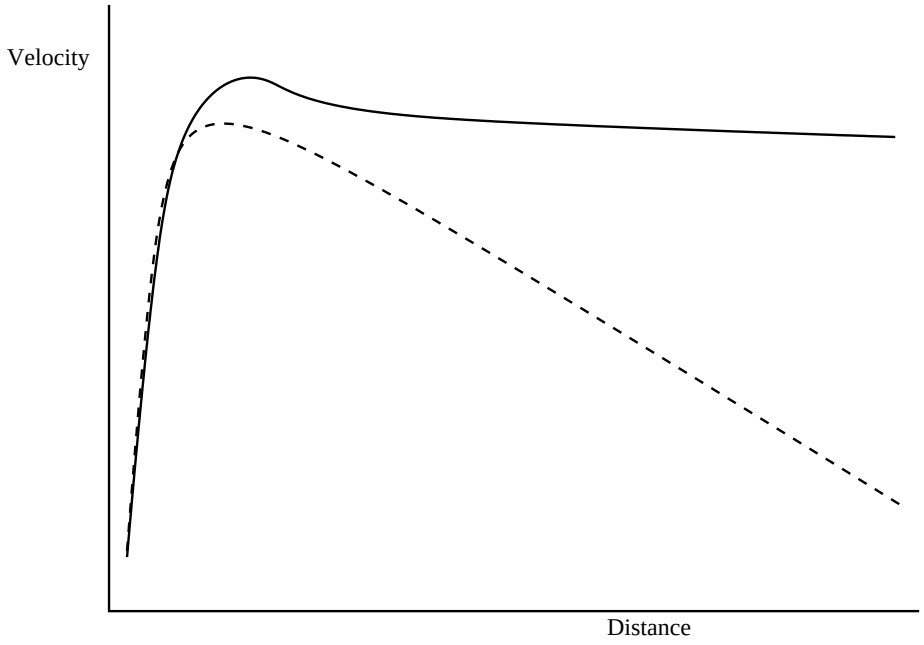

Figure 1.8: Schematic disk galaxy rotation curve. The dashed line is the expected rotation curve for an object in a stable Keplerian orbit. The solid line is a typical observed rotation curve. A smooth dark matter component with a density profile $\rho \propto \mathrm{r}^{-2}$ added to the stars and the gas fits most observations very well.

such as the Ω_m. For example, if the matter density of the universe is high then clusters of galaxies tend to form at higher redshift than if the matter density is low. Galaxy clusters are also the perfect objects to study in the search for dark matter. We can accurately measure the velocity dispersions of galaxies in nearby clusters. The velocity dispersions of galaxies is indicative of the dark matter potential well in which they live. If clusters are very massive (contain a lot of dark matter) then the velocity dispersions of the galaxies in them will be significantly larger than if there is no dark matter.

The typical velocity dispersion of rich clusters is $\sim$1000 km s^{-1}. This indicates that cluster masses are roughly 10 times greater than can be accounted for by adding up the mass from all the stars and gas (inferred from the distribution of light). With velocities this high galaxies would fly out of clusters unless there is a large, unseen mass component. While Zwicky first noted this in 1933, in the Coma cluster, much more precise measurements have now been made for many clusters. While this technique is a promising way to estimate the quantity of dark matter it has some of the same drawbacks as the rotation curve analysis. The systems under observation must be modelled very well (usually dynamical equilibrium is assumed), and again visible tracer populations are required.

X-ray Evidence

Objects in the universe emit x-rays if their temperatures exceed approximately 10^7 K. If there is a significant quantity of dark matter in galaxy clusters then you would expect the temperature of the gas in those deep potential wells to be sufficiently hot to emit x-rays. Many clusters do show extended x-ray emis-

sion ((Briel et al., 1992), for example). The thermal pressure from this gas is enormous and much more matter than is observed is required in order to hold these clusters together. The x-ray emitting gas and the galaxies do not contain enough mass to hold the cluster together and thus there must be a significant quantity of dark matter in clusters.

The x-ray emission from clusters can be used to estimate the total mass of a cluster, but the estimation relies on a few assumptions, most importantly that the system is in a relaxed thermal equilibrium state. In order to estimate the density and pressure of a cluster the size must be known and generally sphericity is assumed. The calculated pressure can be used to estimate the necessary dark matter component to keep the cluster stable.

CMB

As discussed in the Section 1.1 the CMB is a powerful probe of cosmological parameters and can tell us about something about the amount of dark matter in the universe. The amplitude of the fluctuations in the CMB are of the right amplitude to explain the structures we observe in the universe today. Without dark matter the small fluctuations observed in the CMB could not have been amplified by gravity into the structures present at low redshift. It is important to note that the fit to the CMB angular power spectrum (Figure 1.2) is based on a CDM model with a positive cosmological constant. The peaks in the spectrum are not well-fit by a model without non-baryonic dark matter.

Gravitational Lensing

Nearly 100 years ago Einstein developed his theory of General Relativity which describes gravity in a new way. In this theory the presence of mass creates curvature of space-time. The differences between Newtonian gravity and General Relativity are very small in most situations, but General Relativity can manifest itself in some very exciting ways that help in the study of dark matter. One of the key predictions of General Relativity is the bending of light in a gravitational field. The bending angle of the light depends on the mass that is causing the deflection and the geometry of the system. This technique has been used to detect dark matter in galaxies, clusters and large scale structures.

The details of how gravitationally lensing can be used to study dark matter will be explained in detail in Chapter 2.

Summary

With the exception of gravitational lensing all of these techniques require visible tracers. The presence of dark matter is deduced by observing the behaviour of these tracers. Therefore, where there are no tracers we know very little about the presence and/or distribution of dark matter. Numerical simulations and theoretical models require observational inputs on all scales in order to try and understand the composition of this mysterious dark matter component.

1.3.2 Direct Dark Matter Particle Searches

While the astrophysical evidence for the existence of dark matter is overwhelming, there is still the need to identify the particle (or particles) which make up this component of our universe. This has become a very active area of astroparticle physics research. An early candidate for the dark matter particle was the neutrino, but, though neutrinos have recently been shown to have mass (Fukuda et al., 1998; Aharmim et al., 2005), they move too quickly to explain the dark matter structures we see in our universe today. Neutrinos are not capable of collapsing into the halos we observe. Other favoured candidates include the axion and the neutralino. These particles (known as weakly interacting particle or WIMPs) do not interact through the electromagnetic force and this is why they are so difficult to detect.

Understanding the nature of the dark matter particle(s) is of great importance to astrophysics, but is also extremely important to the fields of particle physics, supersymmetry and quantum gravity. The prospect of identifying these particles by directly detecting them has a promising future, but has yet to produce conclusive results. Most current detectors operate in a fashion similar to neutrino detectors in that they search for the signature of scattering events. One of the primary difficulties in the quest for directly detecting the dark matter particle(s) is the wide range of predicted energy scales from theory. The theoretical work on dark matter has produced estimates of the energy scale over at least 5 orders of magnitude (Gaitskell, 2004). There is considerable optimism that in the next decade direct dark matter particle searches will be successful, or at the very least rule out some of the currently most favoured models.

Ultimately some sceptics of dark matter will not be convinced until the particles that comprise it are identified and studied.

1.3.3 Dark Matter, What Dark Matter?

It is important to note that there are also alternative theories which do not require dark matter to explain some of the above-mentioned observations. Such theories modify the inverse-square law of gravity. In general, such modified gravity theories can explain flat rotation curves very well, but do less well explaining the observations on larger scales, such as in clusters or large-scale structure. The most well-known variety of these theories is Modified Newtonian Dynamics (MOND) (Milgrom, 2002). This theory states that Newtonian gravity still holds true for the kinds of accelerations that take place inside our solar system, but that there are differences when the mass is accelerating very slowly, such as for bodies within galaxies or larger structures. This theory has some successes, particularly in fitting spiral galaxy rotation curves (Figure 1.9, for example), but most astrophysicists remain very sceptical of MOND and think dark matter is a more natural solution to the missing mass problem. MOND, in its original form, has always had difficulty describing phenomena such as gravitational lensing partly because a complete relativistic version of the theory did not exist. However, there is now a relativistic theory which reduces to MOND on galactic scales (Bekenstein, 2004). This theory should be testable by looking for an anisotropic lensing signal (to be described in Section 2.3).

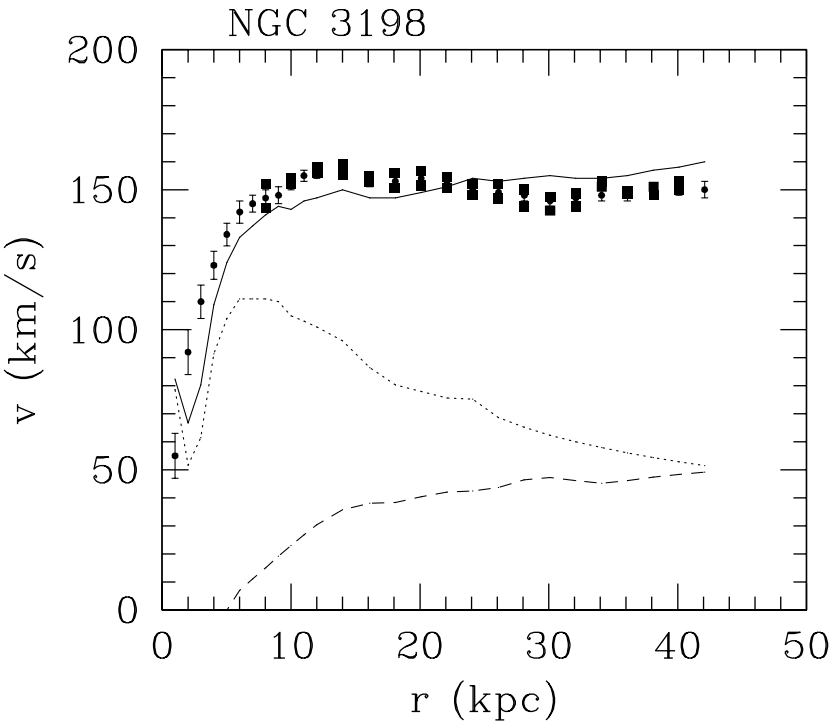

Figure 1.9: Galaxy rotation curve fit for NGC3198. The solid line is the best fit MOND model while the dotted and dashed lines are the Newtonian rotation curves of the stellar and gaseous components respectively (Bottema et al., 2002)

1.4 Outline of Thesis

In this thesis I will discuss two separate observational projects which use weak gravitational lensing as a probe of mass distributions. In Chapter 2 I will introduce the field of gravitational lensing, providing a historical context as well the basic theoretical aspects. In addition, I will mention some of the most recent results from the field of gravitational lensing and the various applications this technique has in the field of cosmology.

Chapter 3 is a detailed look at the data reduction and analysis of a sample of galaxy groups. In Chapter 4, I will discuss the weak lensing signal from these groups and use that to infer their velocity dispersion and hence mass. Using what is known about the luminous content of these groups one can then deduce the M/L ratio of galaxy groups, which is an interesting constraint on any theory of structure formation. Chapter 5 is a study of galaxy dark matter halos in the Canada-France-Hawaii Telescope Legacy survey. This galaxy-galaxy lensing project presents preliminary results based on early data from this ongoing survey. Finally, Chapter 6 will offer a summary of results and a discussion of future work in the field of weak lensing.

Chapter 2

Gravitational Lensing

If your experiment needs statistics, then you ought to have done a better experiment.

— Ernest Rutherford

Gravitational lensing is the bending of light which passes close to a massive object. It is predicted by Einstein's Theory of General Relativity, and is due to the fact that the space-time around massive objects is curved and distorted. Soon after the publication of Einstein's theory of General Relativity, there was confirmation of one of its predictions. In 1919, Eddington succeeded in detecting gravitational lensing of the light from a star passing near the sun during a solar eclipse. The measured offset in position was consistent with the value predicted by General Relativity, thus adding substantial credibility to the theory.

2.1 Physics of Lensing

The strength of the gravitational lensing signal is dictated by the mass of the lens and the geometry of the system. For example, the signal is stronger if the lens and source are well-separated in redshift space and if the alignment along the line-of-sight is close between the lens, observer and source (see Figure 2.1). Gravitational lensing is generally divided into two categories based upon whether there are multiple light rays which reach the observer (strong lensing) or just small distortions of the background sources (weak lensing) as in shown in Figure 2.2. The following equations are standard gravitational lensing equations. For a review please see Bartelmann and Schneider (2001) or Mellier (1999).

The bending of light around a mass, M, is given by

$$\alpha = \frac{4\mathrm{GM}}{bc^2}, \tag{2.1}$$

where G is the gravitational constant, c is the speed if light and b is the impact parameter of the light ray as shown in Figure 2.1. The angular position of a lens is described by the *lens equation*

$$\vec{\theta}_S = \vec{\theta}_I - \frac{D_{LS}}{D_S}\alpha(\vec{\theta}_I), \tag{2.2}$$

where D_{LS} and D_S are the angular diameter distances between the lens and source, and to the source respectively. If the lens equation has more than one solution then the lens is producing multiple images of the source. If the lens,

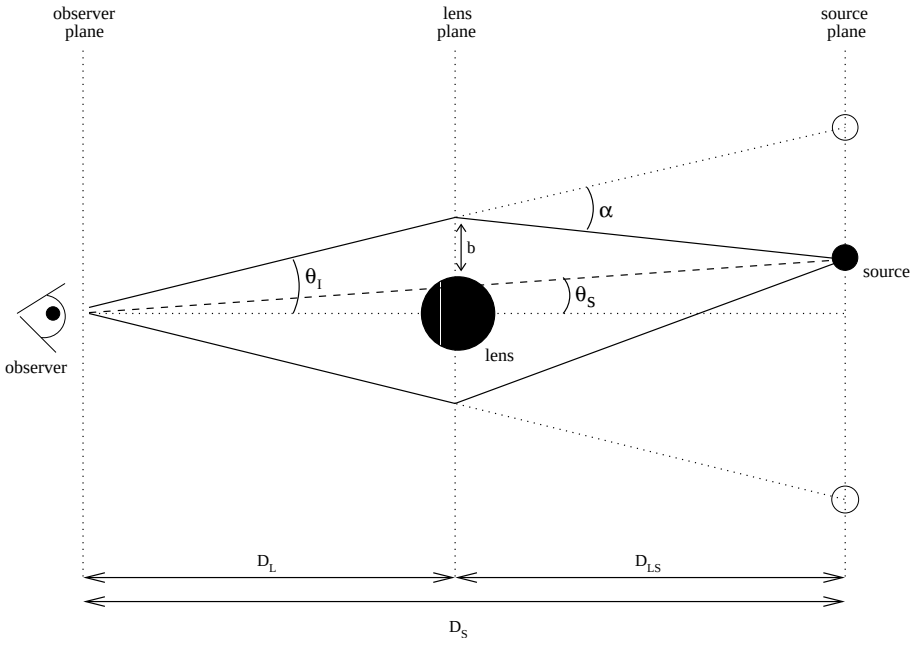

Figure 2.1: The geometry of a lensing system where $\vec{\theta}_I$ is the observed angular position of the source, $\vec{\theta}_S$ is the intrinsic position of the source, b is the impact parameter, and α is the bending angle. D_L, D_S and D_{LS} are the angular diameter distance to the lens, source and between the lens and source, respectively. The figure is not to scale, and all angles in weak lensing analysis can be considered to be very small.

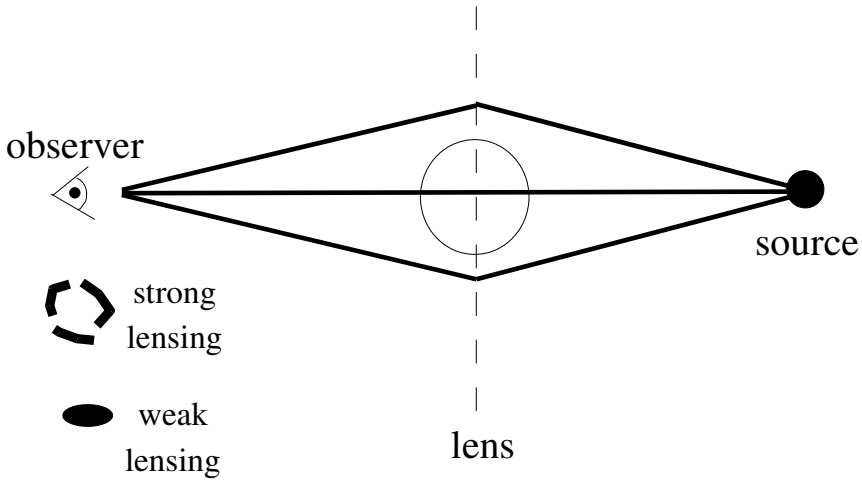

Figure 2.2: Weak and strong weak lensing regimes. When the alignment between the observer, lens and source is close, multiple images and giant arcs can form. When the alignment is poor, distant sources are only slightly distorted, and are called arclets. This weak distortion must be measured statistically through weak gravitational lensing

source and observer are exactly aligned then the image of a source will be stretched into a circle, where the radius is called the *Einstein radius* and is given by

$$\theta_E = \left(\frac{4GM}{c^2} \frac{D_{LS}}{D_L D_S} \right)^{1/2}, \tag{2.3}$$

where D_L is the angular diameter distance to the lens. A popular lens model is the isothermal sphere. This mass distribution, with a density profile $\rho \propto r^{-2}$, appears to fit most results very well and is consistent with results from numerical simulations. The isothermal sphere mass distribution leads to an Einstein radius of

$$\theta_E = \left(\frac{4\pi\sigma^2}{c^2} \right) \frac{D_{LS}}{D_S} \tag{2.4}$$

$$= \left(\frac{\sigma}{186 \mathrm{kms}^{-1}} \right)^2 \frac{D_{LS}}{D_S} \mathrm{arcsec}, \tag{2.5}$$

where σ is the line-of-sight velocity dispersion of the lens.

In order for multiple images to form, the lens must be "strong"; this can be quantified by the dimensionless surface mass density

$$\kappa(\vec{\theta_I}) = \frac{\Sigma(D_L \vec{\theta_I})}{\Sigma_{cr}}, \tag{2.6}$$

where

$$\Sigma_{cr} = \frac{c^2}{4\pi G} \frac{D_S}{D_L D_{LS}} \tag{2.7}$$

Σ_{cr} is the *critical surface mass density* which is a function of the redshifts of the lens and the source. A mass distribution with $\kappa > 1$ will produce multiple images.

A convenient, simple lens model is the isothermal sphere. The projected mass density for this profile is

$$\Sigma(b) = \frac{\sigma^2}{2Gb}, \tag{2.8}$$

where σ is the line-of-sight velocity dispersion of the particles in the halo (as in equation 2.5), assuming they are in virial equilibrium. This mass profile yields the dimensionless surface mass density of

$$\kappa(\theta_I) = \frac{\theta_E}{2\theta_I}, \tag{2.9}$$

where θ_E can be found in equation 2.4.

The bending angle $\vec{\alpha}$ can be re-written in terms of κ

$$\vec{\alpha}(\vec{\theta_I}) = \frac{1}{\pi}\int_{\mathbb{R}^2} d^2\vec{\theta}'_I \kappa(\vec{\theta_I}')\frac{\vec{\theta_I} - \vec{\theta_I}'}{|\vec{\theta_I} - \vec{\theta_I}'|^2} \tag{2.10}$$

The bending angle can also be written as the gradient of the lensing potential $\vec{\alpha} = \bigtriangledown\psi$ where the lensing potential, ψ is

$$\psi(\vec{\theta}) = \frac{1}{\pi}\int_{\mathbb{R}^2} d^2\theta' \kappa(\vec{\theta'}) \ln|\vec{\theta} - \vec{\theta'}| \tag{2.11}$$

The lensing potential also satisfies the Poisson equation $\bigtriangledown^2\psi = 2\kappa(\vec{\theta_I})$

The shapes of distant sources are distorted by a lensing potential and different parts of an extended image are deflected differently. It is also possible to describe the distortion of distant sources using the Jacobian matrix of the lens equation (equation 2.2)

$$\mathcal{A} = \mathcal{A}(\vec{\theta_I}) = \frac{\partial \vec{\theta_s}}{\partial \vec{\theta_I}} = \begin{bmatrix} 1-\kappa-\gamma_1 & -\gamma_2 \\ -\gamma_2 & 1-\kappa+\gamma_1 \end{bmatrix}, \tag{2.12}$$

where γ_1 and γ_2 are components of the *shear*. The κ term changes the size of objects, but not the shape.

$$\gamma_1 = \frac{1}{2}(\psi_{11} - \psi_{22}) = \gamma \cos 2\phi \tag{2.13}$$

$$\gamma_2 = \psi_{12} = \psi_{21} = \gamma \sin 2\phi \tag{2.14}$$

$$|\gamma| = \sqrt{\gamma_1^2 + \gamma_2^2}, \tag{2.15}$$

where ψ_{ij} are the partial derivatives of the lensing potential with the respect to the components of $\vec{\theta_I}$. The shear for an isothermal sphere is given by

$$\gamma(\vec{\theta_I}) = -\frac{\theta_E}{2|\vec{\theta_I}|} e^{2i\phi} \tag{2.16}$$

The singular isothermal sphere is not a realistic mass distribution since the surface mass density diverges as $\vec{\theta_I} \to 0$, but it does fit most lensing data very well.

2.2 Strong Lensing

Strong gravitational lensing occurs when there is a mass distribution for which $\kappa \geq 1$ somewhere, or in other words, where the surface mass density exceeds the critical value, Σ_{cr}. This is the regime for which multiple images of a distant source are formed. It occurs because the light from a source is sufficiently bent that more than one light ray reaches the observer. Some of the most spectacular images captured by the Hubble Space Telescope (HST) have been of rich, strong lensing clusters. The mass concentration in clusters is sufficient to distort background sources into long extended multiple arcs. These images, an example of which can be seen in Figure 2.3, are not only beautiful but also extremely useful for the determination of the mass distribution in galaxy clusters.

Strong lensing can be used to directly probe the matter distribution in foreground lenses (usually clusters or massive elliptical galaxies), calculate the Hubble Constant through the time delay of multiply imaged quasars, or probe dark matter in our galaxy through the microlensing of stars in the Milky Way or nearby satellites.

Arcs

High resolution images of galaxy clusters sometimes show sources distorted and stretched into giant arcs (Figure 2.3). These strong lensing arcs require massive lenses and alignment of the arc source with the lens (usually a galaxy cluster). At larger angular distance from the cluster centre, images of background galaxies are only weakly deformed, and they are referred to as arclets

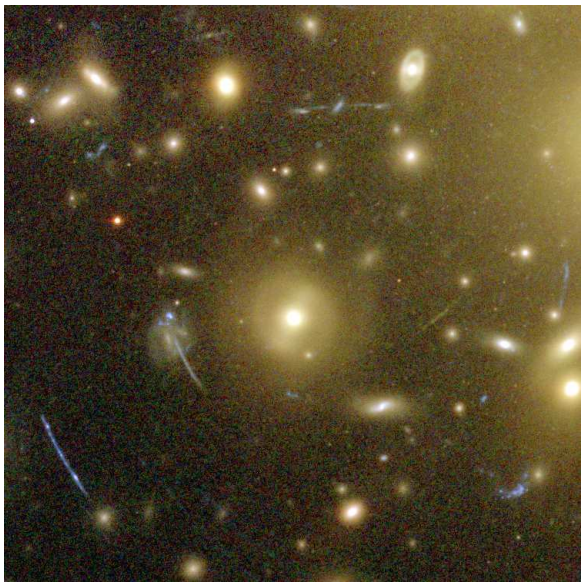

Figure 2.3: The central region of Abell 1689. Many strong lensing features are clearly visible in this HST image. Strong lensing arcs are much easier to locate in space-based observations because of the greatly increased spatial resolution. Credit: NASA, N. Benitez (JHU), T. Broadhurst (Racah Institute of Physics/The Hebrew University), H. Ford (JHU), M. Clampin (STScI), G. Hartig (STScI), G. Illingworth (UCO/Lick Observatory), the ACS Science Team and ESA

(see Figure 2.2). These arcs can be exploited in two ways. Firstly, the positions, sizes and fluxes from the arcs can be used to model the object causing the lensing, and thus the dark matter content (Mellier et al., 2003). This method is particularly useful for studying the mass distribution in the inner-most part of the cluster. The locations of the arcs are associated with the Einstein radius of the cluster, and are therefore useful for studying the mass internal to θ_E. Unlike dynamical or x-ray studies of clusters, lensing studies do not require any equilibrium assumptions. Secondly, the arcs are highly magnified distant sources which would be too faint to study without the magnification effect of lensing. Consequently, an efficient way to hunt for the highest redshift galaxies is to observe strong lensing clusters. It is possible, in this way, that galaxies in the earliest stages of their formation may be found.

The superior resolution of the Hubble Space Telescope has allowed a number of systems with strong lensing arcs to be observed. Based on the assumption that the cluster mass is smoothly distributed and can be described analytically, the positions of the arcs can allow the mass distribution to be constrained. Once a simple lens model has been constructed, substructure can be added to try and fit the observed arcs better. In addition, the mass model can be used to predict the positions of more arcs which were not previously observed. This has led to the successful recovery of arcs which were not initially seen in the images (Bradac et al., 2005). The lensing models are improved if the exact redshifts of the arc sources are known. This is fortunately often the case, since the arcs are highly magnified, and therefore they can be studied spectroscopically.

Quasars

Quasars can be split into multiple images by the effect of strong gravitational lensing as can be seen in Figure 2.4. The light from these multiple images will follow different paths to us here on Earth. The time delay in the arrival of the signal from different images can be used to estimate the expansion rate of the universe, and hence the Hubble constant. Currently the best estimates of the Hubble constant come from distances calibrated via Cepheid Variable Stars. These techniques both lead to approximately 10% uncertainty (Schechter, 2005) in the value of the Hubble Constant, assuming the universe is perfectly flat. Strong gravitational lensing can be used to estimate H_0 to at least this accuracy, but there are a number of systematics which must be overcome.

One of the primary challenges with using quasars to measure the Hubble Constant is that not all quasars are observed to have variable behaviour. In order to detect a delay in arrival times, there must be a variable signature to search for. In addition, in order to calculate the Hubble Constant, the lens causing the strong lensing must be precisely modelled, particularly in the central region. In some cases no lens is observed, or not nearly enough information about the lens is known. There is, therefore, a lack of constraints in most quasar strong lensing systems.

The time delay is a function of the lens properties and, in order to determine it accurately, the quasar system must be continuously monitored over a long period of time. Like many areas of gravitational lensing quasar lensing observations have greatly benefited in recent times from advances in technology especially from large diameter, high-resolution telescopes. There are currently

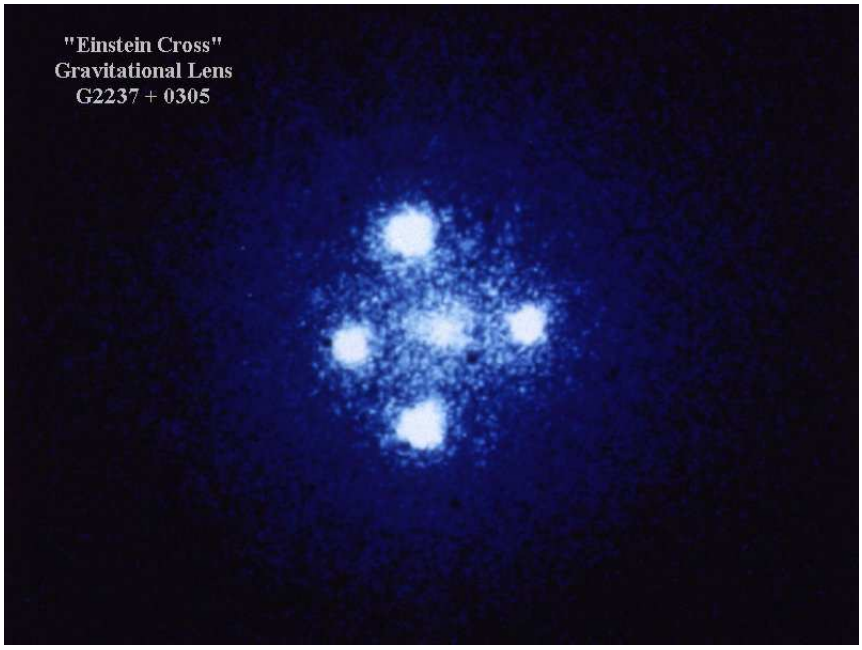

Figure 2.4: Gravitational lens G2237 + 0305. A distant quasar multiply imaged by strong gravitational lensing into a quadrupole image. Credit:NASA and STScI.

surveys dedicated to finding variable lensed quasars with the hopes of improving current estimates of the Hubble constant. Figure 2.5 illustrates the current estimates of H_0 from a number of quasar systems.

Microlensing

In addition to cosmological applications, strong gravitational lensing can be used in a much more local context by looking at the lensing of stars by other stars. Formally, this is also in the strong lensing regime bu, realistically, the image separations are much too small to be observed. However, the lensing of a star by mass along the line of sight can cause a temporary boost in the luminosity of that star. This type of event, with micro to milli-arcsecond separations is called microlensing, and produces a characteristic light curve.

Initially suggested by Paczynski (1986) the method is this, if there are massive compact objects in the halo (MACHOs) of our galaxy we should be able to find them by looking for microlensing of the stars in our neighbouring satellite galaxies, the Large and Small Magellanic Clouds. Gravitational microlensing can be used to detect masses ranging from roughly $10^{-6}\mathrm{M}_{\odot}$ to $10^{6}\mathrm{M}_{\odot}$. Microlensing occurs in two regimes: cosmological and local. We will not discuss cosmological microlensing here, but this occurs when distant quasar strong lensing is affected by small mass concentrations within the lens. This has an impact on the detected light curves from distant quasars. Local, “galactic” microlensing occurs when stars in our galaxy lens those in either the Galactic bulge, Galactic halo or the nearby Magellanic Clouds or Andromeda galaxies.

Galactic microlensing occurs when a small (much smaller than the Ein-

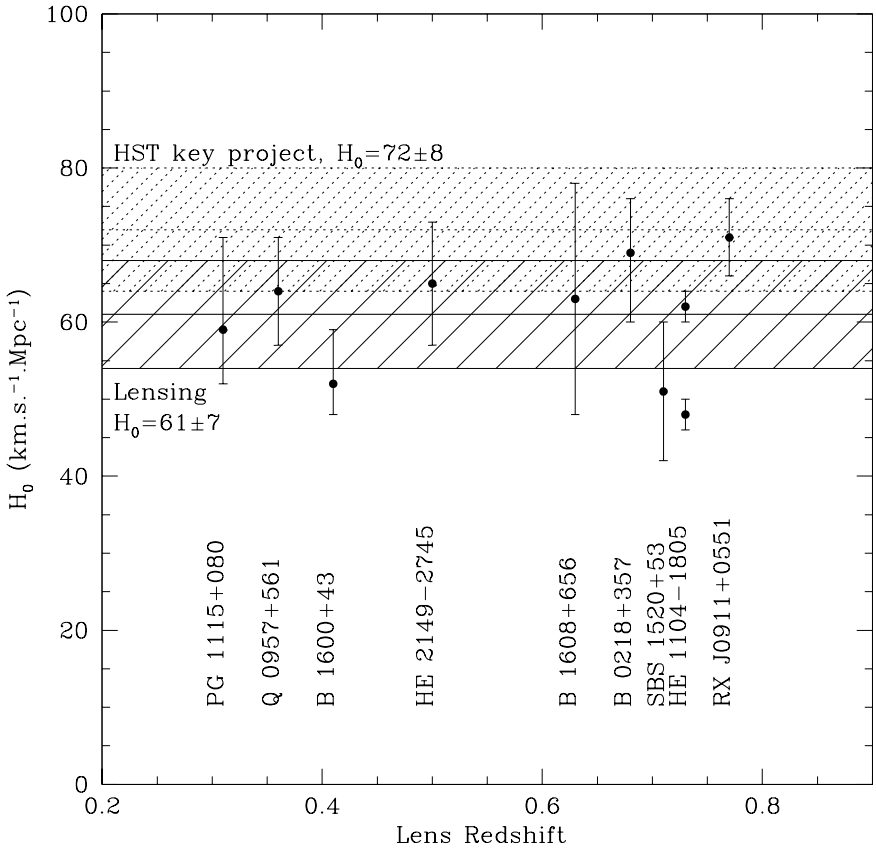

Figure 2.5: Quasar constraints on H_0 versus the result from the HST Key Project using Cepheid Variable Stars as distance indicators (Courbin, 2003)

stein radius) object passes between us, the observer, and a more distant star. If the halo of our galaxy were full of compact massive objects, such as stellar black holes, then we would expect distant stars to occasionally pass behind this dark matter and for a microlensing event to occur. This idea has been the catalyst for several large observational survey programs to monitor millions of stars and look for the signature light curve of a microlensing event. The most well-known of these surveys is the MACHO project, which after 5.7 years of observing has detected between 13 and 17 microlensing events towards the Large Magellanic Cloud (Alcock et al., 2001b). These results can be used to estimate the amount of dark matter in MACHOs, and it is clear that these high-mass objects do not account for most of the galactic dark matter (Alcock et al., 2001a).

2.3 Weak Lensing

Weak gravitational lensing is the small coherent distortion of background sources caused by foreground lenses. The lenses can be any mass concentration including galaxies, galaxy groups, galaxy clusters, or even the large scale network of structure in the universe. If there existed a dense sample of perfectly circular sources on the sky, then the shape of every source could directly be used to probe the mass along the line of sight. However, the densest sample of sources on the sky is galaxies, which are intrinsically elliptical in projected shape. This means that the signal-to-noise of measuring the shape of one distant galaxy is $\ll$1. The scatter in the shapes of galaxies is on the order of $\sim 30\%$ and the weak lensing distortion signal is an approximately 1% effect; thus the shapes

of many galaxies must be measured in order to accumulate a statistically significant signal.

Weak gravitational lensing is statistical in nature, and thus is often used to study ensemble averaged properties for a population. Individual rich galaxy clusters, however, can be detected through weak lensing and their internal mass distributions can be measured. Weak lensing can also be induced by individual galaxies lensing distant background galaxies. This is referred to as galaxy-galaxy lensing and is a powerful tool to probe the dark matter distribution on galaxy scales. The large scale structure of the universe (the complex network of filaments, clusters and voids) can induce a distortion pattern in background galaxies. This type of weak lensing is usually called *cosmic shear*, and can be used to probe cosmological parameters such as Ω_m and w, the dark energy equation of state.

2.3.1 History

While gravitational lensing was first detected with the famous 1919 solar eclipse and the first multiply imaged quasar was observed in 1979 (Walsh et al., 1979), weak lensing has only recently been used extensively for cosmology. The first use of weak gravitational lensing was in 1990 (Tyson et al., 1990) where background sources were found to be aligned tangentially to a rich cluster. This first detection did not have the statistics to constrain the dark matter well but many improved measurements have since been made. The first attempt at detecting a galaxy-galaxy lensing effect was reported by Tyson et al. (1984), but the images were from photographic plates and in relatively poor seeing, and no signal

was found. The first detection of galaxy-galaxy lensing was report by Brainerd et al. (1996). In the last 15 years many more detections of weak lensing been made, and the the methods used to detect and analyze the signal have greatly improved.

2.3.2 How to Measure Weak Lensing

The basic idea of weak lensing is quite simple. The shapes of distant source galaxies are distorted by foreground mass concentrations. If you can accurately measure these distortions then you can map out the foreground mass. In reality, this situation is complicated by the fact that the unlensed shapes of the sources are unknown and there are other possible ways the galaxy shapes could appear distorted. For example, the shapes of galaxies can be distorted by both the atmosphere of the Earth and the optics of the telescope and camera, because, all of the objects in the image have been convolved with the point spread function (PSF) of the atmosphere and optics.

In order to proceed from raw measurements taken from the images to a final shear estimate a number of techniques have been developed. It is important to note that regardless of how the analysis is done, weak lensing benefits greatly from using the highest quality images available. Deep, wide-field, sub-arcsecond seeing images will improve both the statistics and the systematic errors. The images used in weak lensing are generally taken in optical bands using a CCD camera. To get from images to galaxy shape (ellipticity) measurements, you must do basic data reductions, detect objects in the images, determine the shapes and finally correct them for the influence of the PSF as

will be described. The basic data reduction is fairly standard and includes removing the bias and flat-fielding. In addition, most images are collected with a dither pattern to allow for filling in the gaps between CCD chips and the elimination of bad pixels. The dithered images must be combined very carefully to make sure that the shapes of galaxies are not changed by the stacking procedure. With modern large mosaiced CCD cameras the distortion across a field may be quite large and must be mapped accurately in the stacking process.

The stacked images are then used to detect galaxies and the shapes of these galaxies are measured. This step is complicated by the fact that galaxies will not all appear totally isolated on the images, particularly in the very deep images generally used in weak lensing studies. Furthermore, the galaxies must be distinguished from stars, which will also be visible in the images. This is not a significant problem since stars will all appear to have the same size in the images, and their number density is much lower than that of galaxies at faint magnitudes and high latitudes.

There are a number of ways to detect the galaxies and correct their shapes but we will discuss in detail the Kaiser, Squires, & Broadhurst (1995) (KSB) method which was used in the observational projects which will be discussed in chapters 3-5. It is important to note that the analysis techniques for weak lensing have been rapidly improving in unison with the growth in technology. It is now relatively easy to obtain wide-field, high-quality images in multiple filters, ideally suited for lensing analysis.

KSB method

The KSB method of weak lensing analysis has been extensively used since its publication in 1995, and many others have added their own improvements to the technique (Luppino and Kaiser, 1997; Hoekstra et al., 1998). KSB is implemented in a software package called imcat (http://www.ifa.hawaii.edu/ kaiser), and is both an object detection and shape measurement tool. This method detects objects by filtering the images with a Gaussian filter and picking up the peaks. The images are smoothed with Gaussian filters of progressively larger radius and the significance of each peak is calculated. For each object the peak of greatest significance is added to a catalogue. This method then gives a position and size for each object. This information can then be fed into a photometry tool in order to measure the light content of each detected object. The software allows the user to select the significance of the peaks required in order to be added to the catalogue.

The shapes of galaxies are parametrized by a two-component "polarization". The polarization components are the combinations of the trace-free parts of their weighted quadrupole moments.

$$Q_{ij} = \frac{\int d^2\theta W(\theta) I(\theta) \theta_i \theta_j}{\int d^2\theta W(\theta) I(\theta)} \tag{2.17}$$

where I is the surface brightness of the galaxy, W is a Gaussian weight function of size r_g, and (θ_1,θ_2)=(0,0) is the assumed centre of the object. The polarization components, e_1 and e_2 are as follows

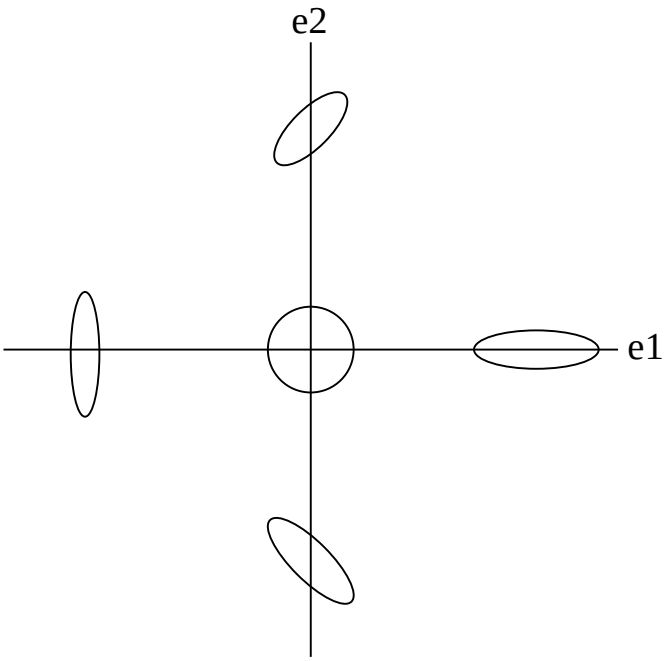

Figure 2.6: Polarization values for a variety of galaxy shapes.

$$e_1 = \frac{Q_{11} - Q_{22}}{Q_{11} + Q_{22}} \tag{2.18}$$

$$e_2 = \frac{2Q_{12}}{Q_{11} + Q_{22}} \tag{2.19}$$

The relationship between polarization and galaxy shape can be seen in Figure 2.6. In the absence of lensing these components average to zero, and thus you can look for a lensing signal by detecting a non-zero average polarization for a large number of background sources.

The basic KSB method detects objects, measures their raw ellipticities and then applies corrections to them to account for the PSF and any camera distor-

tions. The major drawback for the KSB method is that it does not work well with very anisotropic PSFs. This is generally not a problem for ground-based observations where the PSF is very nearly Gaussian, but for space-based observations this technique is not sufficient, and improvements have been made to deal with more complicated PSFs (Hoekstra et al., 1998; Rhodes et al., 2000).

Implementation

The raw shape measurements are e_1 and e_2, as defined in equations 2.18 and 2.19. In order to get from the measured shapes to the true shapes it is necessary to account for the smearing caused by the isotropic component of the PSF, any non-isotropic component of the PSF and the camera distortions. The smearing can be corrected for by observing the stars in the field. In order for this to work there must be a sufficiently high density of stars in the image to accurately map out the PSF as a function of position. For some data this might not possible, in which case calibration images of star fields should be taken simultaneously with the lensing observations in order to accurately measure the stellar PSF at the time of observations. The details of the correction can be found in KSB (1995) and Hoekstra et al. (1998).

The final shear estimate, γ, from the polarization measurement is

$$\gamma = \frac{e^{obs} - p^{sm} p}{P^{\gamma}} \tag{2.20}$$

where e^{obs} is the observed polarization, p^{sm} is the smear polarizability, p is calculated from the stars and P^{γ} is defined in equation 2.22. The quantity p is defined by

$$p = \frac{e^*}{p_*^{sm}} \tag{2.21}$$

where e^* is the polarization of the stars in the images and P_*^{sm} is the smear polarizability of the stars. The quantity P^γ is defined by

$$P^\gamma = p^{sh} - \frac{p_*^{sh}}{p_*^{sm}} p^{sm} \tag{2.22}$$

where p^{sh} is the shear polarizability and asterisks always refer to stars. The shear polarizability is used to calculate the "pre-seeing" shapes of objects. Seeing tends to circularize objects and needs to be removed from the shape measurements. The smear and shear polarizability can be measured for each individual object. P^γ is noisy for individual sources and so it is usually fit in bins of magnitude and r_g and then applied to the data.

2.3.3 Applications

Cluster Mass Reconstruction

Strong lensing can be used to map the mass distribution in galaxy clusters, as was discussed in Section 2.2.. This method, while very useful, generally only constrains the central regions of galaxy clusters, and it is only applicable where arcs are found. On the other hand, every cluster will weakly distort the distant galaxies behind it on the sky. This weak lensing signal can be inverted in order to reconstruct the cluster mass distribution (Kaiser and Squires, 1993). Sources that are in the background of the lens will be distorted and show a preferred

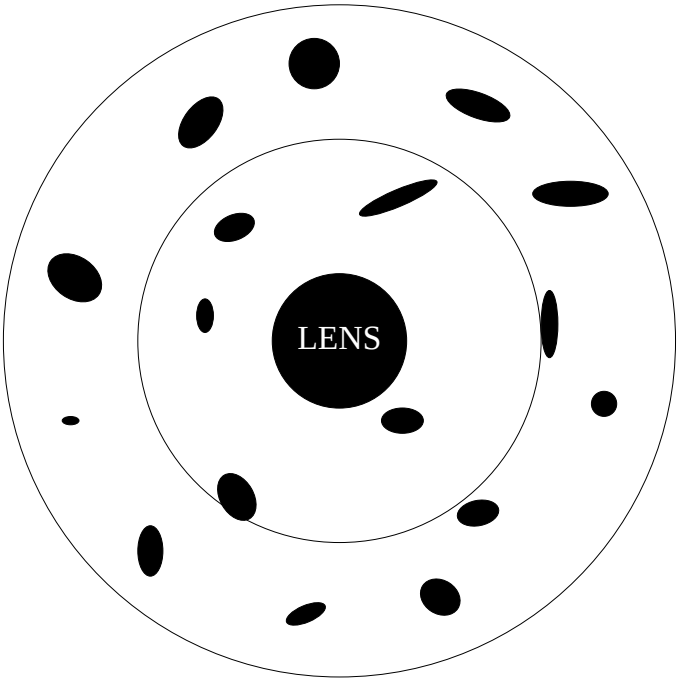

Figure 2.7: Weak lensing schematic. The tangential component of the shear is calculated in radial annuli centred on the lens

alignment tangential to the mass concentration of the cluster (see schematic in Figure 2.7). The cluster masses derived from weak lensing agree very well with those from x-ray estimates (Mellier, 1999).

The method of inverting the shear map into a mass profile was pioneered by Kaiser & Squires (1993). The technique uses the fact that the shear, γ, is a convolution of the surface mass density κ with the kernel D (see Mellier, 1999))

$$\gamma(\theta) = \frac{1}{\pi} \int D(\theta - \theta')\kappa(\theta')d^2\theta' \tag{2.23}$$

This relation is easily inverted in Fourier space to return the surface mass density in terms of a linear function of the shear

$$\kappa(\theta) = \frac{1}{\pi} \int \Re[D(\theta - \theta')\gamma(\theta')] d^2\theta' + \kappa_0 \tag{2.24}$$

where $\Re$ represents the real part. The κ_0 is necessary because lensing measurements are subject to a "mass-sheet degeneracy". The shear signal is not affected by adding a sheet of constant surface mass density, so that the mass recovered is not unique, unless this degeneracy can be broken. In addition, lensing measurements are sensitive to the *projected* mass density which can make comparisons with other measurements, such as x-ray masses, more complicated.

Hence, if the shear can be observed from image distortions, the surface mass density can be reconstructed. Mass reconstruction techniques were implemented first on cluster scales because the weak lensing is not so weak ($\kappa \sim 0.1$). This method has been successfully used to map the dark matter distribution in many clusters (Fahlman et al., 1994; Luppino and Kaiser, 1997; Hoekstra et al., 1998; Hoekstra et al., 2000).

A sample shear map and mass map can be found in Figure 2.8. The tangential shear profile can be fit with an isothermal sphere as in equation 2.16 in order to estimate the Einstein radius (see Figure 2.9a). In order to convert the isothermal sphere fit to a velocity dispersion, and hence a mass, the redshift must be estimated for the lens and source because of the angular diameter distance dependence, D_{LS}/D_S (characterized by the parameter β in equation 2.25) in equation 2.5. The redshifts of the sources are often estimated by the

magnitude limit of the observations, or if multiple-filter data are available then photometric redshifts can be estimated. The important thing is to understand the distant source redshift distribution. The redshifts of the cluster lenses are almost always known spectroscopically. For very deep observations there may not be calibrated photometric redshifts available, and so the redshift distribution of the faint sources may have to be roughly estimated simply from the observed magnitude.

$$\beta = \max\left[0, \frac{\mathrm{D_{LS}}}{\mathrm{D_S}}\right], \tag{2.25}$$

where the angular diameter distances are shown in Figure 2.1.

The method introduced by Fahlman et al. (1994) uses a slightly more robust statistic which is a measure of the radial surface density profile ζ

$$\zeta(r, r_{\max}) = \frac{1}{1-(r/r_{\max})^2}\int_r^{r_{\max}} d\mathrm{ln(r)}<\gamma_\mathrm{T}> \tag{2.26}$$

where γ_T is the tangential shear, averaged in annular bins.

$$\gamma_T = -(\gamma_1 \cos 2\phi + \gamma_2 \sin 2\phi) \tag{2.27}$$

ζ gives the mean surface density interior to r relative to the mean in the annulus from r to $r_{\max}$.

$$\zeta(r, r_{\max}) = \bar{\kappa}(r' < r) - \bar{\kappa}(r < r' < r_{\max}) \tag{2.28}$$

ζ provides a lower bound on the average dimensionless surface density, $\bar{\kappa}(r)$, within radius r and therefore on the mass within that aperture. The aperture mass is independent of the addition of a sheet of constant surface mass density so that the additive term in equation 2.24 drops out. A plot of the aperture mass for the cluster 1358+62 can be seen in figure 2.9. The ζ statistic leads directly to the mass estimate within an aperture

$$M(< r) = \pi r^2 \zeta(r) \Sigma_{crit} \tag{2.29}$$

The Kaiser & Squires weak lensing method appears to work well in reconstructing the mass profiles of galaxy clusters using only the shapes of distant source galaxies. The weak lensing signal is noisy at small radii because of the small number of background galaxies, and due to the contamination from cluster member galaxies. Furthermore, the assumption of weak lensing that $\kappa \ll 1$ is not valid in the inner-most regions of a cluster. One way to improve our understanding of cluster mass distributions is to use weak and strong lensing together to constrain the mass. This of course can only be done for clusters where arcs have been identified, but for all such systems the weak lensing distortion can be measured. The combination of weak and strong lensing can also eliminate the "mass-sheet degeneracy" alluded to in equation 2.24 (Bradac et al., 2005).

Another application of cluster weak lensing is to blindly search for clusters without relying on visible signatures such as an overabundance of red galaxies, or extended x-ray flux. These searches operate in much the same way that cosmic shear surveys do. Large blank patches of the sky are observed and

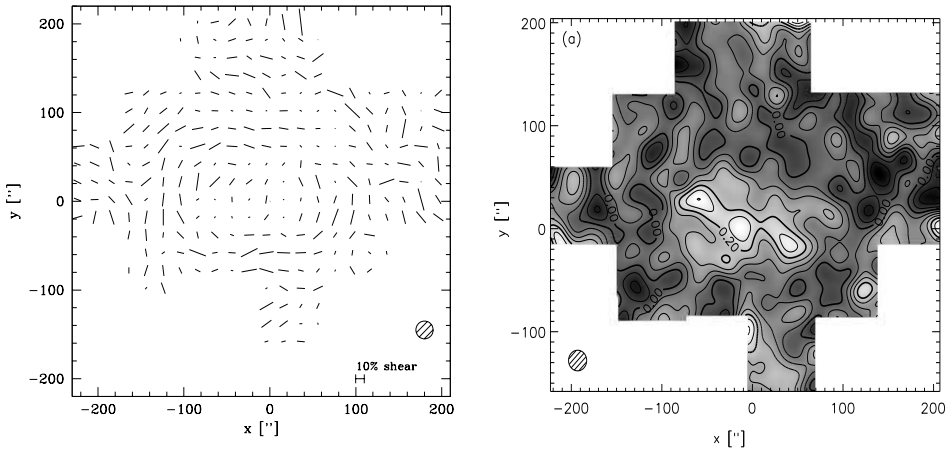

Figure 2.8: On the left: smoothed shear map for MS 1054-03, obtained from the corrected shapes of background sources. The orientation of the sticks indicates the direction of the shear, while the length represents the amplitude. Due to lensing, the "sticks" tend to align tangentially to the cluster centre. The shaded circle indicates the size of the smoothing filter used. On the right: Reconstructed mass contours for MS 1054-03. The signal-to-noise is highest in the middle of the frame where a clear mass concentration is visible. (Hoekstra et al., 2000)

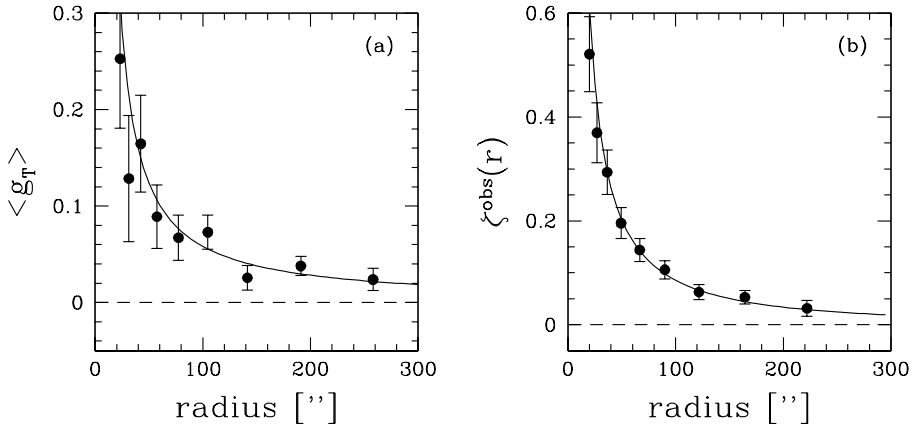

Figure 2.9: (a) Average tangential shear around a cluster of galaxies. The best fit isothermal sphere is shown with the solid line. (b) $\zeta(r)$ statistic profile, again showing the best fit isothermal sphere as a solid line, corresponding a velocity dispersion of 780$\pm$60 km s^{-1} (Hoekstra et al., 1998).

the shapes of distant source galaxies are accurately determined. Using the shear to mass inversion technique outlined above (Kaiser & Squires, 1993), the shear fields can be used to detected the mass peaks. This method can be used to search for clusters, and produces a shear-selected sample (Miyasaki et al., 2005). Such surveys will not be sensitive to low mass clusters, but will be invaluable for locating the most massive clusters in the universe, which are also the largest collapsed objects, and hence critical for studies of structure evolution.

Galaxy-Galaxy Lensing

Galaxies are the basic building blocks of the luminous structures in the universe, and yet some of their basic physical attributes, such as their masses and radial extents have only recently become observationally accessible. The importance of halo structure is two-fold: for an understanding of the dark matter itself and the sequence of hierarchical growth, and because of its influence in the process of disk formation. While rotation curves constrain the dark matter content in the inner region of spiral galaxies, they fail at large radii where there are few visible tracers. Similarly, dynamical mass estimates probe only the inner region of dark matter halos and are highly dependent on equilibrium assumptions. Gravitational lensing has the advantage that it can trace the dark matter distribution to large radii where there are few tracer populations.

Measurements of the dark matter halo are critical for a comprehensive understanding of the formation and evolution of baryonic disks, as discussed in Chapter 1. There are many outstanding puzzles related to the formation of disks

including: the cooling of gas in the dark matter halos, how angular momentum is transferred during this process, the effect of feedback and the dynamical response of the dark matter halo to this "adiabatic" contraction of the baryons. If we could determine the baryonic fraction as a function of total mass from observations of galaxies it would be possible to place tight constraints on the the efficiencies of cooling and feedback (van den Bosch et al., 2003). Unlike kinematics or dynamics, weak gravitational lensing provides us with a method to determine the total or "virial" mass of galaxy halos. These masses are vital for comparison to the results of numerical and semi-analytic simulations.

The weak lensing signal from a rich cluster is adequate to map the projected matter distribution. This is not the case for individual galaxies, which are not sufficiently massive for the distortion pattern to be detected. The signal-to-noise for an individual galaxy halo is $\ll 1$ (Bartelmann and Schneider, 2001). While weak lensing can not be used to map the matter distributions for individual galaxies it can detect ensemble averaged properties for a large sample of galaxies. The weak lensing patterns around many galaxies can be stacked together and the average shear profile can be estimated. If there is a sufficiently large sample of foreground galaxies to act as lenses, then the sample can be split into different morphology, luminosity or redshift bins in order to look for variations in the average dark matter profiles.

The ideal galaxy-galaxy lensing survey will have wide-field, deep data with a redshift for every object in the field of view to allow proper division into lens and source samples. Unlike the case of cluster weak lensing the redshifts of the lenses are often not known. There have been examples of galaxy-galaxy lensing measurements using small areas with spectroscopic redshift information

(McKay et al., 2001; Smith et al., 2001; Hoekstra et al., 2003; Sheldon et al., 2004), but generally the redshifts must be estimated based upon photometry. If there is multi-band data then photometric redshifts can be used to estimate the redshifts of both lenses and sources (Hudson et al., 1998; Wilson et al., 2001), but if there is only imaging in one band then assumptions about the lens and source redshift distributions must be made.

The amplitude of the weak lensing signal from a singular isothermal sphere (with projected mass profile defined in 2.8) is a function of redshift through the angular diameter distances of the lenses and sources (equations 2.5, 2.25). If no colour information is available then the redshift distributions can be estimated from the magnitude limits of the sample. For example, if the limiting magnitude of the lens sample is 21.5 in R_c then another survey of the same depth with known redshifts can be used to estimate the redshift distribution. This is certainly possible for the lens populations but for very deep surveys there may not be appropriate redshift surveys to estimate the redshift distribution of the very faint background sources. An alternative method is to use galaxy formation simulations to estimate the redshift distribution based on the observed magnitude in a particular band, but this is subject to much uncertainty. If estimated redshift distributions for the lenses and sources are assumed based solely on their observed magnitudes, then there will be some small overlap in the samples. For example, most faint galaxies will be at high redshift, but some may be faint foreground galaxies which should not be in the source sample, but without redshift information this discrimination can not be made. The interpretation of the ensemble averaged galaxy halo properties is complicated when there is little redshift information, but useful constraints can still be obtained (Hoekstra

et al., 2004).

Since galaxy-galaxy lensing is used to measure the average properties of a sample of lenses, the differences between the lenses must be accounted for in the analysis. A quantitative analysis of the lensing signal must account for the fact that the foreground lenses are not identical. Therefore, the mass properties of galaxies have to be parameterized in order to allow the joint analysis of the foreground galaxy population. In particular, one is interested in the velocity dispersion of a typical L_* galaxy, where L_* defines the luminosity above which there is a sharp cut-off in the galaxy population. Assuming a scaling between velocity dispersion and luminosity ($\sigma \propto L^{1/4}$, for example) the lensing results can be scaled to an L_* value (Hudson et al., 1998; Hoekstra et al., 2004; Kleinheinrich et al., 2005), and therefore be compared with other lensing, and non-lensing measurements. Alternatively, the results can be binned by luminosity (McKay et al., 2001) in order to detect differences in the galaxy-mass correlation function between different populations of galaxies.

Halo Sizes One of the goals of galaxy-galaxy lensing is to measure the extent of galaxy dark matter halos. This is a particularly difficult problem because at large projected radii from the lens centre, the shear induced by the lens is very small, and in addition, there will be other concentrations of mass contributing to the signal, which makes interpretation of the shear profile more challenging. At large radii the observed tangential shear is likely coming from multiple sources especially nearby dark matter halos. These results can therefore be best interpreted by studying the galaxy-mass cross-correlation function.

The tangential shear γ_T can be thought of as the galaxy-shear correlation

function which can then be related to the galaxy-mass correlation function, ξ_{gm}. For large samples of lenses there will be both faint nearby galaxies and more luminous distant galaxies in the sample. This complicates the interpretation of ξ_{gm} because there will be galaxies in the sample with inherently different clustering properties. The galaxy-mass cross-correlation is also useful in computing the bias parameter, b, which is usually defined as

$$\mathrm{b}^2 = \frac{\xi_{\mathrm{gg}}}{\xi_{\mathrm{mm}}}, \tag{2.30}$$

where ξ_{gg} is the correlation function for luminous galaxies and ξ_{mm} is the correlation function for dark matter. The bias parameter measures the extent to which mass follows light

The combination of the galaxy-mass correlation function , ξ_{gm}, and the galaxy-galaxy correlation function, ξ_{gg}, can be used to estimate b through the equation

$$\frac{\xi_{gg}}{\xi_{gm}} = \frac{\mathrm{b}}{R} \tag{2.31}$$

where R is the correlation coefficient. The correlation functions can both be measured from the lensing data, provided there are redshift estimates for the foreground and background galaxies. The galaxy-mass correlation function has now successfully been used to estimate the bias-parameter in weak lensing studies. Hoekstra et al (2002) used data from the Red Sequence Cluster Survey and Sheldon et al.(2004) used the SDSS to estimate b/R=1.09$\pm$0.04 and 1.1$\pm$0.2 respectively. Both b and R are scale-dependent and these quoted val-

ues are average values out to $\sim 10h^{-1}$Mpc. The biasing will be different for different galaxy types and thus the interpretation of b/R is non-trivial.

Halo Shapes An important characteristic of dark matter halos is their shape. We know that projected galaxy shapes on the sky are elliptical, but the shapes of their dark matter halos are unknown. Numerical simulations can predict the shapes but comparing these to observed halo shapes is an important constraint on CDM models. Weak lensing has the potential to make this important measurement. There have been hints of non-spherical halos from x-ray isophotes, for example, but most dynamical, kinematic and lensing measurements assume spherical halos.

The simplest way to measure the halo shape from weak lensing was suggested by Brainerd & Wright (2000). The tangential shear signal can be compared for samples of sources close to the major axes of the lenses versus those close to the minor axes (Figure 2.10). The difference in the signal from the 2 regions can be used to estimate the flattening of galaxy dark matter halos. This technique was used by Hoekstra et al. (2004), who found a significant detection of dark matter halo flattening, indicating that halos have on average an ellipticity of $0.33^{+0.07}_{-0.09}$ and that they are aligned with the light distribution of galaxies. Hoekstra et al. estimated a flattening parameter, f, based on the assumption that the ellipticity of dark matter halos is related to the observed ellipticity of the lens as $e_{\rm halo} = f e_{\rm lens}$. They found that $f = 0.77^{+0.18}_{-0.21}$ and excluded flat dark matter halos ($f = 0$) at the 3-σ level. This intriguing result was contradicted in the latest SDSS galaxy-galaxy lensing analysis (Mandelbaum et al., 2005), who found no significant flattening. The analysis techniques em-

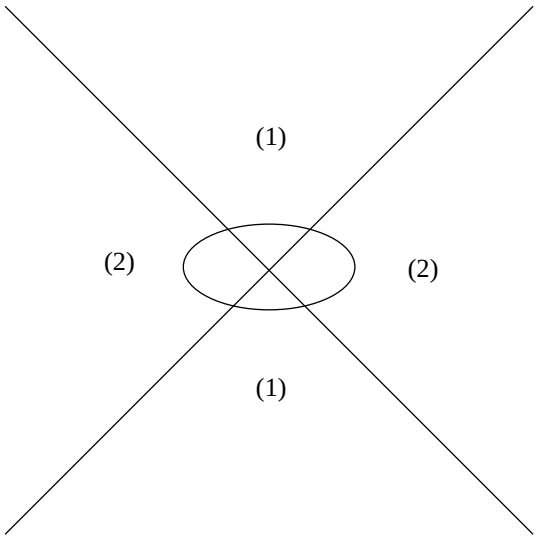

Figure 2.10: Schematic of anisotropic weak lensing. The lensing signal from sources in regions labelled (1) and (2) are measured separately and compared in order to estimate the flattening of galaxy dark matter halos

ployed in these two measurement were significantly different, however. We will attempt to measure the flattening of galaxy halos in the Canada France Hawaii Telescope Legacy Survey lensing analysis to be presented in Chapter 5.

Systematic Errors Any time weak lensing is used to estimate the shear around a mass concentration there is a built-in systematic test. If the phase of the distortion is increased by $\pi/2$ (this is equivalent to rotating all images by 45°) then the resulting signal should vanish if the tangential shear measured is truly due to gravity. This provides a quick way to test for some systematic effects. An additional method that can be used in galaxy-galaxy lensing studies is to search

for a signal around random points. The amplitude of this signal should be very small and should not produce a radial profile. These tests applied to analysis using the KSB method consistently indicate that systematics are indeed very small. See Figure 4.1 to see tangential and "cross" shear for our sample of galaxy groups.

Weak gravitational lensing is reliant upon accurate galaxy shape measurements and the assumption that galaxy shapes are not aligned at large separations. Nearby galaxies can be aligned because they formed in similar and related gravitational fields. If indeed galaxies are aligned at large separations then the interpretation of a weak lensing signal is complicated. Galaxy-galaxy lensing is particularly susceptible to intrinsic alignments if no redshift information is available for the lenses. If the lenses and sources are separated based only upon their apparent magnitudes, then some sources may be physically associated with some lenses. If satellite galaxies are either aligned or anti-aligned to their host galaxies this will influence the tangential shear measurements.

Recent results based on the 2dF Galaxy Redshift Survey indicated that there was no alignment between satellites and their host, suggesting that the contamination to galaxy-galaxy lensing measurements by satellites is minimal (Bernstein and Norberg, 2002) . Results from the SDSS (Agustsson and Brainerd, 2005) suggest that there is a radial alignment between satellites and hosts and therefore the tangential lensing signal is systematically suppressed. These contradictory results indicate the importance of obtaining photometric redshifts to clearly separate lenses and sources.

Galaxy Groups The lensing induced by individual galaxy groups is also too small to be observed for individual systems, and the signal from a sample of groups must be stacked together. In this sense galaxy-group weak lensing is very similar to galaxy-galaxy lensing. The first group weak lensing measurement (Hoekstra et al., 2001) was able to detect a signal, but at a low significance for all groups stacked together. We (Parker et al., 2005) were able to make a much more significant detection of group weak lensing and calculate the radial profile of the M/L ratio. In addition, we had sufficient signal to divide our groups into two different mass bins as will be discussed in Chapter 4.

Cosmic Shear

In addition to tangential shear around foreground objects there is a coherent distortion of background galaxies caused by the large scale distribution of structure along the line of sight (see Figure 2.11). This signal is very small, but understanding its statistical properties provides a new way to estimate cosmological parameters such as σ_8 and Ω_m. The amount of this shear depends on the integral of the gravitational potential along the line of sight and the redshifts of the sources. By studying the shear of many galaxies one can statistically infer the amount of dark matter as a function of position and time to constrain its properties, spatial distribution and evolution. Numerous large surveys devoted to the study of cosmic shear are underway, including, notably the Canada-France-Hawaii Telescope Legacy Survey. Cosmic shear is particularly powerful because it can be used to estimate cosmological parameters without the unknown biases inherent in the light distribution of galaxies. Weak lens-

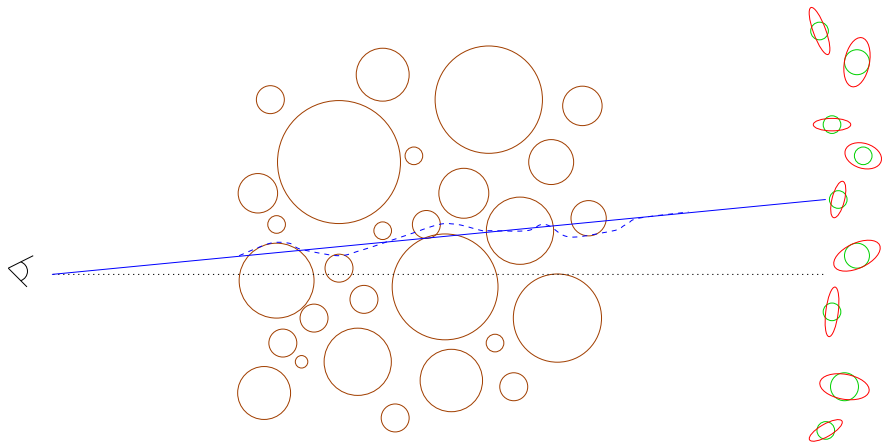

Figure 2.11: Schematic illustration of the effect of weak lensing by large-scale structure. The photon trajectories from distant galaxies (right) to the observer (left) are deflected by intervening large-scale structure (centre). This results in coherent distortions in the observed shapes of the galaxies. These distortions, or shears, are on the order of a few percent in amplitude and can be measured to yield a direct map of the distribution of mass in the universe (Refregier, 2003).

ing is particularly sensitive to σ_8 which is vital to cosmology, because even if all fundamental cosmological parameters are known with great precision, σ_8 is still necessary to normalize the matter power spectrum. There has also been considerable interest in using cosmic shear as a probe of "dark energy" (Benabed and van Waerbeke, 2004).

While cosmic shear studies are of great interest to cosmology, the measurement is not an easy one to make. The signal is smaller than the signal from cluster or galaxy-galaxy weak lensing and requires deep multi-filter data covering wide areas of the sky. Until recently obtaining wide-field high quality

data was very time-expensive and the tools did not all exist to extract and interpret this tiny signal. The basic idea of cosmic shear is to map out the shear field from galaxy ellipticities and look for correlations in the shapes. An example shear map can be seen in Figure 2.12.

Despite the challenges inherent in measuring cosmic shear, there have now been many successful detections (see Heymans et al., 2005 for a recent discussion). There are ongoing and planned surveys which are much larger and should be able to estimate cosmological parameters with precision better than other cosmological probes. The cosmic shear signal can be quantified in a number of different ways. One of the most popular is to measure "shear correlation functions". These correlation functions can be related to the matter power spectrum and used to estimate cosmological parameters. The shear signal can be divided into a gradient, or "E"-mode signal, and a curl, or "B-" mode (see Figure 2.13). The E-mode is the gravitational lensing signal while the B-mode provides a systematic error check. If the observed shear is due to gravity through lensing then it should be curl-free and hence the B-mode should be zero.

Each cosmic shear survey uses its own analysis tools including unique methods for PSF correction and weighting of distant sources. In order to try and ascertain the optimal method for analyzing cosmic shear data a collaboration has been established to test each pipeline on both real and simulated data. The simulated data have the advantage that the input shear signal is known precisely and so the pipeline which can recover that signal is the "best" method. This project was motivated by the apparent lack of agreement in the early cosmic shear surveys in regards to their σ_8 estimates (Heymans et al.,

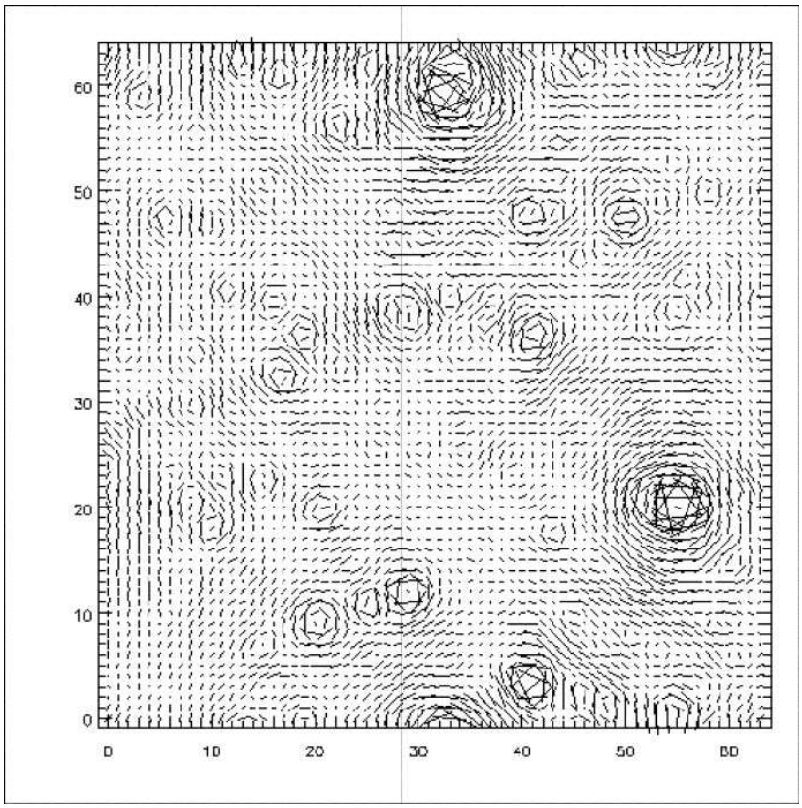

Figure 2.12: Simulated shear map for a 1 sq. degree field (Jain et al., 2000). The “sticks” are as in Figure 2.8. A few cluster masses are clearly visible by their tangential shear patterns.The root-mean-square of the shear in this map is $\sim$2%.

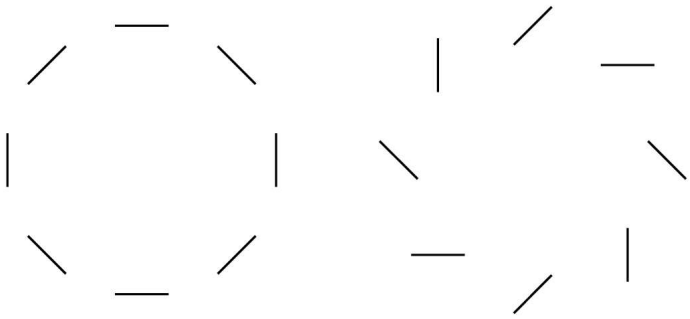

Figure 2.13: E- and B-mode shear signal. On the left is the tangential pattern of shear which would occur around an over-density. This is a pure E-mode signal from an isolated, spherically symmetric mass. On the right, a pure B-mode signal, which is not generated by lensing at lowest order, and is a built-on systematic error check for cosmic shear studies.

2005). These results are summarized in Table 2.3.3 from the review by Refregier (2003). The results from the Shear TEsting Programme (STEP) indicate that while new methods of weak lensing analysis show promise, the traditional KSB techniques, with appropriate weighting, recover the cosmic shear signal very accurately.

Summary and Outlook

This chapter has given a hint of the breadth of applications that gravitational lensing has in modern astrophysics; from trying to detect MACHO dark matter to estimating fundamental cosmological parameters. Lensing has a huge advantage over other observational tools because it can be used to directly detect the presence of matter without making any assumptions about M/L ratios or the dynamical state of a system. The weak lensing signal, however, is very small and the understanding and correction of systematic effects must be carefully considered.

Gravitational lensing is a rapidly evolving field with the potential to measure some cosmological parameters more precisely than has ever been done. In addition, weak gravitational lensing can be used to probe dark matter structures on scales where other techniques fail. Perhaps the most exciting aspect of lensing is its role in helping uncover some of the mysteries of galaxy formation. With ongoing and planned surveys it should be possible to estimate which types of galaxies live in which type of dark matter halos as a function of redshift. Furthermore, weak lensing can be used to constrain dark matter properties by studying the sizes and shapes of dark matter halos.

Reference	Telescope	Area (deg^2)	$\sigma_8{}^a$
Bacon et al. 2000	WHT	0.5	$1.50^{+0.50}_{-0.50}$
Maoli et al. 2001	VLT	0.65	$1.03^{+0.03}_{-0.03}$
Rhodes et al. 2001	HST/WFPC2	0.05	$0.91^{+0.25}_{-0.30}$
van Waerbeke et al. 2001a	CFHT	6.5	$0.88^{+0.02}_{-0.02}$
Hoekstra et al. 2002a	CFHT, CTIO	24	$0.81^{+0.07}_{-0.09}$
van Waerbeke et al. 2002a	CFHT	8.5	$0.98^{+0.06}_{-0.06}$
Refregier et al. 2002	HST/WFPC2	0.36	$0.94^{+0.14}_{-0.14}$
Bacon et al. 2005	WHT, Keck	1.6	$0.97^{+0.13}_{-0.13}$
Hoekstra et al. 2002b	CFHT, CTIO	53	$0.86^{+0.04}_{-0.05}$
Brown et al. 2003	MPG/ESO	1.25	$0.72^{+0.09}_{-0.09}$
Hamana et al. 2003	Subaru	2.1	$0.69^{+0.18}_{-0.13}$
Jarvis et al. 2003	CTIO	75	$0.71^{+0.06}_{-0.08}$

[a] for ΛCDM model with $\Omega_m = 0.3$, $\Omega_\Lambda = 0.7$; Γ is marginalised over or set to 0.21 when possible; errors correspond to 68%CL

Table 2.1: Current cosmic-shear surveys with σ_8 estimates, adapted from Refregier (2003).

The remainder of this thesis will deal with weak gravitational lensing and its applications to galaxies and galaxy groups at intermediate redshifts.

Chapter 3

CNOC2 Galaxy Groups: Observations and Data Reduction

Detection is, or ought to be, an exact science, and should be treated in the same cold and unemotional manner. You have attempted to tinge it with romanticism, which produces much the same effect as if you worked a love-story or an elopement into the fifth proposition of Euclid.

— Sir Arthur Conan Doyle

3.1 Introduction

Although galaxy groups, with masses of $\sim 10^{13} M_{\odot}$, dominate the overall mass and luminosity densities of the universe, their properties are poorly understood in comparison to individual galaxies or rich galaxy clusters. To date, galaxy

groups have not been extensively used for cosmology, largely because they are notoriously difficult to identify due to their small contrast with the field. However, with large redshift surveys it is now possible to identify substantial samples of galaxy groups.

A sample of roughly 200 galaxy groups was identified in the Canadian Network for Observational Cosmology 2 (CNOC2) redshift survey using an iterative friends-of-friends algorithm (Carlberg et al., 2001). The dynamical analysis of these groups indicated a increasing mass-to-light ratio with radius. This suggests that groups are the scale where segregation begins to occur between mass and light. This effect could be due to dynamical friction, or to a large core radius which could indicate that dark matter has different properties from "standard" collisionless cold dark matter (CDM). The cores of galaxies and clusters appear to be less cuspy than expected, which has prompted theoretical work in alternative dark matter models (see discussion in Governato et al. (2001)).

The dark matter density profile has yet to be measured for galaxy groups. Dynamical studies of groups are difficult because kinematic information is known for very few galaxies, and because equilibrium assumptions might not be valid. Furthermore, these difficulties increase at large radii from the group centre. Weak gravitational lensing has proven invaluable in the analysis of single massive objects such as galaxy clusters (Hoekstra et al., 1998; Mellier, 1999) as well as in the statistical studies of individual galaxies (Brainerd et al., 1996; Hudson et al., 1998; Fischer et al., 2000; Sheldon et al., 2004; Hoekstra et al., 2004). To date there has been only one weak lensing measurement of galaxy groups (Hoekstra et al., 2001) using a small subsample of the total

CNOC2 galaxy group catalogue.

In this chapter we will outline the data used in our weak lensing study of CNOC2 galaxy groups and in Chapter 4 we will provide lensing analysis details and discussion. Our results will be compared with those found from the dynamical measurements (Carlberg et al., 2001) and the weak lensing detection of Hoekstra et al. (2001). We will also present the results when the sample of groups is split into two sub-samples of "rich galaxy groups" and "poor galaxy groups".

3.2 CNOC2 Groups

Our galaxy group catalogues were generated using a friends-of-friends algorithm with the CNOC2 redshift survey data (Yee et al., 2000; Carlberg et al., 2001). The CNOC2 area contains 4 fields well-spaced in right ascension and was intended to study the properties of field galaxies, as opposed to the original CNOC survey which was intended to study galaxy clusters. The CNOC2 galaxy sample contains 6200 galaxies with redshifts in the range to $0.1 < z < 0.7$. From this galaxy catalogue a sample of 192 galaxy groups was identified. Identifying a sample of galaxy groups in a redshift survey is not an easy task since the redshifts of galaxies are known but not their precise physical radial distances. There can be velocity interlopers which corrupt the catalogue. In addition, dynamical studies of groups require the assumption that the systems are in dynamical equilibrium and thus a sample of "virialized" groups is desired, not just galaxies which are close to each other in space. The difficulty in

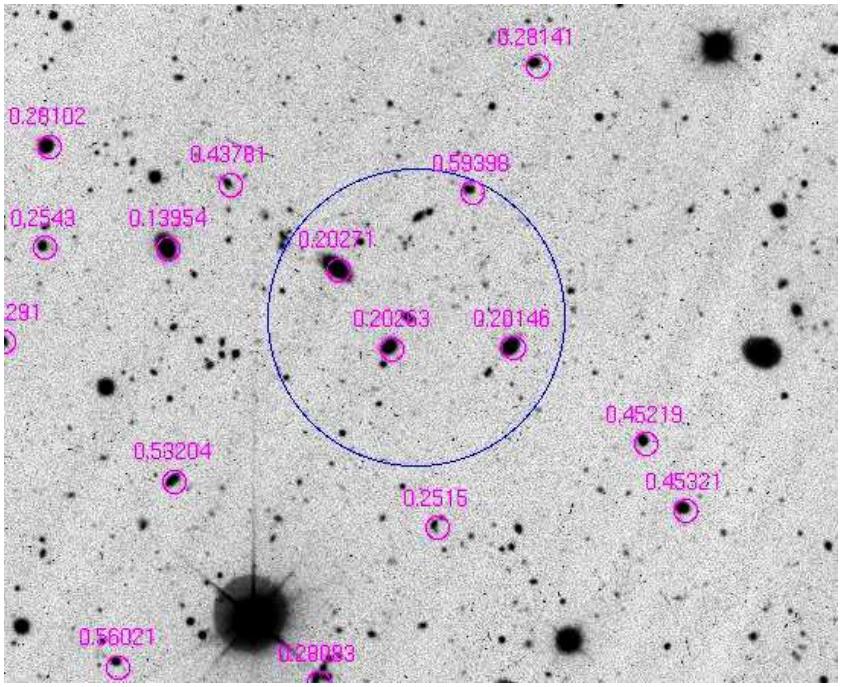

Figure 3.1: The CNOC2 galaxies, labelled by their redshifts. The large circle indicates the virial radius for one galaxy group. Without spectroscopic redshifts identifying these groups would not be possible.

identifying galaxy groups without redshift information can be seen in Figure 3.1. The group galaxies do not stand out clearly from the field galaxies.

The basic algorithm used by Carlberg et al. (2001) to identify groups is a variant of the"friends-of-friends" algorithm (Huchra and Geller, 1982) and is as follows:

- Choose a cosmology for the analysis. In this case the assumptions were Ω_m=0.2, $\Omega_\Lambda = 0, h = 1$. The final catalogue is, however, not very

sensitive to the choice of cosmology.

- Choose a redshift and magnitude limit for the sample. For this analysis all redshifts were included, but only galaxies brighter than M_R=-18.5 were included (resulting in a relatively complete sample).

- Pick a maximum projected radius (0.25 h^{-1}Mpc) and radial separation (5 h^{-1}Mpc).

- With each galaxy find all neighbours which meet the search criteria and add these to the group. Do this for each galaxy in the sample.

- Determine the weighted mean x,y,z and σ. Based on the calculated σ estimate r_{200} (the radius where the density is 200 times the critical density ρ_c). Add galaxies within some factor of r_{200} and with velocities within 3-σ and trim galaxies outside these limits. Repeat this process until the results are identical from one iteration to the next.

- Keep all groups with 3 or more members

The average number of galaxies identified in each group is $\sim$4 and the groups have a median redshift of 0.33. The groups have a median dynamically-determined velocity dispersion of 190 km s^{-1}. In chapter 4 we will analyze the weak lensing signal from the entire sample of groups, as well as two subsets divided by their median velocity dispersion. We call these subsets the "rich" and "poor" galaxy groups. The observed dynamical group properties can be found in Table 3.1.

Sample	$\bar{z}$	σ (km s^{-1})	N	M_{200} (h^{-1} $M_\odot$)	M/L (h $M_\odot/L_{\odot B}$)	r_{200} (Mpc)
All	0.32	218	3.9	2.1×10^{13}	288	0.28
Poor	0.30	128	3.6	5.2×10^{12}	96	0.17
Rich	0.34	316	4.1	3.8×10^{13}	496	0.39

Table 3.1: CNOC2 galaxy groups - mean properties

3.3 Observations

For this project we observed the 4 central patches of the CNOC2 fields, where most of the galaxy groups are located. One of the 4 fields is seen in Figure 3.2. The observations were carried out mostly at the Canada-France-Hawaii Telescope with 2 additional nights at the Kitt Peak National Observatory Mayall 4-m Telescope. The fields were observed in B,V,R_c, and I_c. Deep exposures ($\sim$4 hours) were taken in the R_c and I_c bands, which were used for the lensing measurements. The characteristics of the data obtained are outlined in Table 3.2.

3.4 Basic Reductions

The basic data reduction steps applied are standard for CCD image analysis. They include subtracting the readout bias, which is estimated from the overscan strip on each CCD. The observations described in this chapter were taken with mosaic cameras which are made up of many CCD chips. The other important

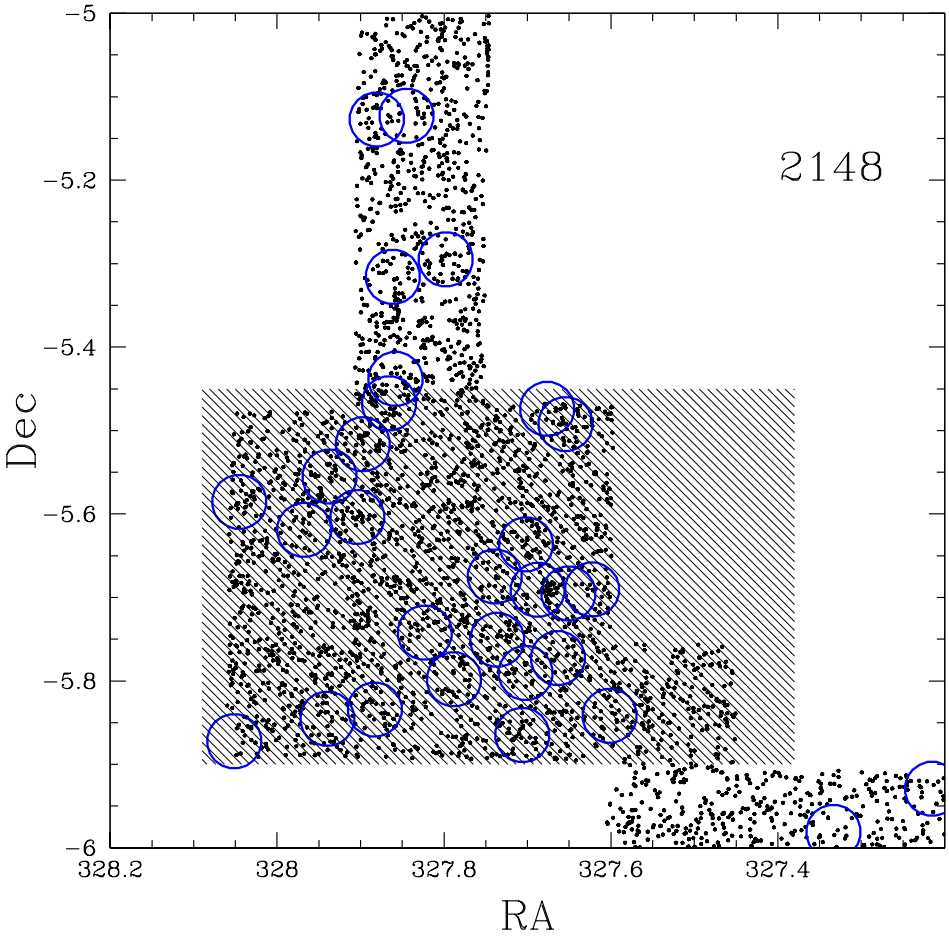

Figure 3.2: CNOC2 field 2148. The black dots are the positions of CNOC2 galaxies and circles represent the locations of CNOC2 galaxy groups (Carlberg et al., 2001). The hatched region is the field we observed using the cfh12k mosaic camera at CFHT. The region we observed covers the central portion of the CNOC2 field and we are able to observe many of the CNOC2 groups. The 3 other fields were very similar.

Field	Facility	Area (sq.arcmin)	Density (No./sq.arcmin)	Median Seeing	No. of Groups
0223+00	KPNO	1120	30	1.1	23
0920+37	CFHT	1100	40	0.9	40
1447+09	CFHT	1220	32	0.8	29
2148-05	CFHT	1125	40	0.8	25

Table 3.2: Field Information.

basic reduction step was to create a master flat frame and divide all science images by this flat field. The flat fields used in this analysis were all twilight flats. These steps can be seen in Figure 3.3. In addition to these standard reduction steps, the I-band images needed to have a fringe removal correction applied, and the R-band images from CFHT were corrupted by scattered light, which was removed. During the basic reductions the chips were trimmed to get rid of the overscan region and the bad pixels were flagged. The data reduction and stacking were carried out using the IRAF mosaic package, mscred (Valdes, 1997).

3.5 Astrometry and Stacking

Gravitational lensing is usually limited by systematics and it is important to ensure no spurious shear is introduced in the stacking procedure. This can be achieved by carefully monitoring the astrometry over each input image that enters the stack. Wide-field cameras in use today often have larger distortions

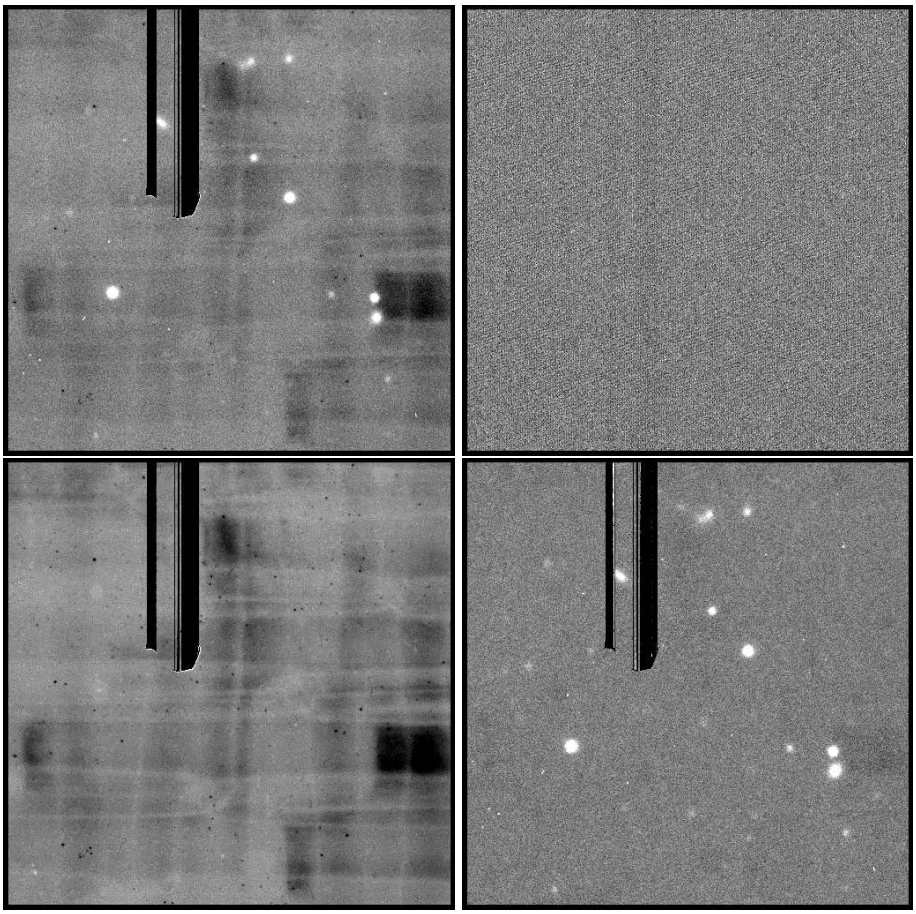

Figure 3.3: Basic image reduction. The raw frame is in the upper left, bias frame in the upper right, flat field frame in lower left and reduced image in the lower right. The bad pixels are masked in all of the analysis but can be clearly seen in this image.

than earlier, smaller CCD cameras. This distortion must be properly mapped and corrected in order to ensure no artificial source of shear is imported during the stacking process. Note, however, that group lensing is less affected by systematics than, for example, cosmic shear studies. Cosmic shear measurements use the patterns in the large-scale distortion field of background sources to map out the matter distribution in the universe. This signal is tiny and more susceptible to systematics than galaxy-galaxy or group-galaxy lensing where the shear signal is averaged in radial bins around each lens.

The goal is to have the best internal astrometry possible. The astrometric solution was calculated separately for each chip in the mosaic images to allow more freedom in the fit. The basic pipeline is outlined in Figure 3.4. The bright stars from the USNO-A2 star catalogue are identified in one image and then the positions of the stars are fit to match the known coordinates of the USNO-A2 stars. This fit is recorded in a "database" file which can then be applied to other images. This corrected image is then fed into a source detection package such as SExtractor (Bertin and Arnouts, 1996) and all objects in the image are found. This catalogue of positions now becomes the master catalogue, to which each other image is matched. In this way the internal, or relative, astrometry is very good (the rms is $\sim$0.05 arcseconds). The reason this pipeline was necessary is that the astrometric solutions from the telescope were not sufficient for lensing purposes.

The matched images are then stacked together to create one deep image which can be used to for source detection and shape measurements. The process of the matching can be see in Figure 3.5. The coordinates of the master catalogue are overlaid onto an image, once the matching to the catalogue is

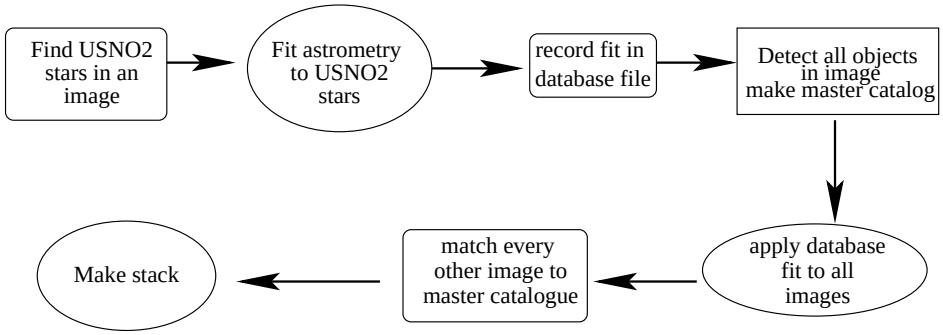

Figure 3.4: The astrometric pipeline. Raw images are reduced and then matched to a master catalogue produced from one of the individual frames. The corrected images are then combined to create deep stacks used for object detection and shape measurement.

done the positions of the catalogue objects and the image are aligned. It is important to note that since lensing relies critically on shape measurements only images of the highest quality are desired. Therefore, only the images with the best seeing are kept. Typically the best $\sim 60 - 70\%$ of the images are used in the stacks.

An alternative to stacking images and measuring galaxy shapes is measuring the shapes on individual frames and averaging these (Bernstein and Jarvis, 2002). Combining the shape measurements for each image separately allows you to weight the measurements based on image quality, for example, which is not possible when you measure objects from one final stack. This method works better than operating on a stacked image if you have an unstable PSF which would corrupt your stack, or if you have large dithers resulting in the same objects falling on different chips in different exposures. Unfortunately,

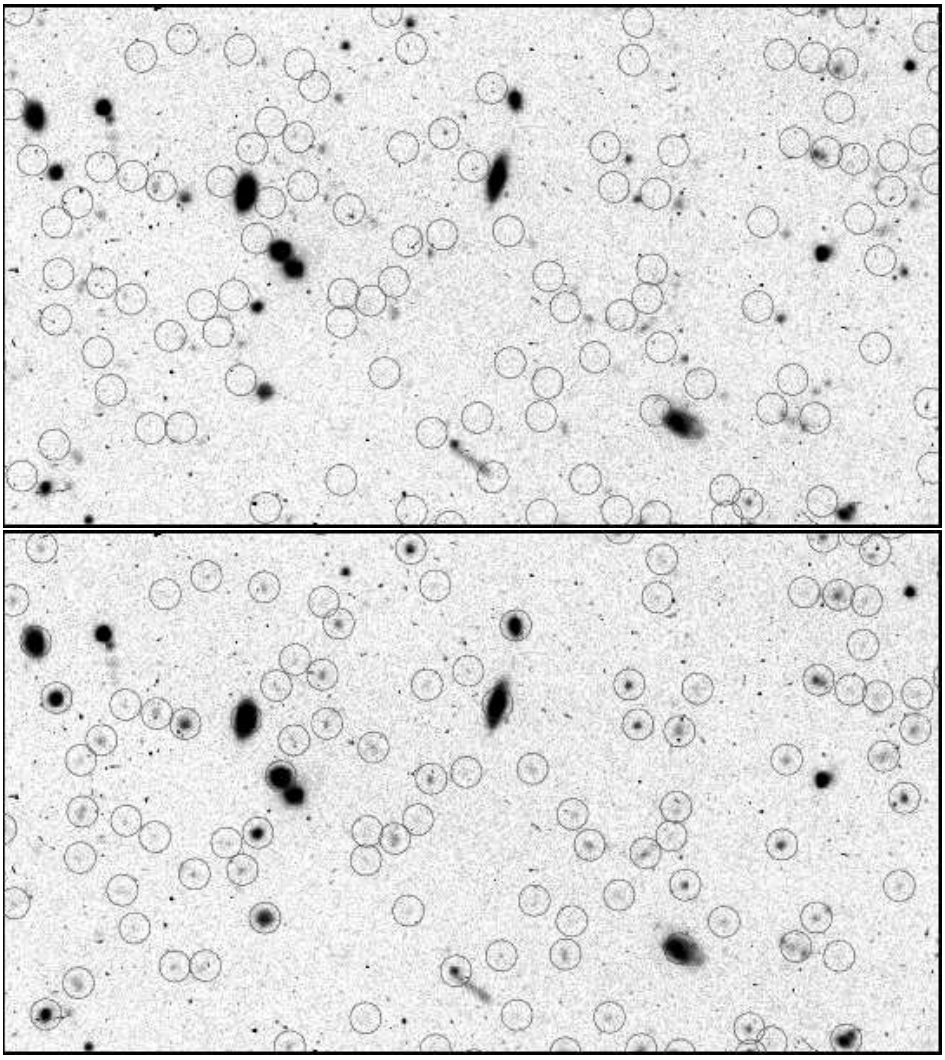

Figure 3.5: The upper panel shows one reduced image with catalogue coordinates overlaid. The lower panel demonstrates the same catalogue overlay after the astrometric fit has been applied. The astrometry is corrected in all images before the deep stacks are produced.

in order to measure the shapes of individual faint objects the positions of those objects must be precisely known, and therefore the objects are extracted from a deep stacked image, not the individual frames. This means that a careful stack must be made in order to detect the objects, and so the simplest analysis then uses this stack for shape measurements. If the data has a stable PSF and small dithers there is no advantage to stacking the shapes from each exposure separately. Measuring the shapes from each exposure is also computationally expensive and requires substantial data storage for any reasonably sized survey.

3.6 Object Detection and Shape Parameters

Object catalogues were extracted from our stacked images using the imcat software, an implementation of the Kaiser, Squires and Broadhurst (1995, hereafter KSB) method. This software is optimized for measuring the shapes of faint sources. The object detection algorithm works by smoothing the images using different sized filters and then detecting the "peaks" which are then added to the source catalogue. This hierarchical object finder gives the user flexibility in determining the significance of peaks to be added to the source catalogues. For this analysis only objects which were more than 5σ above the background were included.

Each detected object is assigned a Gaussian radius by the peak-finding software which is then used for aperture photometry. The photometry is used to calculate the apparent magnitude of each source as well as the half-light radius. The peak-finding and aperture photometry can be done within imcat or

alternatives such as SExtractor (Bertin and Arnouts, 1996) can be used. For each detected object, weighted quadrupole moments were measured and the resulting polarizations were calculated as in equations 2.18 and 2.19.

The polarization measurements need to be corrected for the effects of seeing, camera distortion and PSF anisotropy. These corrections have been discussed in KSB and Luppino & Kaiser (1997) with some improvements made by Hoekstra et al. (1998 and 2000). The shapes of objects are circularized by seeing as well as being altered by any anisotropy in the PSF. The PSF anisotropy correction is characterized by the smear polarizability in equation 2.20 and can be estimated by examining the shapes of stars. Smear polarizability defines how objects react to a convolution with a small anisotropic kernel. The shapes of stars pre- and post- correction can be seen in Figure 3.6. Without the correction the stars have a position angle of $\sim 60^{\circ}$. After correction the stars appear circular indicating that the correction scheme has worked.

The shapes of galaxies are used to estimate the shear, and therefore the "pre-seeing" shapes need to be determined. This can be done by applying the shear polarizability (equation 2.22). The shear polarizability accounts for the dilution of the shear due to the circularization caused by the seeing. This techniques work well for ground-based data where the PSF is stable and not very anisotropic, and where the fields contain many stars which are used in the correction algorithms.

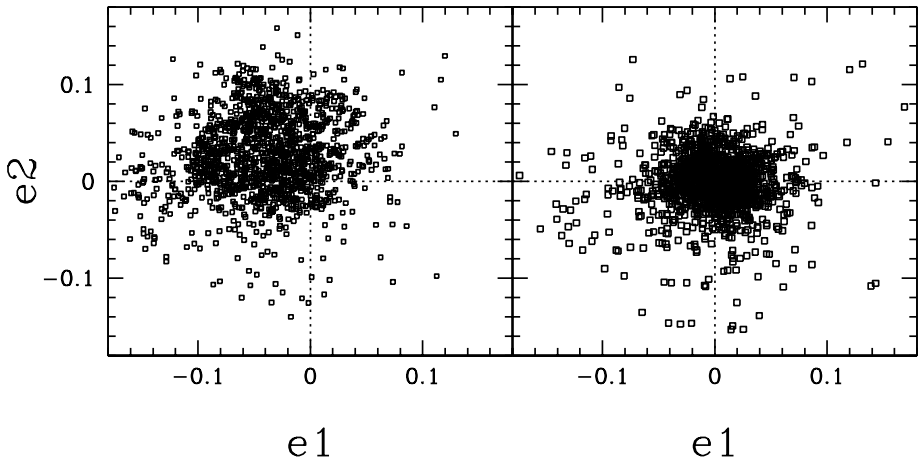

Figure 3.6: Pre- and post-correction polarization values for stars. The polarization values for stars should be small and average to zero, as can be seen in the post-correction data. Prior to correction the median e1 value is -0.040 and e2 is 0.025, giving a position angle of $\sim$60°. The stars are from one field used in the CNOC2 galaxy group analysis from Chapters 3 and 4.

3.6.1 Star-Galaxy Separation

The source catalogue generated from the imcat software contains stars, galaxies and unknown objects smaller than the stellar PSF. These catalogues can be cleaned to get rid of close neighbours and all objects smaller than the PSF for which no reliable shape measurements are available. Figure 3.7 shows a plot of apparent magnitude versus half-light radius which can be used to separate galaxies from stars. The stars can be easily located in this plot because they all have the same half-light radius, dictated by the PSF.

The source catalogues are trimmed so that all stars are removed. We kept only those objects for which the half-light radii were greater than 1.2 times the stellar PSF, thus ensuring the contamination from stars in our source catalogue is very small. Without applying a size cut we would expect roughly $\sim$10% of the objects at faint magnitudes to be stars (based on the slopes of stellar and galaxy number counts as a function of magnitude). Thus, while some small number of stars may scatter to sizes larger than 1.2 times the PSF, the stellar fraction in the final source catalogue will be $\ll$10%. The shapes of the galaxies are then weighted based on the errors in their shape measurements as described in Hoekstra et al. (2000). This is effectively down-weighting all of the small and faint galaxies for which the shapes are poorly defined.

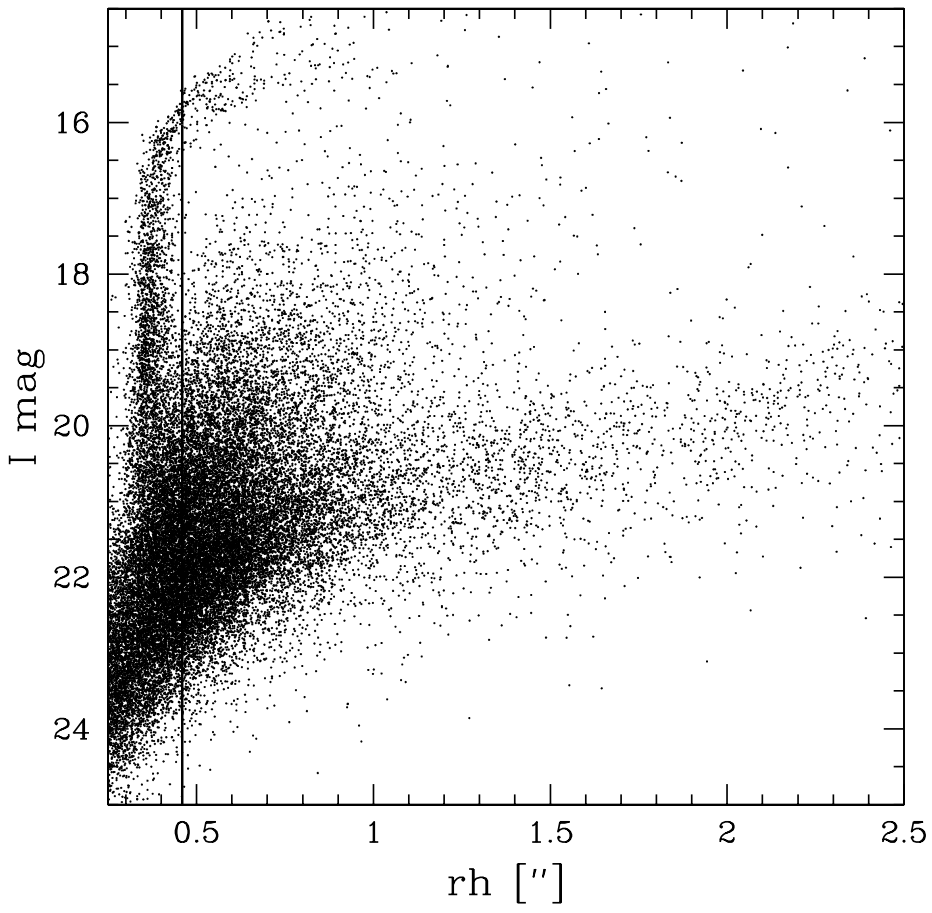

Figure 3.7: Apparent magnitude in the I_C-band versus the half-light radius in arcseconds for one of the CNOC2 fields. The stellar locus is clearly visible at r_h $\sim$0.38 arcseconds. Only objects with $r_h > 1.2$ times the stellar PSF (indicated by the vertical line) are included in source catalogue.

Chapter 4

CNOC2 Weak Lensing Analysis

When we try to pick out anything by itself, we find it is tied to everything else in the universe.

— John Muir

4.1 Weak Lensing Measurement

In the weak lensing analysis we used a source catalogue of approximately 150 000 objects ($\sim$40 per sq arcminute) and a galaxy group catalogue containing the 116 CNOC2 galaxy group centres that were within the area we observed. The faint members of the galaxy groups are included in the source catalogue, but the number density of faint galaxies is increased by only a few percent towards the group centre; thus the presence of faint group members do not influence the final shear measurement.

The weak lensing signal for individual galaxy groups is not sufficient to

extract a reliable measurement. The signal-to-noise of the lensing signal is proportional to the square of velocity dispersion (equation 4.1), thus the signal from a σ $\sim$200 km s^{-1} group is 25 times smaller than from a σ $\sim$1000 km s^{-1} cluster. Therefore, the signal from many galaxy groups must be stacked together. Assuming that the dark matter halos of groups are well described by an isothermal sphere, we expect a tangential shear signal as follows

$$\gamma_T = \frac{\theta_E}{2\theta} = \frac{2\pi\sigma^2}{c^2\theta}\frac{D_{LS}}{D_S} \tag{4.1}$$

where σ is the line-of-sight velocity dispersion of the halo, and D_S and D_{LS} are the angular diameter distances shown in Figure 2.1. The source galaxies around the stacked galaxy group were divided into radial bins and the average distortion was calculated in each bin.

The tangential shear calculated from the stacked groups is shown in Figure 4.1. The tangential shear is plotted in physical bins (units of h^{-1}Mpc) since the redshift of each galaxy group is precisely known from the CNOC2 redshift survey. The best fit isothermal sphere to the average tangential shear profile yielded an Einstein radius of $0\farcs88 \pm 0\farcs13$.

We can alternatively fit the tangential shear data with a Navarro, Frenk and White (NFW) dark matter profile (Navarro, Frenk & White, 1996). This density profile, which has been observed to fit mass distributions well over a wide range of scales, is given by

$$\rho(r) = \frac{\delta_c \rho_c}{(r/r_s)(1 + r/r_s)^2} \tag{4.2}$$

where ρ_c is the critical density for closure of the universe. The scale radius, r_s, is defined as r_{200}/c_{NFW} where c_{NFW} is the dimensionless concentration

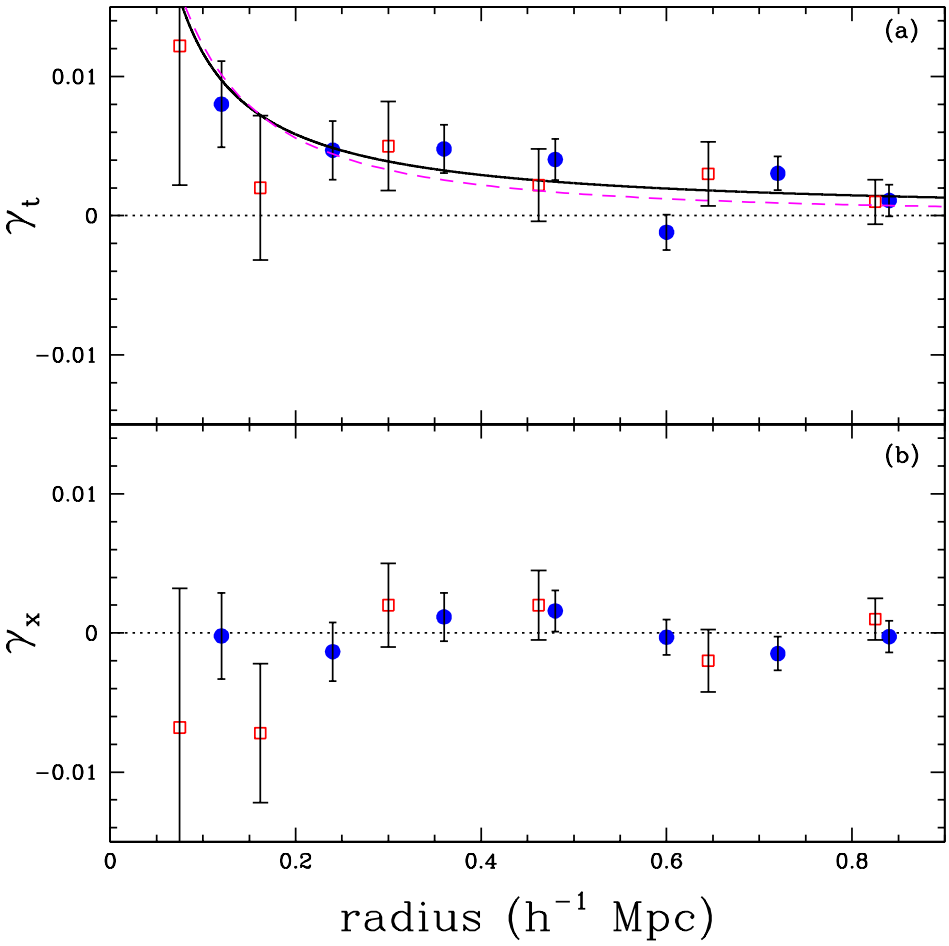

Figure 4.1: (a)The ensemble averaged tangential shear as a function of radius around a sample of CNOC2 galaxy group centres from Carlberg et al (2000).The best fit isothermal sphere, shown with the solid line, yields an Einstein radius of $0\farcs88 \pm 0\farcs13$ corresponding to a velocity dispersion of 245 ± 18 km s^{-1}. The best fit NFW profile is shown with the dashed curve. (b) The signal when the phase is rotated by $\pi/2$. No signal is present as expected if the signal in (a) is due to gravitational lensing. The results of Hoekstra et al. (2001) are shown with the open squares while the results of this analysis are shown with filled circles. There is good agreement between the two measurements but the result here is a much more significant detection.

parameter, and δ_c is the characteristic over-density of the halo. The tangential shear signal γ_T as a function of radius θ for a NFW halo is given by (Wright & Brainerd, 2000):

$$\gamma_T(\theta) = \begin{cases} \frac{r_s \delta_c \rho_c}{\Sigma_c} g_<(x) & , x < 1 \\ \frac{r_s \delta_c \rho_c}{\Sigma_c} \left[\frac{10}{3} + 4 \ln\left(\frac{1}{2}\right)\right] & , x = 1 \\ \frac{r_s \delta_c \rho_c}{\Sigma_c} g_>(x) & , x > 1 \end{cases}, \tag{4.3}$$

where $x = r/r_s$. The critical surface density Σ_c is given by

$$\Sigma_c = \frac{c^2}{4\pi G} \frac{D_S}{D_L D_{LS}}, \tag{4.4}$$

where D_L, D_S, and D_{LS} are the angular diameter distances between the observer and the lens, the observer and the source, and the lens and the source, respectively. The functions $g_<(x)$ and $g_>(x)$ in equation 2.3 are given in Wright $ Brainerd (2000) as

$$\begin{aligned} g_<(x) = & \frac{8 \mathrm{arctanh} \sqrt{\frac{1-x}{1+x}}}{x^2 \sqrt{1-x^2}} + \frac{4}{x^2} \ln\left(\frac{x}{2}\right) - \frac{2}{(x^2-1)} \\ & + \frac{4 \mathrm{arctanh} \sqrt{\frac{1-x}{1+x}}}{(x^2-1)\left(1-x^2\right)^{1/2}}, \end{aligned} \tag{4.5}$$

and

$$g_>(x) = \frac{8\arctan\sqrt{\frac{x-1}{1+x}}}{x^2\sqrt{x^2-1}} + \frac{4}{x^2}\ln\left(\frac{x}{2}\right) - \frac{2}{(x^2-1)} + \frac{4\arctan\sqrt{\frac{x-1}{1+x}}}{(x^2-1)^{3/2}}. \quad (4.6)$$

In order to fit this two-parameter profile to our tangential shear data we must assume a reasonable value for the concentration parameter c_{NFW}. Based on the high resolution numerical simulations of Bullock et al. (2001), a concentration parameter of $\sim$10 was used as a reasonable estimate for galaxy group scales. The best fit NFW profile can be seen as the dashed line in Figure 4.1. Over the scales where we can measure the weak lensing signal the NFW profile and the isothermal sphere are very similar and are both good fits to the data. The similarity of these two profiles at the galaxy group mass scale is expected from models (Wright and Brainerd, 2000).

A common systematic test employed in gravitational lensing is to measure the signal when the phase of the distortion is increased by $\pi/2$. If the measured tangential distortion is due to gravitational lensing the rotated signal should be consistent with 0 as is shown in Figure 4.1b. In addition to this standard systematic test, we also measured the signal around random points in the field. This test yielded no signal, indicating that the results plotted in Figure 4.1a are indeed due to gravitational lensing by the groups.

4.2 Velocity Dispersion

In order to relate our estimate of the Einstein radius to the average velocity dispersion of the groups, the redshift distribution of the background sources must be understood. The strength of the gravitational lensing signal as a function of redshift is characterized by the parameter β which is defined as

$$\beta = \max[0, \mathrm{D_{LS}}/\mathrm{D_S}]. \tag{4.7}$$

β was calculated for each group-source pair based on the known spectroscopic redshift of the group and the estimated redshift of the source. The source redshift estimate was based on the observed R_c magnitude and the method outlined in Brainerd, Blandford and Smail (1996). We find a value of β=0.49. This yields an ensemble averaged group velocity dispersion $<\sigma^2>^{1/2}$ =245$\pm$18 km s^{-1} for an $\Omega_m = 0.3$, $\Omega_\Lambda = 0.7$ universe. This value agrees well with Hoekstra et al. (2001) who found $<\sigma^2>^{1/2}$ =258$\pm$50 km s^{-1} for an $\Omega_m = 0.2$, $\Omega_\Lambda = 0.8$ universe, although our result has considerably smaller uncertainties. Our measured velocity dispersion from weak lensing also agrees with the results from a dynamical study of the CNOC2 groups (Carlberg et al., 2001) who found $\bar{\sigma}$ =218$\pm$14km s^{-1}. However, it is important to note that the value of σ from Carlberg et al., is dependent on a number of assumptions, most importantly the assumption that the groups are virialized.

4.3 Mass-to-Light Ratio

Gravitational lensing can be used to estimate masses, and hence mass-to-light ratios. The mass estimate , as a function of distance from the group centre, comes directly from the isothermal sphere fit to the tangential shear data, and the light information comes from the CNOC2 galaxy catalogues (Yee et al., 2000). Each galaxy in the redshift survey has a measured magnitude and various weights (colour, geometric and redshift) to account for incompleteness in the sample. The galaxy group luminosity profile was calculated by using the magnitudes and weights for each galaxy that belonged to a galaxy group. The group galaxies were sorted in radial bins centred on the group centres. The luminosity of each galaxy was calculated, with a correction for galaxies fainter than the survey limit. This was done by employing the CNOC2 galaxy luminosity function published in Lin et al. (1999) and using the spectral classification provided in the CNOC2 galaxy catalogues. The luminosities were not corrected for evolution, but were k-corrected. The mass-to-light ratio of the galaxy groups as a function of radius is plotted in Figure 4.2. We obtain an integrated mass-to-light ratio to 1.0 h^{-1}Mpc of $185 \pm 28h\mathrm{M}_{\odot}/\mathrm{L}_{B\odot}$, consistent with the value of $191 \pm 81h\mathrm{M}_{\odot}/\mathrm{L}_{B\odot}$ found by Hoekstra et al. (2001) using a subset of the groups. The method employed by Hoekstra et al. was slightly different in that the mass-to-light ratio was estimated by calculating the ratio between the measured shear signal and the expected shear derived from the luminosity profile. This method requires the assumption that the mass-to-light ratio is constant across the groups and was necessary because of the smaller data set and low signal-to-noise ratio. As is clear in Figure 4.2, the M/L ra-

tio is remarkably flat as a function of distance from the group centre. This is in contrast to what was found by the dynamical study of the CNOC2 groups, as will be discussed in Section 4.4. If the M/L ratio is calculated using the NFW mass profile the results are statistically equivalent. We chose to calculate the M/L ratio in the B-band to facilitate comparison to previous results, but it would also be interesting to calculate M/L ratio in a redder band which is less sensitive to recent star formation.

It is important to note that the tangential shear signal is sensitive to all matter along the line-of-sight, and as the distance from the group centre increases more of the signal is coming from other mass that is correlated with the group (like a 2-halo term in a cross-correlation function). In addition to calculating the M/L of the galaxy groups using the known group members from the CNOC2 groups catalogue, we also calculated the M/L for all galaxies in the CNOC2 galaxy catalogue with a line-of-sight separation $<$1200 km s^{-1}. This separation was chosen because galaxies within that distance, while perhaps not formally members of a virialized group could be correlated with the mass and therefore influence the lensing signal. The effect of this procedure is to add galaxies to our luminosity profile. The total M/L is lower by 8%, which is within the 1σ errors, and is still flat with distance from the group centre. Assuming a constant M/L with distance from the group centre, the best fit M/L using this larger sample of galaxies can be observed as the heavy dashed line in Figure 4.2.

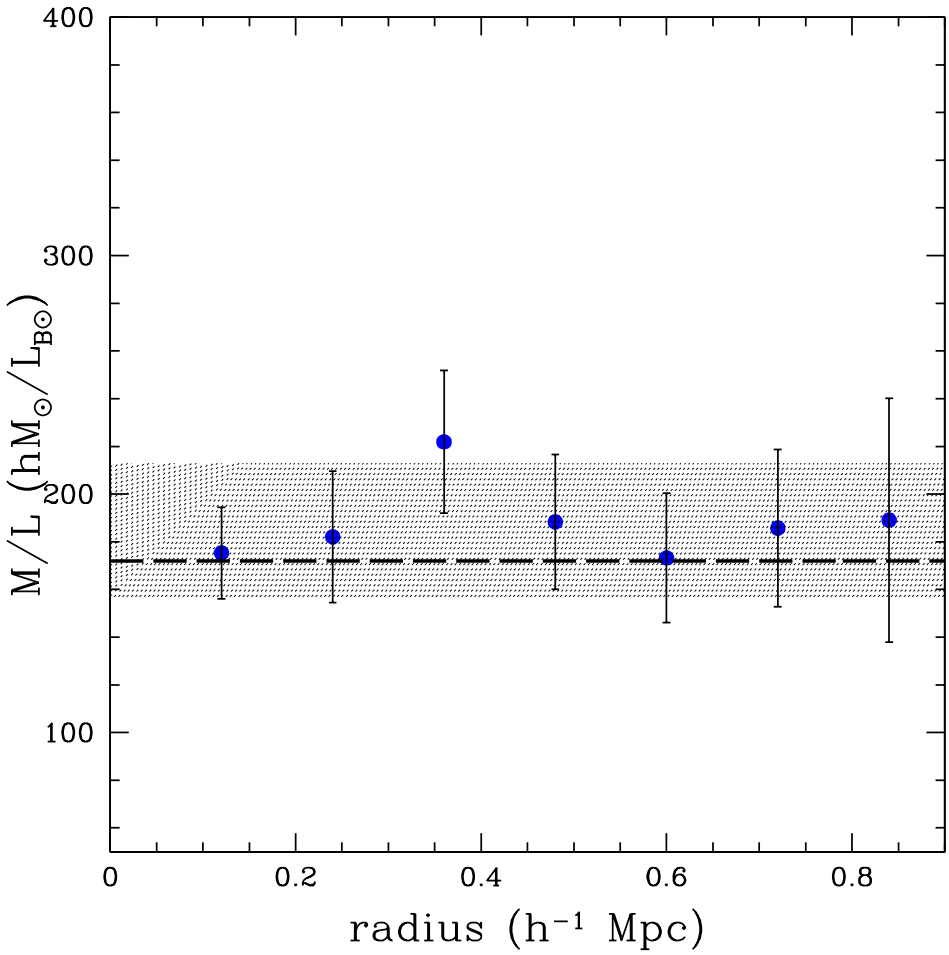

Figure 4.2: The mass-to-light ratio for the entire sample of galaxy groups in radial bins. The average M/L is 185±28 $h\mathrm{M}_\odot/\mathrm{L}_{B\odot}$. The hatched region represents the 1-σ bounds on the mass-to-light ratio, assuming M/L is constant with radius. The heavy dashed line indicates the M/L calculated using all CNOC2 galaxies projected to be close the galaxy group centre, as described in the text.

4.3.1 Mass-to-Light Ratios of Rich and Poor Galaxy Groups

We wanted to examine the difference in the shear signal from the rich and poor groups, and to this end we divided the galaxy group catalogue into two subsamples. We split the sample by the median dynamical velocity dispersion (190 km s^{-1}), although results were similar regardless of whether the groups were divided by their luminosities or velocity dispersions as we will discuss in Section 4.4.1. The same source catalogue was used to study the two group subsets. The only difference from the technique outlined in the sections above is that the input group catalogues have half the number of groups. The resulting tangential and cross shear for the two group subsets are shown in Figure 4.3.

The shear profiles for the two subsamples were fit with isothermal spheres and their mass-to-light ratios were estimated. The mean velocity dispersion of the "poor" groups is $<\sigma^2>^{1/2}$ =193$\pm$38 km s^{-1}, while the "rich" groups have a velocity dispersion of $<\sigma^2>^{1/2}$ =270$\pm$39 km s^{-1}. The mass-to-light ratios of the "rich" and "poor" galaxy groups are flat with radius, as can be seen in Figure 4.4. The weighted mean mass-to-light ratio of the "poor" groups within 1 h^{-1}Mpc is 134$\pm$26 $h\mathrm{M}_{\odot}/\mathrm{L}_{B\odot}$, while the mass-to-light ratio of the "rich" groups within 1 h^{-1}Mpc is 278$\pm$42 $h\mathrm{M}_{\odot}/\mathrm{L}_{B\odot}$. As was done with the entire group sample, galaxies within 1200 km s^{-1} were added to the sample and the M/L ratios were calculated. The best fit results are shown with the heavy dashed lines in Figure 4.4. Note that the relative M/L between the rich and poor groups is not altered by the inclusion of nearby potentially correlated galaxies. The offset in the M/L ratio between the rich and poor groups is robust.

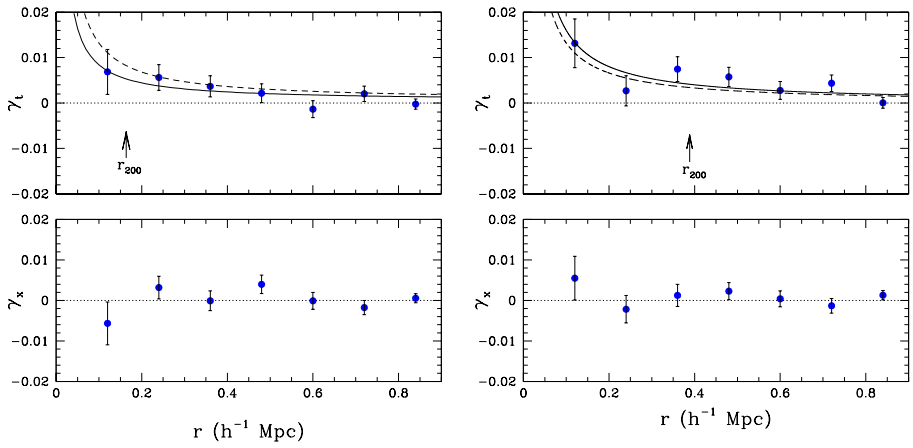

Figure 4.3: The tangential and cross components of shear as in Figure 4.1, on the left for the sample of "poor" groups, which have dynamical velocity dispersions less than 190 km s^{-1}, and on the right for the "rich" galaxy groups, which have velocity dispersions greater than 190 km s^{-1}. The best fit isothermal sphere is plotted with a solid line in both plots. The best fit velocity dispersion is 193 ± 38 km s^{-1} for the poor groups and 270 ± 39km s^{-1} for the rich groups. The dashed line is the best fit isothermal sphere from Figure 4.1, for the entire data set. The characteristic r_{200} values (Carlberg et al., 2001) are indicated by the arrows.

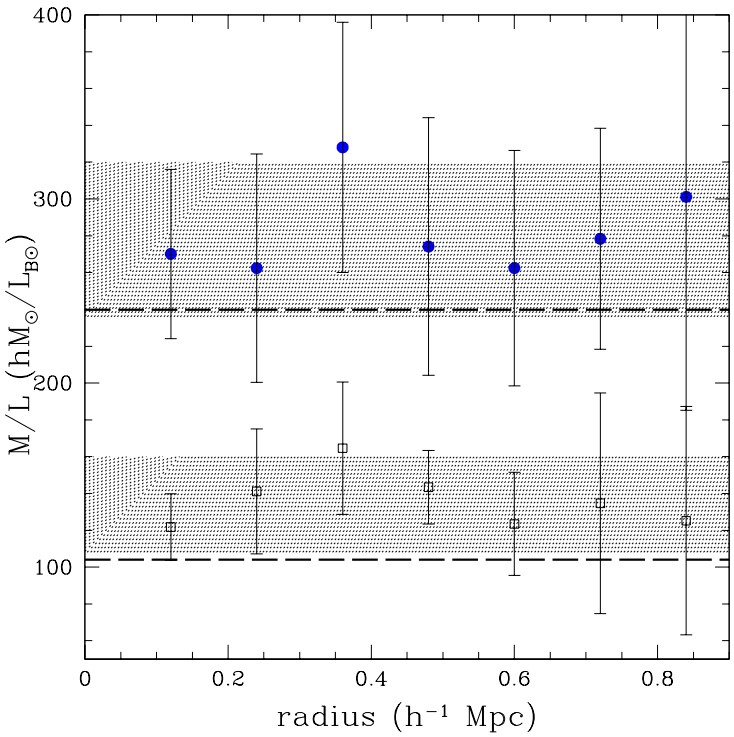

Figure 4.4: The mass-to-light ratio for subsamples of galaxy groups in radial bins. Symbols are as in Figure 4.2. The mass-to-light ratio of the poor galaxy groups (open squares) and rich galaxy groups (filled circles) as a function of the distance from the group centre. The average M/L of the rich groups is 278±42 $h\mathrm{M}_\odot/\mathrm{L}_{B\odot}$and 134±26 $h\mathrm{M}_\odot/\mathrm{L}_{B\odot}$ for the poor groups. There is a clear offset in the mass-to-light ratio between the two subsamples as can be seen by comparing the two hatched regions. The heavy dashed lines indicate the M/L calculated using all CNOC2 galaxies close to the group centre, as described in the text.

4.4 Discussion

Weak lensing is a powerful tool for understanding the ensemble-averaged properties for a sample of objects, but can not tell us about the properties of an individual galaxy group. There are a few potential systematic effects which could influence the shear results. We will discuss some of those in this section along with a comparison to other galaxy group results.

4.4.1 Systematic Tests

Testing the centres

The tangential lensing signal is measured in annular bins around the group centres. If the centres are poorly defined, or not properly assigned, then the resulting shear signal will be smaller than the if the true centre had been used. The Carlberg et al. (2001) CNOC2 group centres were defined based on the average galaxy position. An alternative choice of groups centres is the brightest galaxy. Most galaxy clusters have their brightest galaxy at the centre of their potential well (Postman and Lauer, 1995). In order to test whether the brightest group galaxy is a good tracer of the galaxy group centre, we repeated the shear analysis outlined above replacing the group centres with the position of the brightest group member. The results are shown in Figure 4.5. There is a positive detection of a tangential shear signal, but it is $\sim$25% lower than in the case of position weighted centres. This indicates that an isothermal sphere centred on the brightest group member is not the best fit to the potential of these galaxy groups. From Figure 4.5 it appears that the first bin is higher for

the case of the brightest galaxy centres. This could be due to the galaxy-galaxy lensing signal from that bright galaxy. In addition, it appears that on the largest scales the tangential shear signal for the two centre definitions are very similar. This is expected since at very large radii the result of changing the centre should be minimal.

In addition to measuring the tangential shear signal around the brightest group galaxy, we also measured the signal around the Carlberg et al., centres randomized by up to 40″ (0.12 h^{-1}Mpc). The resulting isothermal sphere fits differed by $\lesssim$10%, indicating that the group centre positions need only be accurate to that level. The single isothermal sphere fit, and hence the derived velocity dispersion, are dominated by the outer bins where the errors are much smaller.

The most massive groups

As we have seen the lensing signal is proportional to the square of the velocity dispersion. The results in figure 4.3 clearly indicate that the lensing signal is dominated by the larger groups. A few of the galaxy groups identified in the CNOC2 fields had measured velocity dispersions in excess of 500 km s^{-1}. To be certain that the tangential shear signal measured was not coming solely from these groups we measured the tangential shear around only those groups with dynamical velocity dispersions greater than 500 km s^{-1}. In addition, we also repeated the measurement of the tangential shear around all galaxies except those with velocity dispersions greater than 500 km s^{-1}. The results, as shown in Figure 4.6 indicated that there is a substantial signal coming from the most

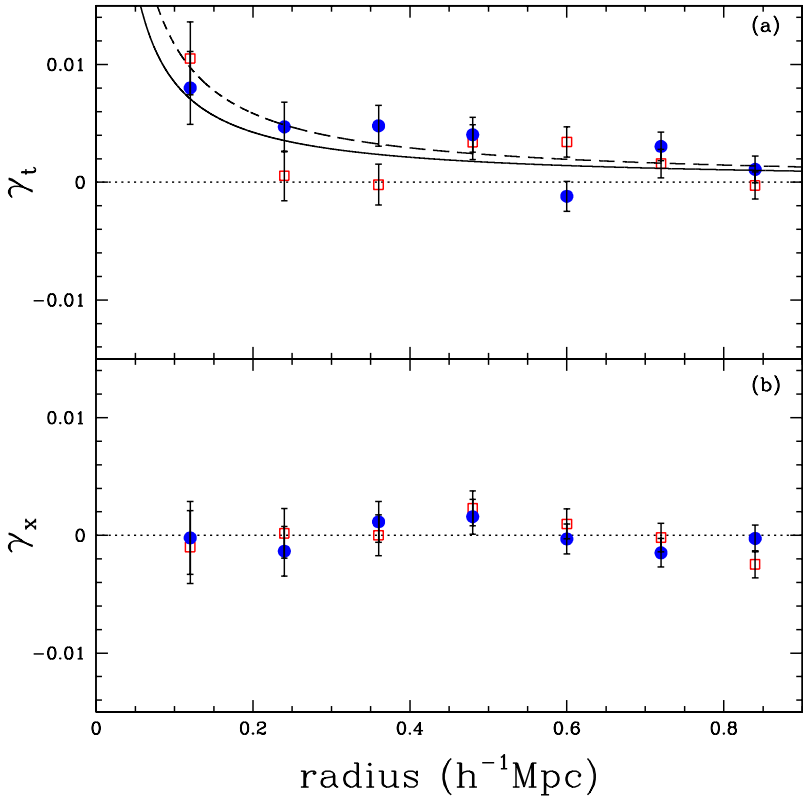

Figure 4.5: (a) The ensemble averaged tangential shear as a function of radius. (b) The shear signal when the source images are rotated by 45°. The open squares are the measurements assuming the brightest group member galaxy is the centre of the galaxy group. The filled circles are as in Figure 4.1, based on the centres of Carlberg et al. (2001). The best fit isothermal to the data, assuming the brightest galaxy is the centre, is shown with the solid line. The dashed line is the best fit from Figure 4.1. The tangential shear signal is clearly weaker for galaxy position weighted centres. The best fit isothermal sphere corresponds to a velocity dispersion of 169 ± 28 km s^{-1}.

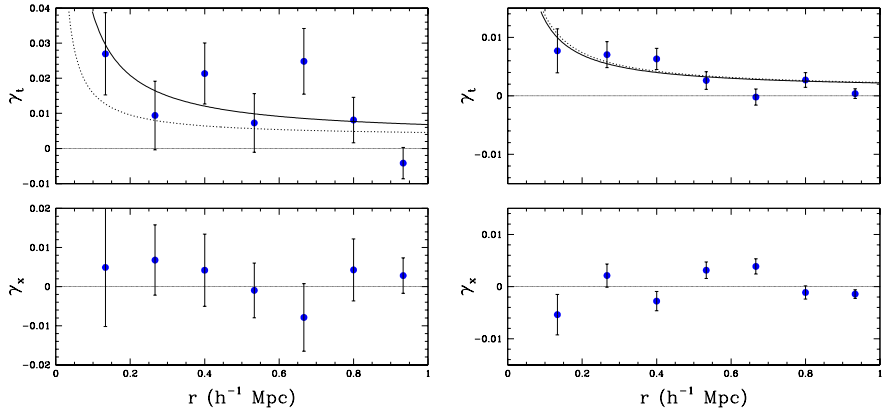

Figure 4.6: On the left, the tangential shear measured from a sample of galaxy groups with dynamically inferred velocity dispersions of greater than 500 km/s. The best fit isothermal sphere yields a lensing derived velocity dispersion of 425 ± 182 km s^{-1}. On the right, the remaining shear signal when the massive galaxy groups are removed. The best fit isothermal sphere gives a velocity dispersion of 239 ± 37 km s^{-1}. The dotted line in both plots is the best fit isothermal sphere from Figure 4.1, for the entire data set.

massive galaxy groups (small clusters) but that the tangential shear profile is not dominated by these for the sample as a whole. The lensing-derived velocity dispersion for the most massive groups is 425 ± 182 km s^{-1}. After the massive groups are removed an isothermal tangential shear profile with an Einstein radius of roughly $0.8''$ remains, corresponding to an ensemble-average velocity dispersion of 239 ± 37 km s^{-1}.

Dividing the Sample

The subsamples of rich and poor galaxy groups were selected based on their dynamically estimated velocity dispersions. However, since these groups have, on average, 4 members, this dispersion estimate is very noisy, with errors of typically 50% per group. An alternative way to divide the groups into rich and poor subsamples is based on their observed luminosities. The rich galaxy groups are those with a luminosity greater than the median group luminosity, $6.86\times10^{10}L_{\odot}$, and the poor groups are those with a luminosity less than the median. The weak lensing signal can then be measured for these two subsamples. The resulting velocity dispersions are 298 ± 43 km s^{-1} and 192 ± 38 km s^{-1} for the rich and poor groups respectively. The results are within 1-σ of the velocity dispersion defined rich and poor groups. However, the contrast is higher between the rich and poor groups with the luminosity defined subsamples, suggesting that perhaps the noisy velocity dispersions are diluting the differences between the two subsamples. It appears that for this sample, either the velocity dispersion or the luminosity can be used to divide the sample of galaxy groups into subsamples, but since the luminosity of the groups is less noisy than the dynamical velocity dispersion it may ultimately be a better separation criterion when there are not many group members identified.

4.4.2 Comparison to Other Work

It is of great interest to compare the results we obtained for our sample of CNOC2 galaxy groups to those obtained by Carlberg et al. (2001), using dynamical methods on the full sample of CNOC2 galaxy groups. The lensing-

and dynamically-derived properties of these CNOC2 groups are summarized in Table 4.1. The lensing and dynamical results agree well for the sample as a whole, and for the rich groups, but there appears to be some difference in the mean velocity dispersion of the poor groups. Of course it is for this latter sample that the dynamical estimates will be most strongly affected by systematic errors, so we do not wish to draw any strong conclusions from the slight discrepancy.

We found that the M/L ratio was extremely flat with distance from the group centres as can be seen in Figure 4.2. This is in contrast to what was found using the dynamics of the CNOC2 groups. In order to properly compare our results to those of Carlberg et al. (2001), we have calculated the shear and light profiles in units of r_{200}. In Figure 4.7 we have plotted the lensing M/L ratio of galaxy groups as a function of radius, as well as the best fit curve for the dynamical data in units of r_{200}. We do not observe the steep increase in M/L that was observed with the dynamical methods. Our data can be well-fit with a straight line with no slope. The M/L ratio calculated from the dynamical data is dependent on the orbits of the galaxies in the groups, but their result of a rising M/L is robust for all reasonable orbits. It is not clear why there is such a contrast in the radial M/L ratio profiles between dynamics and lensing. The dynamical methods can be tested by repeating the friends-of-friends algorithm and velocity dispersion estimates on data from a numerical simulation.

It is particularly interesting to plot our two values for the mass-to-light ratio of galaxy groups on the mass sequence, and compare our results to previous measurements. This can be seen in Figure 4.8 where B-band M/L ratios for galaxy groups and clusters are plotted. The curve is from Marinoni & Hudson

Group Sample	$\bar{N}$ per group	$<\sigma>_{\rm lens}$ km s^{-1}	$<\sigma>_{\rm dyn}$ km s^{-1}	$<$M/L$>_B$ hM$_\odot$/L$_\odot$	$<$M/L$>_{R_C}$ hM$_\odot$/L$_\odot$	median z
all	3.9	245$\pm$18	219$\pm$10	185$\pm$28	179$\pm$27	0.323
rich	4.2	270$\pm$38	311$\pm$13	278$\pm$42	269$\pm$40	0.360
poor	3.6	198$\pm$38	127$\pm$4	134$\pm$26	130$\pm$26	0.303

Table 4.1: Weak lensing and dynamical properties of galaxy groups

(2002), who estimated the M/L ratio by comparing the mass function from Press-Schechter model with their measured luminosity function of virialized systems. Our data follow the trend of rising mass-to-light ratio with mass. We are in approximate agreement with the global mass-to-light ratio found on similar scales by Carlberg et al. (2001), Tucker et al. (2000) and Eke et al. (2004), although some of these studies are at a lower redshift.

The halo mass of approximately 10^{13}M$_\odot$, hosting typically 3 L* galaxies (Marinoni and Hudson, 2002), appears to be a critical scale, at which the mass-to-light ratio is increasing dramatically as a function of mass. There are a couple of possible explanations for this rise. Firstly, the higher mass halos could host a much larger fraction of early type galaxies than the low mass groups, and therefore the M/L ratio measured in the B-band would rise with mass. Recent results by Weinmann et al. (2005) indicate that we should expect an increase in the early type fraction of $\sim$10% (and a decline in late types of 10%) between our poor and rich galaxy group samples. This can not explain the large offset in M/L ratios. An alternative explanation is that there is a fundamental difference in the efficiency of star formation between the high

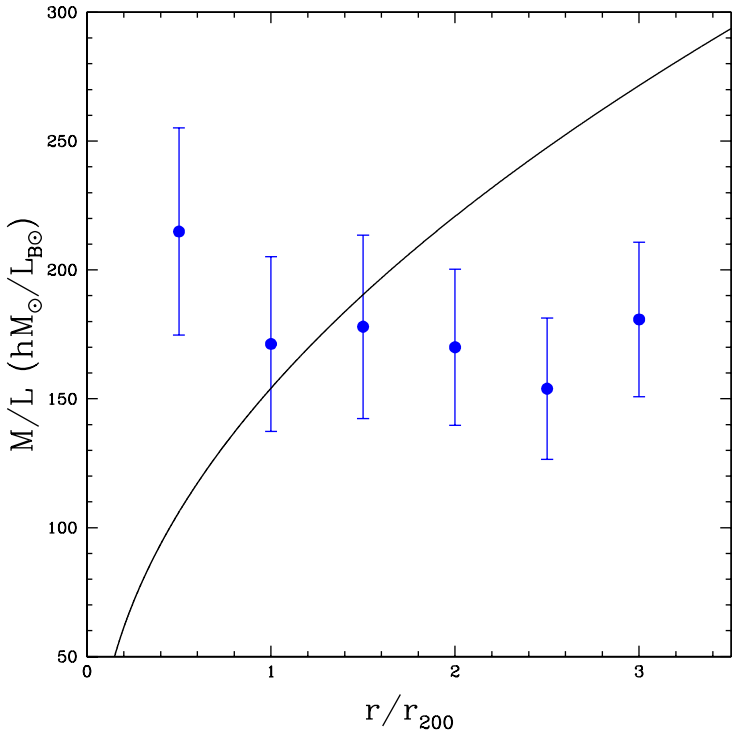

Figure 4.7: The mass-to-light ratio of the galaxy groups in radial bins in units of r_{200}. The line is fit to the dynamical results of Carlberg et al. (2001). We do not observe the steep rise in mass-to-light ratio with radius. Note that the Carlberg et al. results are for a 3-dimensional mass-to-light ratio while the data points are in projection.

and low mass group halos. This could indicate the transition from the actively star-forming field environment to the passively-evolving cluster regime. This theory is supported by recent results of Eke et al. (2005) showing that the K-band M/L ratio also increases steadily with mass scale. They determined that the stellar-to-total mass fraction declines with halo mass, indicating that there is a fundamental difference in the star formation efficiencies on different mass scales.

Note that the M/L ratio of the rich galaxy groups appears to be comparable to that found in massive galaxy clusters (Carlberg et al., 1997), as seen in Figure 4.8, so there is presumably little change in M/L on more massive scales. A rise in M/L on group scales has been suggested previously, from analysis based directly on dynamical studies of groups (Marinoni and Hudson, 2002; van den Bosch et al., 2003; Eke et al., 2004) and from semi-analytic models (for example Benson et al. (1992)). See also the discussion in Dekel & Birnboim (2004). The results presented here are then consistent with earlier studies, although this weak lensing result suggests a somewhat steeper increase than had been found previously.

4.4.3 Estimating Ω_m

From the average mass-to-light ratio for our entire sample of galaxy groups it is possible to naively estimate Ω_m using the method outlined in Carlberg et al. (1997). By combining M/L with luminosity density it is possible to estimate the matter density of the universe.

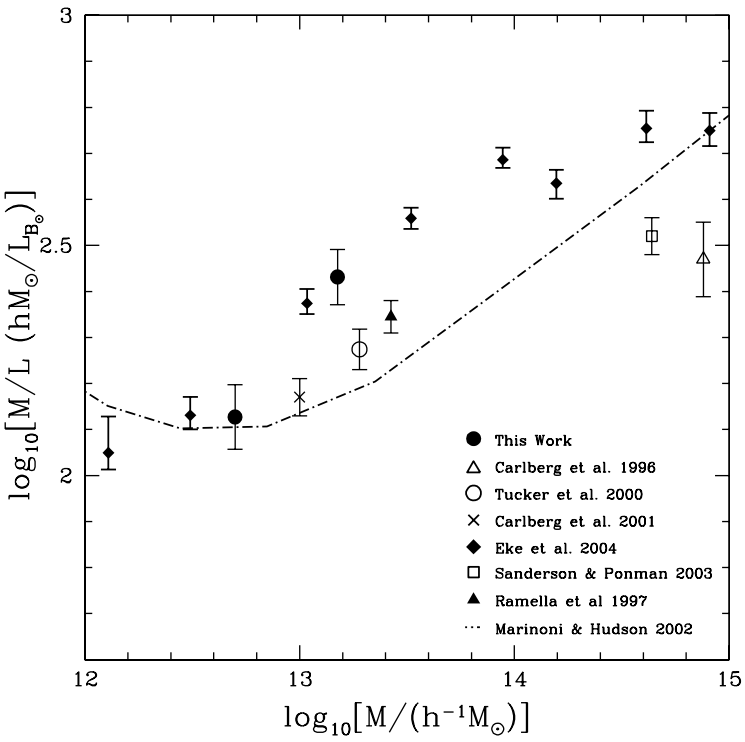

Figure 4.8: The mass-to-light ratio as a function of mass for samples of groups and clusters from the literature. The curve (Marinoni and Hudson, 2002) is generated by comparing the mass function from Press-Schechter theory for a ΛCDM universe with an observed luminosity function. Note that the different samples span a range of redshifts. For example, our median redshift is 0.33 while the 2PIGG data (Eke et al., 2004) median redshift is roughly 0.1.

$$\Omega_m = \frac{\rho_m}{\rho_c} = \frac{\rho_L}{\rho_c}\frac{M}{L} \tag{4.8}$$

Using a mass-to-light ratio of $185 \pm 28\ h\mathrm{M}_\odot/\mathrm{L}_{B\odot}$ (converted to $h\mathrm{M}_\odot/\mathrm{L}_{R_{AB}\odot}$), and the luminosity density for CNOC2 galaxies found in Lin et al. (1999) we obtain Ω_m=0.22$\pm$0.06. This is a valid estimate of Ω_m only if galaxy groups dominate the mass and luminosity of the universe. In order to properly calculate Ω_m, it is necessary to know the mass-to-light function for a wide range of masses, extending to single galaxies and rich clusters.

4.4.4 Where is the Group Mass?

The analysis described in this chapter assumes that the mass in a galaxy group can be well described by a simple density profile such as the isothermal sphere or the NFW profile. If, however, the mass in galaxy groups is clumped around the group galaxies, rather than the group centre, then this is not a good assumption. Möller et al. (2002) simulated the expected tangential shear signal from galaxy groups with various mass models. If the mass is mostly concentrated around the group galaxies then the shear signal is suppressed in the inner-regions because there is a deficiency of group mass. This can be seen in Figure 4.9 from Möller et al.(2002). Models with 100% of the mass in the group halo are well fit by an isothermal sphere, whereas models with no mass in a universal group halo deviate strongly from an isothermal sphere at small radii. As can be seen in Figure 4.9 it is possible to discriminate between models only at very small radii. This is not possible with our data, but it is a possible test for the future. Space-based data would be particularly useful for

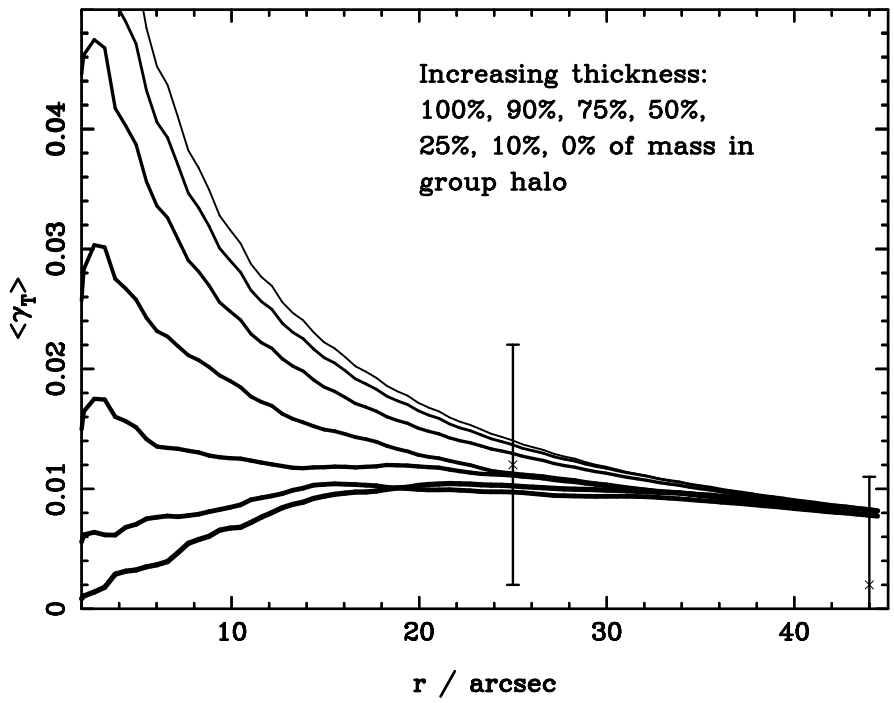

Figure 4.9: Simulated tangential shear for a sample of 100 galaxy groups with different group mass models from Möller et al.(2002). The total group mass is the same in all cases. The data points are from Hoekstra et al. (2001).

this project if a large enough sample of galaxy groups could be observed. The higher source density of objects detected from space would help the statistics in the small radius-bins where there is very little area. It is only possible to discriminate between models if the centres are well-defined. If the centres are off by many arcseconds, then this would also suppress the tangential shear profile in the inner regions.

4.5 Conclusions

We have detected a significant weak lensing signal for a sample of 116 intermediate redshift galaxy groups. From the lensing signal we estimate that galaxy groups have a mean M/L of $185 \pm 28\ h\mathrm{M}_{\odot}/\mathrm{L}_{B\odot}$ within $1\ h^{-1}$Mpc, and that this M/L ratio is constant as the distance from the group centre increases. When the sample is split into subsets of rich and poor galaxy groups, there is a clear offset in the mass-to-light ratios between the two subsets. The increase in the M/L as a function of mass is in general agreement with other results, but is detected here for the first time using weak lensing in the galaxy group mass regime.

This analysis indicates that a weak lensing signal can indeed be measured from galaxy groups. Clearly, a larger sample with well-determined dynamical properties would be ideal for this sort of study. The dark matter halo profiles of galaxy groups are still poorly understood. By combining this group lensing result with galaxy-galaxy lensing it should be possible to determine the size and extent of galaxy group dark matter halos, which will aid significantly in our understanding of structure in the universe and the nature of dark matter.

Chapter 5

Galaxy Dark Matter Halos

We know very little, and yet it is astonishing that we know so much, and still more astonishing that so little knowledge can give us so much power.

— Bertrand Russell

5.1 Introduction

Weak gravitational lensing of distant galaxies by foreground galaxies (galaxy-galaxy lensing) provides a unique tool to probe the dark matter structure of galaxy dark matter halos. Other techniques to map out the mass distribution of galaxies, including rotation curves and dynamical methods, require visible tracers and are thus capable of probing only the inner regions of galaxy halos. Gravitational lensing, on the other hand, is able to map out the mass distribution on much larger scales, far beyond the virial radius of galaxies, well beyond

where the visible part of the galaxy fades from view. Weak lensing on galaxy scales can be used to estimate the mass-to-light ratio of galaxies, as well as determine their dark matter profiles. These measurements can tell us something about the star formation history of different classes of galaxies, as well as provide information about the nature of dark matter.

A foreground galaxy acts to distort the shapes of background galaxies in much the same way that galaxy groups do, as described in the previous chapter. Source galaxies will be, on average, tangentially aligned with the foreground galaxy halos, and this alignment can be measured statistically. This technique has now been implemented successfully many times in the study of galaxy dark matter halos (Brainerd et al., 1996; Fischer et al., 2000; Hudson et al., 1998; Sheldon et al., 2004; Hoekstra et al., 2004). The weak lensing signal from an individual galaxy dark matter halo is too small to be detected and therefore many galaxies must be stacked in order to extract a signal. In this way galaxy-galaxy lensing is used to study ensemble-averaged properties for a population of galaxies.

The use of galaxy-galaxy lensing has grown dramatically in the past few years because of improvements in the analysis techniques employed, thus driving down systematic errors, and also because of modern large field surveys. Galaxy-galaxy lensing measurements require deep, wide-field images with very good image quality. The most precise lensing measurements to date come from the SDSS (Sheldon et al., 2004) which is not particularly deep, but covers an enormous area. Many of the world-class facilities (CTIO, CFHT, Subaru) have installed wide-field cameras which are ideal for this type of study. In addition, some facilities have implemented large survey programs which guarantee high

quality data over a large-field of view, optimized for weak lensing analysis (such as the Canada-France-Hawaii Telescope Legacy Survey).

5.2 CFHTLS

Canada and France have united to use a large fraction of their telescope time at the Canada-France-Hawaii-Telescope in order to complete a 5-year survey. The survey makes use of the new MegaCam instrument at CFHT. This camera is comprised of 36 separate CCD chips and produces distortion corrected 1 sq. degree images with superb image quality. The survey is divided into deep, wide and very wide components. The deepest survey data will cover 4 square degrees and will be used to search for Type Ia supernovae in order to better determine the value of the cosmological constant and the dark energy equation of state. The wide component is primarily designed for weak lensing studies. This will allow the study of dark matter halos, as we will discuss, but will also be used to study the lensing by large scale structure in the universe, cosmic shear. Cosmic shear studies complement the supernovae analysis since they can both be used to determine cosmological parameters. The third, shallow, component of the survey will be used to find and track Kuiper Belt objects in the hopes of better understanding the origin and evolution of solar systems.

This galaxy-galaxy lensing project makes use of early data from the CFHTLS wide survey. Eventually the wide data will cover $\sim$170 sq. degrees in 5 filters (u^*,$g'$$r'$,$i'$,$z'$). The observations are divided into 3 large patches which are well-separated in right ascension. Each patch is roughly 50 sq. degrees and

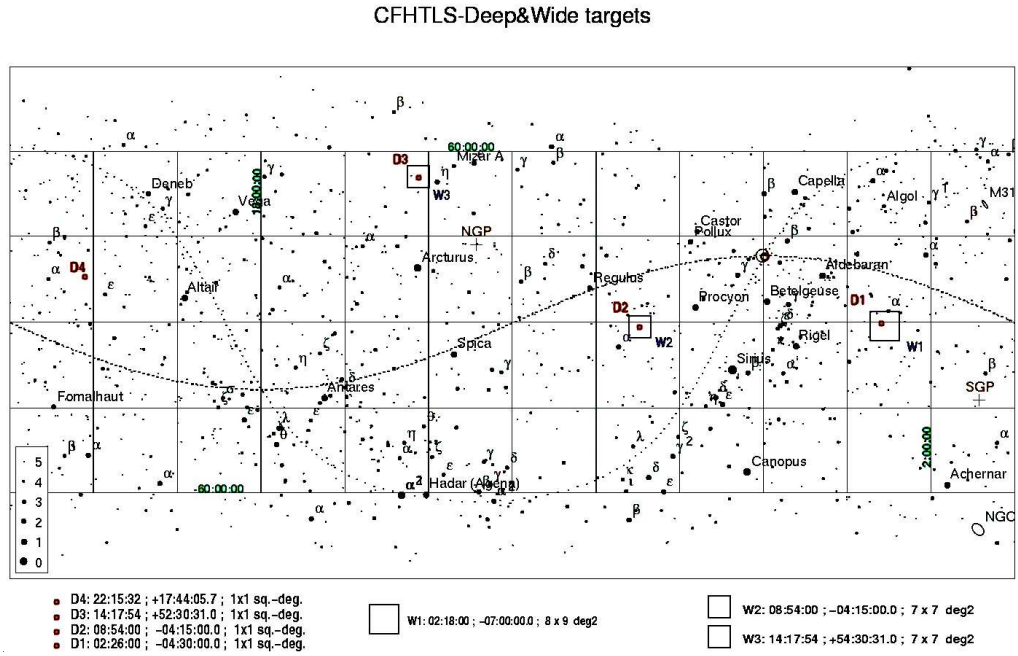

Figure 5.1: Location on the Sky of CFHTLS Deep and Wide fields.

is located far from the Galactic plane in order to minimize extinction and contamination from bright stars. The locations of the deep and wide survey fields can be seen in Figure 5.1. The wide fields all contain a deep field within in them which can be used for improved photometric redshift calibration, since the deep fields overlap with spectroscopic redshift surveys.

5.3 Data

The CFHTLS is an ongoing project that will continue collecting data for at least 2 more years. The analysis to be presented in this chapter is based on

early data collected in 2 of the 3 wide fields. The data consist of 31 pointings taken in the i′-band and cover an effective area of roughly 22 square degrees. The data are from the W1 and W3 fields which will total 72 and 49 sq. degrees respectively at the end of the survey. Figure 5.2 shows the coverage of the data used in this study. There are large masked areas where there were bright stars, diffraction spikes or bad pixels. The source density is $\sim$20 per sq. arcminute.

This represents $<$20% of the total wide area which will be covered at the end of the survey. In addition, the current data are in one band only. The median seeing for the images used in this project is $0.76''$. More recent CFHTLS observations have improved image quality. The image quality degrades towards the edge of the images but only data with sub-arcsecond seeing are included in this analysis. At the end of the survey there will be full 5-band data for the entire area, thus allowing the calculation of accurate photometric redshifts, as well as the discrimination of galaxies based on their observed colours. Ultimately the galaxy-galaxy lensing analysis will be done for subsets of the lenses based upon their observed properties such as their colours, morphologies or redshifts.

This early analysis is limited by the lack of redshift information for either the lenses or the sources. Knowing the redshifts of the lenses improves the signal-to-noise and allows the shear to be measured in physical bins. Redshifts can also be used to study the evolution of dark matter halos with redshift. However, from this early data set we will still have remarkable signal-to-noise and we will be able to not only determine the average mass of these halos, but also to try and measure the non-sphericity of the halos.

There have been previous galaxy-galaxy lensing measurements from large

area surveys (Hoekstra et al., 2004; Sheldon et al., 2004) but the CFHTLS is deeper and with the photometric redshifts we will be able to slice the lens samples into different redshifts and look for evolution in the dark matter halos of galaxies.

The CFHTLS images are provided to the Canadian and French astronomy communities after basic reductions (de-biasing and flat-fielding) by the Canadian Astronomical Data Centre. The images also have basic photometric and astrometric calibrations provided, though the astrometry is generally not precise enough for lensing purposes. The astrometric solution is corrected in a pipeline like the one outlined in Chapter 3. Each image is matched to a catalogue of sources more dense than the USNO-A2 catalogue. The astrometric corrections are also applied chip by chip for the best results. The corrected images are then stacked together to create the deep images used in source extraction for weak lensing shape measurements.

The CFHTLS data are slightly more complicated than the CNOC2 data described in the previous chapters because there are large dithers between some of the images. Therefore, some objects may appear on different chips in the individual exposures. This can lead to complicated PSF anisotropies, which are difficult to correct. For this early analysis all such “multi-chip” data are excluded. Each chip is stacked separately with data only from that chip. This comes at a cost of losing approximately 20% of the area but ensures accurate PSF anisotropy corection. Eventually it is hoped that the astrometry can be applied to the mosaic as whole and that the complicated PSFs can be understood and corrected for.

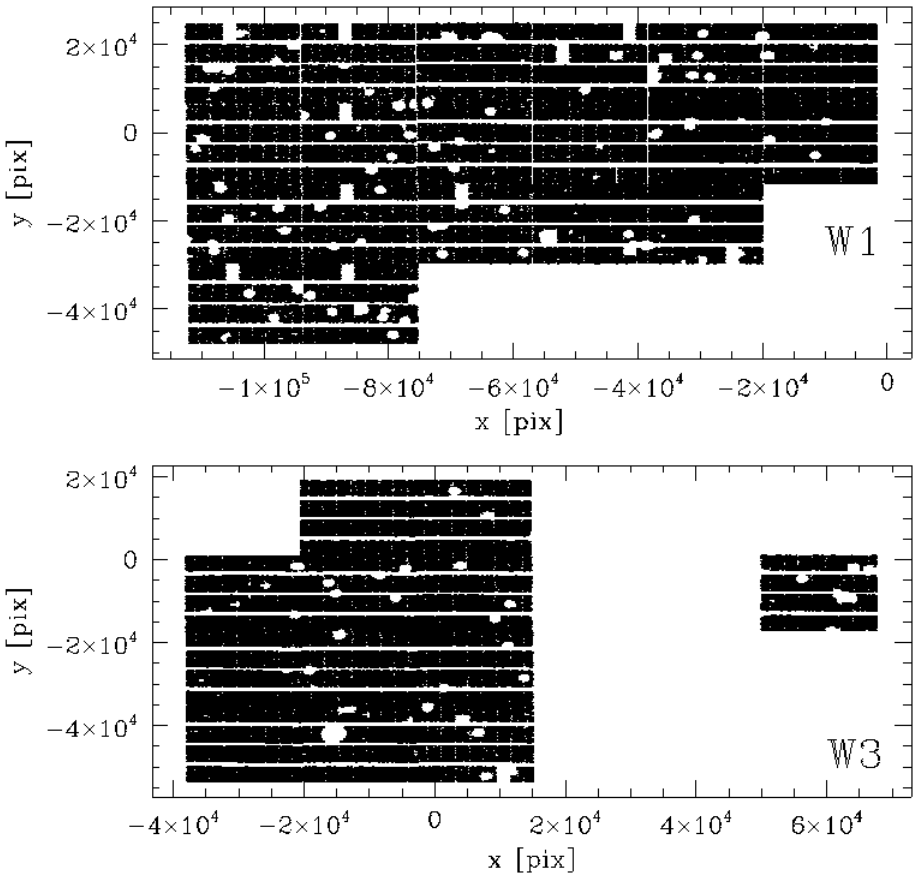

Figure 5.2: CFHTLS observations of W1 and W3 fields. The effective area is approximately 22 sq. degrees from 31 pointings. Bright stars and bad pixels are masked.

Any images with poor seeing or extreme PSF anisotropy are excluded from the stacks. The stacks for this CFHTLS data were created by Henk Hoekstra using the SWarp routine. The stacks are created from 6 or 7 individual images of 620 second exposures, thus each stack is $>$1 hour and reaches a depth of $\sim$25 in i$'$.

5.3.1 Shape Measurements

The carefully stacked i$'$ images were processed with the peak finding algorithm of KSB (1995). Objects which were detected to be more than 5σ above the sky background were added to the source catalogue. The catalogue is then cleaned to include only objects larger than the PSF. These objects are then analyzed in more detail in order to determine their apparent i$'$ magnitudes and half-light radii, as well as their shape parameters. The shape is defined by two polarization "vectors" (equations 2.18 and 2.19), which are combinations of weighted quadrupole moments.

Without the availability of redshift or colour information, galaxies must be separated into source and lens catalogues based only upon their i$'$ magnitude. This means that there will be some overlap in the redshifts of the lens and source populations which must be statistically accounted for in the analysis. The lenses were defined as having $19 < i' < 22$ and the sources have $22.5 < i' < 24.5$. Figure 5.3 shows the magnitude distribution for the entire sample of galaxies in the W1 and W3 fields used.

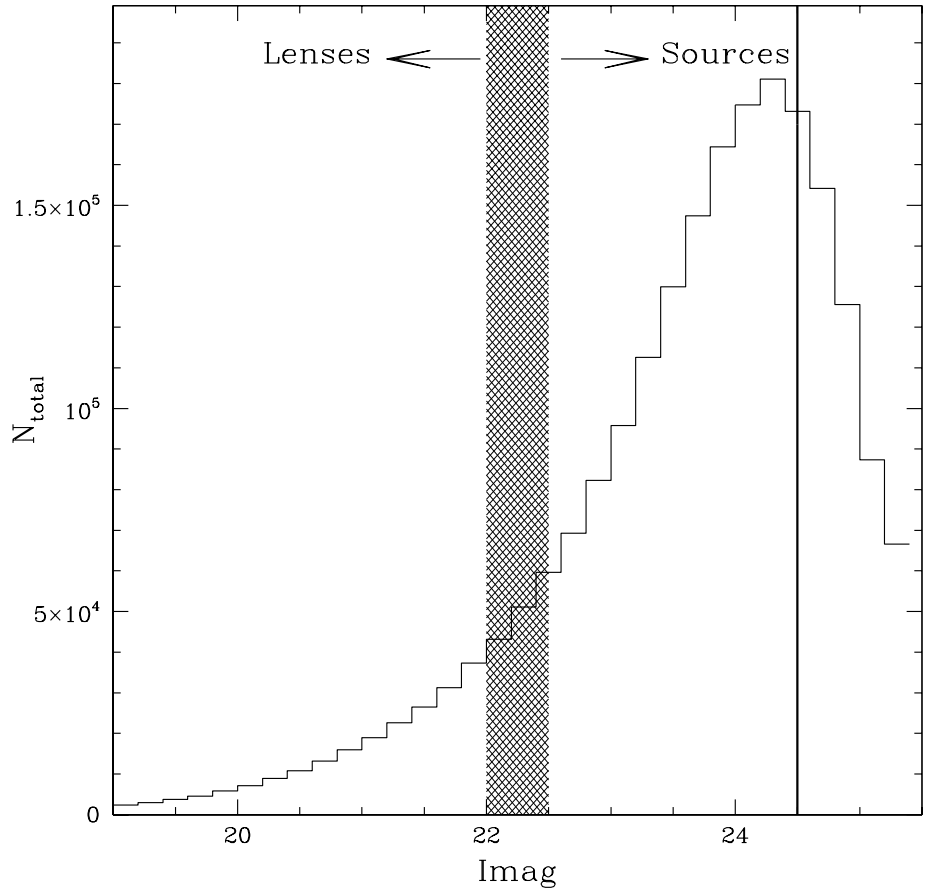

Figure 5.3: Lens and source magnitude distributions. This histogram shows the distribution of magnitudes for all galaxies in the W1 and W3 fields used in this analysis. The hatched region divides the lenses and the sources, and the vertical line at i'=24.5 shows the upper limit for source magnitudes.

Shape Corrections

The measured shapes must be corrected for distortions such as the effects of seeing and PSF anisotropy. This is done following the techniques outlined in KSB (1995) and Hoekstra et al. (1998). A sample of stars is found in the images and they are used to characterize the seeing and any anisotropy in the PSF. The shapes of the stars are fit with a polynomial for each chip in the CFHTLS stacks individually. The shapes of the stars are then used to correct the shapes of all of the galaxies. The catalogues were created by Henk Hoekstra and provided to us with the position, magnitude, shape, error and P^{γ} information. The procedure outlined here to correct the galaxy shapes was recently tested in the Shear TEsting Program (Heymans et al., 2005), and was shown to be very effective. The shear calculated using this method on simulated images was accurate to within $\sim$2%.

5.4 Redshift Distribution of Lens and Source Galaxies

For the analysis presented here, we select a sample of lenses and sources on the basis of their apparent i' magnitude. We define galaxies with $19 < i' < 22$ as lenses, and galaxies with $22.5 < i' < 24.5$ as sources which are used to measure the lensing signal. This selection yields a sample of $\sim 1 \times 10^5$ lenses and $\sim 1.3 \times 10^6$ sources. These catalogues are used to generate 3.7×10^7 lens-source pairs within a projected radius of 2 arcminutes of the stacked lenses. All lens-source pairs within 7 arcseconds of the host galaxy are eliminated

from the catalogue since their shape measurements are likely compromised by light from the host lens.

The lensing signal for an isothermal sphere is a function of $\langle\beta\rangle$, the average ratio of the angular diameter distances between the lens and source, and the source (equation 2.25). Therefore, in order to interpret the detected shear measurements it is necessary to know the redshifts of both the lenses and the sources. If the precise redshifts are not know for each object then at least their distributions must be understood in order to convert shear measurements into properties such as velocity dispersions and halo mass. The CFHTLS data used here were available in one colour only, and so the redshift distributions of the sources and lenses must be estimated. The lack of redshift information limits the accuracy of measurements (Schneider and Rix, 1997; Kleinheinrich et al., 2005). The shear can only be estimated in projected angular bins and not physical units such as kiloparsecs. Therefore, the lensing signal for a distant galaxy is measured on a much larger physical scale than for the case of a closer galaxy. The mixing of scales complicates the interpretation of the results, but we can still learn about the average properties of halos.

The lens catalogues contain relatively bright galaxies, and therefore the distribution of the redshifts is quite well understood from previous studies, such as the CNOC2 field galaxy survey (Lin et al., 1999). It is much more difficult to estimate the redshifts of faint sources, since there are not many spectroscopic redshift surveys available for these depths. The redshifts of faint galaxies are generally estimated using photometric redshifts. A spectroscopic study of the Hubble Deep Field (HDF) to depths of $\sim$24 in R_c showed that the spectroscopic redshifts agreed well with the photometric redshifts (Cohen et al., 2000). For

this analysis we will base the source redshifts on the photometric redshifts from the Hubble Deep Fields North and South (Fernández-Soto et al., 1999) and the redshift distributions derived using the COMBO-17 data (Brown et al., 2003; Kleinheinrich et al., 2005). COMBO-17 uses a combination of 17 wide and narrow band filters to measure very accurate photometric redshifts in a 1 sq. degree patch.

The source and lens distributions can be see in Figure 5.4, using the COMBO-17 results. The median lens redshift is ~ 0.4 and the median source redshift is ~ 0.8. The N(z) distribution for the lenses was estimated using the functional form of Brown et al. (2003) based on the COMBO-17 data

$$\frac{dN}{dz} \propto \frac{z^2}{z_*^3} \exp\left[-\left(\frac{\mathrm{z}}{\mathrm{z}_*}\right)^{1.5}\right] \tag{5.1}$$

where z_* is related to median redshift of the distribution by $z_* = z_m$/1.412, and z_m is a function of the observed magnitude.The source redshift distribution used in the analysis was estimated from photometric redshifts in the HDF (Fernández-Soto et al., 1999). The functional form of the N(z)$_{\mathrm{sources}}$ was as follows

$$N(z)_{\mathrm{sources}} = r_{\mathrm{norm}} \left(\frac{z}{z_0}\right)^{\alpha} \exp\left[-\left(\frac{\mathrm{z}}{\mathrm{z}_\mathrm{o}}\right)^{\beta}\right] \tag{5.2}$$

where

$$r_{\mathrm{norm}} = \frac{\beta}{z_0 \Gamma\left(\frac{1+\alpha}{\beta}\right)} \tag{5.3}$$

The values for α, β and z_0 were supplied by Ludo van Waerbeke based on the magnitude cuts we assumed for our sources.

The N(z) distributions can then be used to estimate the angular diameter distances to the lenses and sources. Assuming a standard ΛCDM cosmology this results in a $\langle\beta\rangle$ of 0.44$\pm$0.02, assuming the COMBO-17 N(z) for the sources. Using the photometric redshift N(z) from the Hubble Deep Fields leads to a $\langle\beta\rangle$ of 0.46$\pm$0.02, where the error is from the field-to-field variations in the HDFs, and the finite number of galaxies. Future CFHTLS analyses will benefit from known redshifts for each lens and source pair.

5.5 Analysis

The lenses are stacked together and the sources that lie within a projected radius of 2 arcminutes are divided into radial bins. The component of their shape tangential to the lens centre is determined and averaged in each bin. Each shear calculation is weighted by the error in the shape measurement as described in Hoekstra et al. (2000). Galaxy-galaxy lensing measurements also have a convenient built-in systematic test. If the tangential lensing signal detected is due to gravity then it should vanish if the source images are rotated by 45 degrees. The tangential and "cross" shear for the entire sample are plotted in Figure 5.5. These data are best fit with an isothermal sphere with Einstein radius of $0\farcs202\pm0\farcs016$. A lensing signal is detected at high significance ($> 12\sigma$). The cross-shear measurement is consistent with 0, as expected, and therefore the tangential signal is interpreted as being caused by weak lensing from an

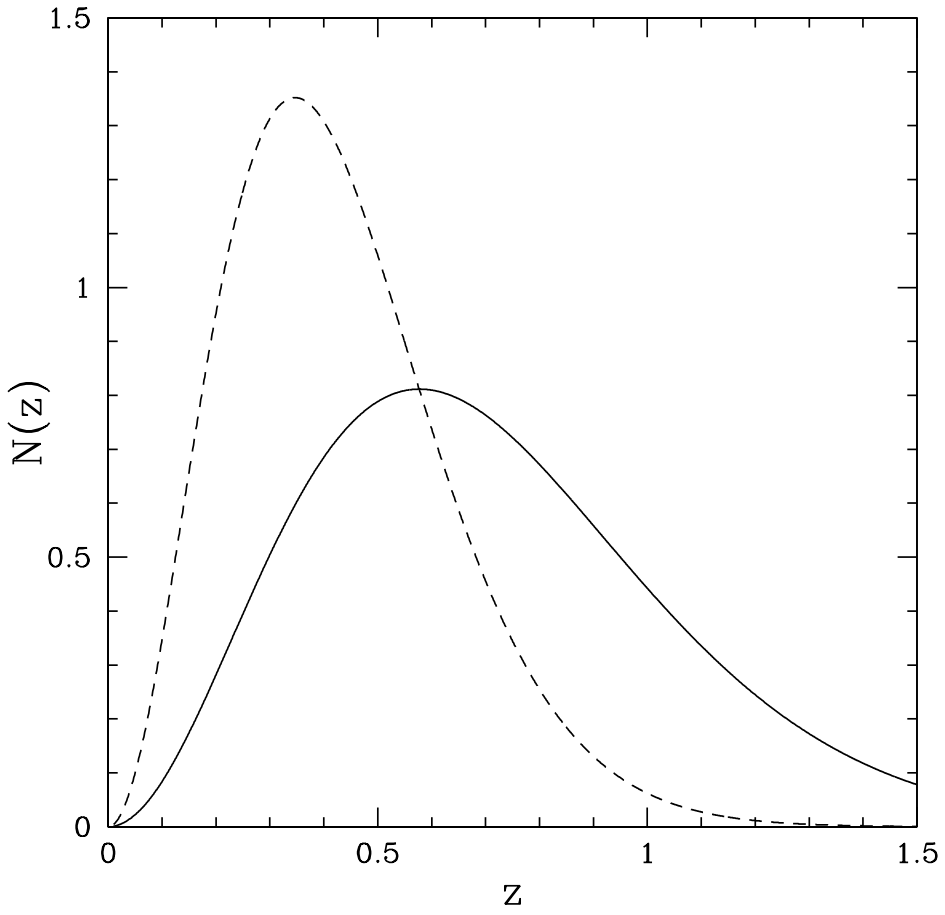

Figure 5.4: N(z) distribution. The lens distribution is shown with the dashed line and has a median z ~ 0.4. The sources are shown with the sold line and have a z~ 0.8

isothermal sphere potential.

In addition to measuring the lensing for the entire sample of lenses, the tangential shear was measured for a brighter sample consisting of galaxies brighter then 20.5 in i′. The results are plotted in Figure 5.6. The shear is best fit by an isothermal sphere with an Einstein radius of $0\farcs361 \pm 0\farcs044$. The $\langle\beta\rangle$ for the bright lenses was 0.69 ± 0.04 and the median redshift was 0.23.

5.5.1 Velocity Dispersion

For an isothermal sphere the tangential shear is proportional to the Einstein radius and hence to the velocity dispersion squared (equations 2.5 and 2.16). The best fit Einstein radius for the entire sample (Figure 5.5) yields a velocity dispersion of 121 ± 9 km s^{-1}. The bright sample of galaxy lenses has a velocity dispersion of 132 ± 16km s^{-1}. This velocity dispersion depends on the sample of lenses used and must be scaled in order to compare to other results. This can easily be done by assuming a scaling relation between luminosity and velocity dispersion as follows

$$\frac{\sigma}{\sigma_*} = \left(\frac{L}{L_*}\right)^{1/\alpha} \tag{5.4}$$

where σ_* is the velocity dispersion of an L_* galaxy. The scaling factor α is generally assumed to be 3 or 4, motivated by the observations or the Faber-Jackson relation, for example. We based our L_* galaxy on the CNOC2 luminosity function results (Lin et al., 1999). Our lenses are known to have a median redshift of 0.4 and the CNOC2 galaxy luminosity function was calculated at a redshift

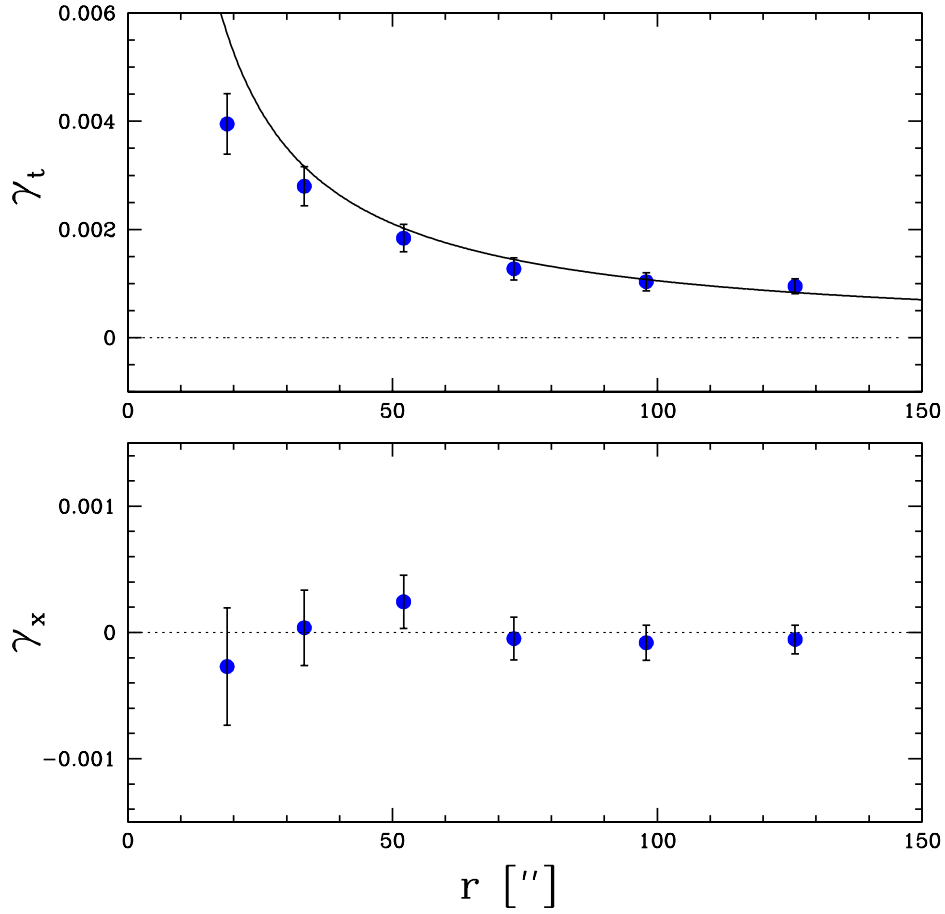

Figure 5.5: (a) The ensemble averaged tangential shear as a function of radius around a sample of CFHTLS galaxies with $19 \lesssim i' \lesssim 22$. The best fit isothermal sphere, shown with the solid line, yields an Einstein radius of $0\farcs202 \pm 0\farcs016$, corresponding to a velocity dispersion of 121 ± 9 km s^{-1}.(b) The signal when the source images are rotated by 45°. Note the difference in scales between the top and bottom figures. No signal is present as expected if the signal in (a) is due to gravitational lensing.

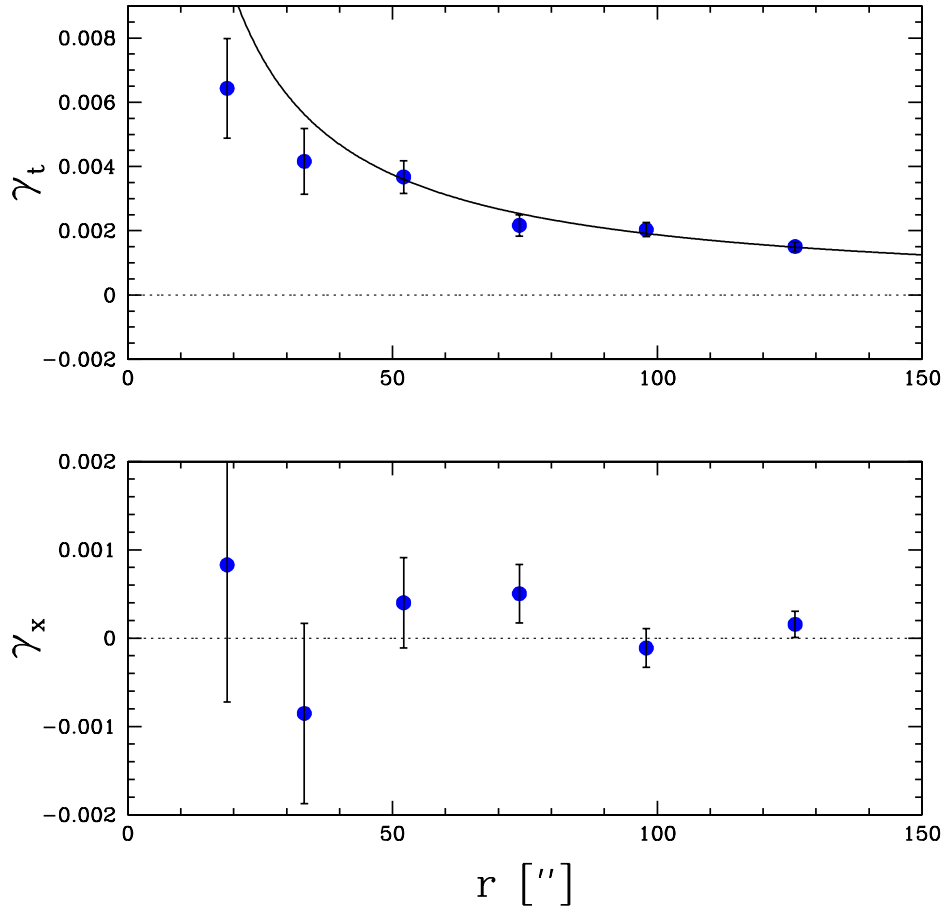

Figure 5.6: (a)The ensemble averaged tangential shear as a function of radius around a sample of bright CFHTLS galaxies with $i' \lesssim 20.5$. The best fit isothermal sphere, shown with the solid line, yields an Einstein radius of $0\farcs361 \pm 0\farcs044$, corresponding to a velocity dispersion of 132 ± 16 km s^{-1}.(b) The signal when the source images are rotated by 45°. No signal is present as expected if the signal in (a) is due to gravitational lensing.

of 0.3. Unfortunately the results of Lin et al. were not evaluated for a ΛCDM cosmology, and therefore their results had to be corrected for the cosmology assumed here. Furthermore the CNOC2 results were quoted in the $R_{\rm c}$ band while our images are i′. We used the colour and k-corrections from Frei and Gunn (1994) to convert our magnitudes to $R_{\rm c}$ and evaluate our characteristic luminosity at a redshift of 0.3. Using the proportion of early and late types of galaxies found in the CNOC2 redshift survey (21% early types, 17% intermediate types, 62% late types) we estimate that an L_* galaxy has a characteristic luminosity of $1.3\times10^{10}h^{-2}\mathrm{L}_{\odot R_{\rm c}}$.

The Einstein radius for an L_* galaxy is given by

$$\theta_E = \frac{4\pi}{c}\frac{\sigma_*^2}{L_*^{2/\alpha}}\langle\beta L^{2/\alpha}\rangle \tag{5.5}$$

where σ_* is the velocity dispersion for an L_* galaxy and θ_E is in radians. We estimate the average luminosity for our lens galaxies to be $\langle L\rangle$=$7.9\times10^{9}h^{-2}\mathrm{L}_{\odot R_{\rm c}}$. The scaled velocity dispersion can now be estimated for different assumed α values. The results of scaling the observed σ for our sample of lenses to a typical L_* galaxy can be seen in Table 5.1.

5.5.2 Halo Masses

The total extent and mass of dark matter halos can be estimated assuming a mass model for the galaxy halos as suggested by Brainerd, Blandford and Smail (1996) with a density profile

$$\rho(r) = \frac{\sigma^2 s^2}{2\pi G r^2 (r^2 + s^2)} \tag{5.6}$$

where s is a measure of the truncation scale of the halo. This profile is an isothermal sphere at small radii with a cut-off at large radii, characterized by the scale parameter s, which scales with velocity dispersion (Schneider and Rix, 1997)

$$s = s_* \left(\frac{\sigma}{\sigma_*}\right)^2 \tag{5.7}$$

Assuming this truncated isothermal sphere halo model, the mass enclosed within a sphere of radius r is

$$M(r) = \frac{2\sigma^2 s}{G} \arctan(r/s) \tag{5.8}$$

which, because of the truncation, results in a finite mass (Hoekstra et al., 2004)

$$M_{\rm tot} = \frac{\pi \sigma^2 s}{G} = 7.3 \times 10^{12} \left(\frac{\sigma}{100 {\rm kms}^{-1}}\right)^2 \left(\frac{s}{1{\rm Mpc}}\right) \tag{5.9}$$

The truncation scale can be assumed to be constant for all halos, in which case the M/L ratio would be $\propto {\rm L}^{1/2}$, if ${\rm L} \propto \sigma^4$. Alternatively, it can be assumed that M/L is constant for all galaxy halos in which case $s \propto \sigma^2$ (Brainerd et al., 1996; Hudson et al., 1998).

Assuming the truncation radius found by Hoekstra et al. (2004) for an L_* galaxy of 185±30 kpc we estimate the total mass of our L_* galaxy to be $2.5 \pm 0.4 \times 10^{12}\ h^{-1}{\rm M}_\odot$ if ${\rm L} \propto \sigma^4$, and $2.8 \pm 0.5 \times 10^{12}\ h^{-1}{\rm M}_\odot$ if ${\rm L} \propto \sigma^3$. The results are in good agreement with the results from the Red-Sequence Cluster

$<\sigma^2>^{1/2}$ km s^{-1}	α	σ_* km s^{-1}	$M_{\rm total}$ $h^{-1}M_\odot$	M_{200} $h^{-1}M_\odot$	M/L h $M_\odot/L_{R_c\odot}$
121±9km	4	137±10	2.5±0.4×10^{12}	1.7±0.3×10^{12}	130±26
121±9km	3	143±11	2.8±0.5×10^{12}	1.9±0.3×10^{12}	145±29

Table 5.1: Velocity dispersions and masses for 2 scaling laws. The quoted errors do not include mass model uncertainties.

Survey (Hoekstra et al., 2004), which found total halo mass to be 2.5± 0.4 $\times 10^{12}$ h^{-1}.

We can use the luminosity of an L_* galaxy together with the velocity dispersion estimate above in order to calculate a typical M/L ratio. We evaluated M/L at the approximate virial radius of r_{200}. The mass inside r_{200} for an L_* galaxy was estimated to be $1.7 \pm 0.3 \times 10^{12}$ $h^{-1}M_\odot$, assuming an isothermal sphere model. This leads to a M/L ratio of 130±26 $hM_\odot/L_{R_c\odot}$.

5.6 Halo Shapes

An important insight into the nature of dark matter comes from the shapes of dark matter halos. Dynamical measurements can be used to trace out the halo shapes on small scales, but they can not be used on larger scales where there are no visible tracers. Numerical simulations of CDM indicate that dark matter halos should be flattened, and more often prolate than oblate (Dubinski and Carlberg, 1991; Springel et al., 2004). Simulations of self-interacting dark matter produce more spherical halos (Davé et al., 2001). Alternative theories

of gravity, as introduced in Chapter 1, attempt to explain astrophysical observations by modifying gravity rather than invoking non-baryonic dark matter. One of the strongest pieces of evidence for the presence of dark matter on scales from galaxies through clusters and large-scale structure has been gravitational lensing, both weak and strong. Non-relativistic theories of modified gravity can not provide predictions for lensing measurements, and therefore can not be tested by lensing observations. However, there is now a candidate relativistic modified gravity theory as presented by Bekenstein (2004) which can be used as an alternative to dark matter to explain relativistic phenomena such as lensing. Thus far this theory appears to match many observations (Skordis et al., 2005; Zhao et al., 2005). One interesting test for this theory is the inferred shapes of galaxy dark matter halos from weak lensing.

Modified gravity theories predict that the lensing signal is due to the observed luminous material, and thus any anisotropy in the lensing measurement is due to the anisotropy in the distribution of gas and stars. Therefore, on small scales you would expect the lensing signal to be anisotropic since galaxies themselves are, but on the large scales probed by galaxy-galaxy lensing you would expect a nearly isotropic signal since there is no luminous material present at large radii from the galaxy centre. If a highly anisotropic signal is detected at large radii this provides an interesting constraint on modified gravity theories, and provides supporting evidence for dark matter theories. This should be possible with the full CFHTLS data set.

Galaxy-galaxy lensing measurements generally assume that dark matter halos are spherical, but a recent galaxy-galaxy measurement by Hoekstra et al. (2004) detected a significant flattening of dark matter halos. This result was

not observed in the latest analysis of SDSS data by Mandelbaum et al (2005). We decided to test for halo flattening using this early CFHTLS data.

Brainerd & Wright (2000) discussed how to measure halo shapes by looking for an anisotropic galaxy-galaxy lensing signal. The CFHTLS data at the end of the survey will be far superior in addressing the question of galaxy shapes since not only will there be much more data but there will be photometric redshifts for every lens and source thus allowing the analysis to be carried out in physical units. One simple approach to try and detect if galaxy dark matter halos are non-spherical is to test whether the tangential shear signal is different along the semi-major and semi-minor axes of the visible galaxy. It is important to note that this technique only works under the assumption that the dark matter halo is aligned with the galaxy. If the halo flattening is not correlated with the disk orientation then this simple measurement is much more difficult to interpret, or there may not be any anisotropic signal detected. The analysis described in the previous sections was repeated for the galaxy lenses, this time dividing the sources into those within 45 degrees of the semi-major axis and those within 45 degrees of the semi-minor axis (see the schematic in Figure 2.10). The tangential shear results can be seen in Figure 5.7. The signal from the two angular bins of sources is very similar. The best fit isothermal spheres yield Einstein radii of $0\farcs176\pm0\farcs017$ and $0\farcs212\pm0\farcs024$, corresponding to velocity dispersions of 113 ± 11 km s $^{-1}$ and 124 ± 14 km s $^{-1}$, respectively.

Following Brainerd & Wright we calculated the ratio of $\langle\gamma\rangle_{\rm minor}$ to $\langle\gamma\rangle_{\rm major}$. The results are plotted in Figure 5.8 and the best fit value was 0.73 ± 0.15 indicating a $\sim2\sigma$ detection of non-sphericity for dark matter halos. Our best fit shear ratio indicates that the halo has an ellipticity of ~0.3 (see Figure 5.9). If

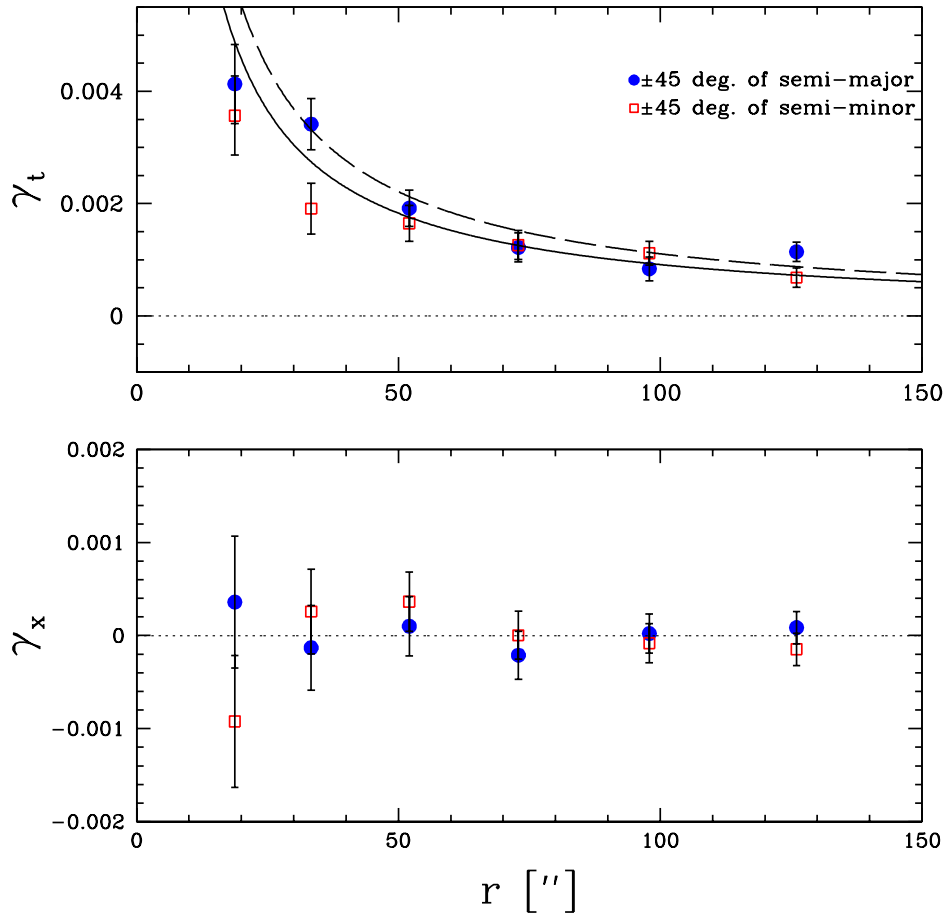

Figure 5.7: Mean tangential shear for sources close to the semi-major axes (filled circles) and close to the semi-minor axis (open squares). The best fit isothermal sphere for the sources within 45° of the semi-major axes yields an Einstein radius of 0.″212±0.″024 corresponding a velocity dispersion of 124±14 km s $^{-1}$. The best fit isothermal sphere for the sources within 45° of the semi-minor axes yields an Einstein radius of 0.″176±0.″017 corresponding a velocity dispersion of 113±11 km s $^{-1}$

we restrict ourselves to the shear signal from within 50 arcseconds (to better match the simulations from Brainerd & Wright) we get find $\langle\gamma\rangle_{\rm minor}$ /$\langle\gamma\rangle_{\rm major\rangle}$ = 0.78$\pm$0.13, also favouring a halo shape with e $\sim$0.3. With more data the precision of this measurement will improve and we will be able to better estimate the ellipticity of dark matter halos.

A recent analysis of isolated galaxies in the SDSS indicated that there are more satellite along the major axes of a galaxy, than the minor axes (Brainerd, 2005). This, together with the suggestion that satellites are radially aligned with their hosts (as discussed in Section 2.3), indicates that the measured flattening from galaxy-galaxy lensing may be underestimating the true halo flattening. The signal along the major axes will be more affected by the radially aligned satellites than signal along the minor axes. In order to quantify this effect it would be interesting to measure the preferred alignment of satellite galaxies, divided by their position angle with respect to their host galaxy. It is possible that all satellites will follow the same radial alignment trend, regardless of their position with respect to their host, or it is possible that the galaxies close to the major axes are more or less aligned than those close to the minor axes. Galaxy-galaxy lensing measurements using redshift information can eliminate this potential contaminant.

5.7 Summary

We have used early i' from the CFHTLS to detect a galaxy-galaxy lensing signal, and to constrain the velocity dispersion of galaxy halos at a redshift of

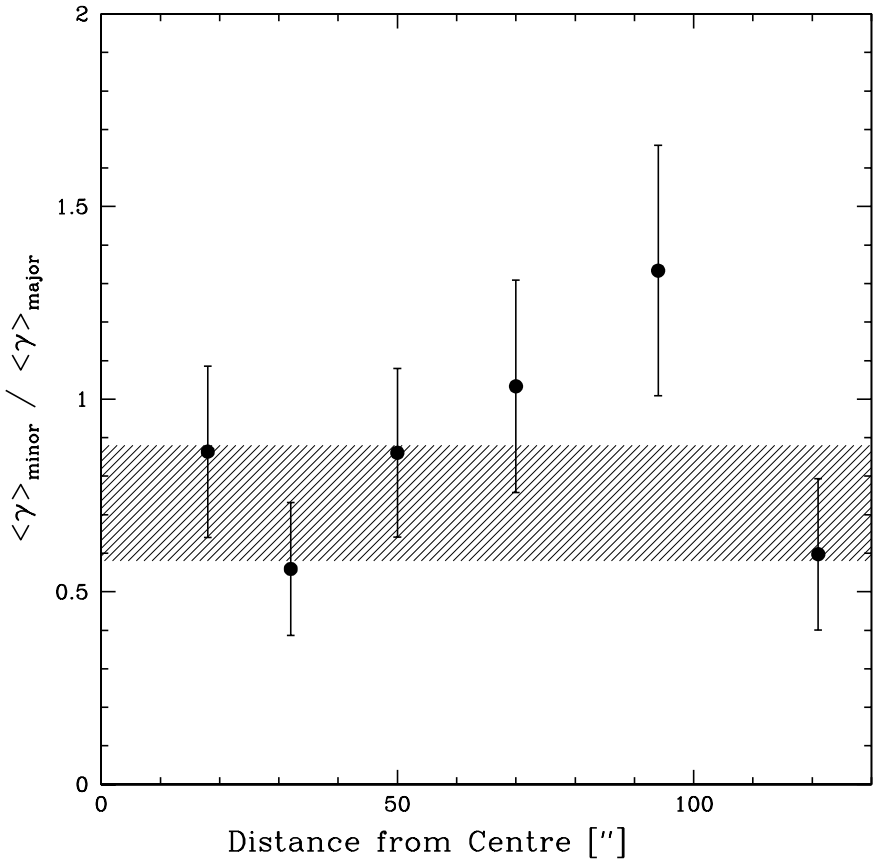

Figure 5.8: Ratio of mean shear experienced by sources closest to minor axis of an elliptical lens to those experienced by sources closest to the major axes.

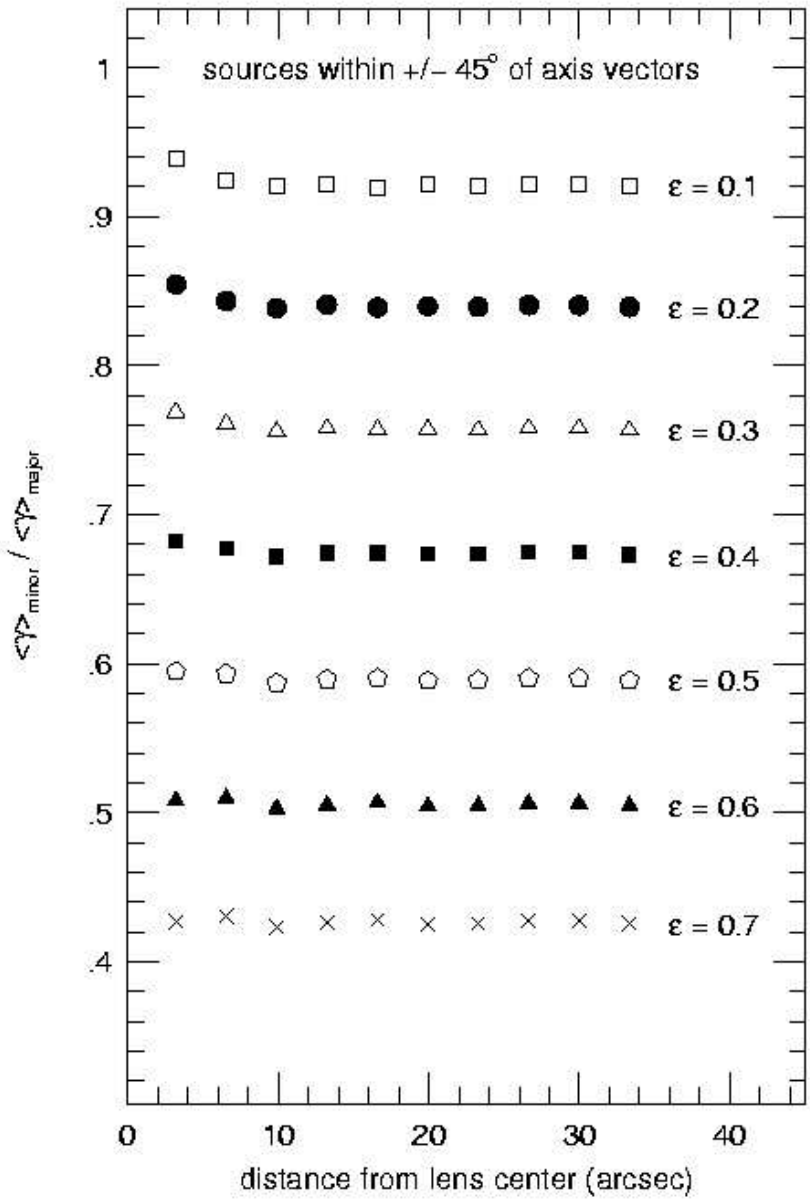

Figure 5.9: Ratio of mean shear experienced by sources closest to minor axis of an elliptical lens to those experienced by sources closest to the major axes for model data from Brainerd & Wright (2000).

0.3. The measured σ from an L_* galaxy is 137$\pm$10 km s^{-1} (circular velocity V_*=194$\pm$14km s^{-1}). A galaxy-galaxy lensing analysis of the COMBO-17 data by Kleinheinrich et al. (2005) estimated the value for σ_* for both the situation that a redshift was known for every source and lens, and for the situation that no redshift information is available. The latter case can be compared with our results. They obtained a mean σ_* of 156^{+24}_{-30} km s^{-1}. Hoekstra et al. (2005) used data from the Red-Sequence Cluster Survey (RCS) to estimate the properties of galaxy dark matter halos using galaxy-galaxy lensing without redshift information. They found a value for σ_* of 136$\pm$8 km s^{-1}. It is important to note that the estimate for L_* is slightly different in each of these studies, but the results agree within errors.

In addition, we were able to estimate the total mass of an L_* galaxy at redshift 0.3 to be 2.5$\pm$0.32 $\times 10^{12}$ $h^{-1}M_\odot$. This is in good agreement with the results from RCS where the mass of L_* halos was estimated at 2.5$\pm$0.26 $\times 10^{12}$ $h^{-1}M_\odot$. Our measured velocity dispersion for an L_* galaxy is also in agreement with results from fundamental plane measurements (Sheth et al., 2003). There was also some evidence for flattened dark matter halos, though a definitive answer awaits more data.

5.8 Future Work and Conclusions

Galaxy-galaxy lensing is a unique and powerful tool for studying the dark matter halos of galaxies to large projected distances. This technique has now been applied many times to try and uncover the properties of galaxy halos, but with

planned and ongoing major surveys the results will get even better. Any complete theory of galaxy formation must be able to to properly map both the baryonic and dark matter components of galaxies, and understanding which galaxies live in which halos is a major piece of this puzzle. Most observational projects help in understanding the baryonic component of galaxies, while simulations are best at explaining the dark matter. Gravitational lensing has an important role to play in uniting simulations and other observations by connecting galaxies to their halos.

There is clearly much more that can and will be done with the entire CFHTLS data set. In particular, having photometric redshifts will aid the analysis immensely. At present, we have lenses and sources over a wide range of redshifts and are estimating shear in angular bins which mix together many physical scales. Furthermore, photometric redshifts will permit a clear division between lens and source populations, rather than a statistical one based upon observed magnitudes as used here. Redshift information also permits the division of lenses into different redshift bins, thus allowing the study of halo evolution. We also plan to measure the morphologies of all of the lens galaxies so that we can divide the sample into early and late-types and try to detect differences in their halo masses, shapes and M/L ratios. Furthermore, with the complete data set we should have sufficient statistical power to be able to distinguish between dark matter profiles in the inner regions of galaxies. For example, we should be able to tell whether the tangential shear is best fit by an NFW profile, an isothermal sphere or a Moore profile (Moore et al., 1999). It is possible, however, that the mass profile in the inner regions of galaxy halos is influenced by the baryonic galaxy. Therefore, an interesting galaxy-galaxy lensing study

could use a sample of low surface brightness galaxies which are more diffuse and the dark matter halos would not be significantly influenced by baryons. The background sources should be visible through the galaxy. The most challenging aspect of such a project would be identifying a sufficiently large sample of such galaxies.

The results in this chapter provide only a hint of what is to come with 5 full years of data from CFHTLS. The quantity and quality of the data from this survey are ideal for weak lensing analysis. These data are also being used for cosmic shear measurements which will constrain the matter power spectrum, and in particular σ_8. In addition, the measurements can be used to constrain Ω_m, w and the bias parameter, b.

Chapter 6

Conclusions

In other words, apart from the known and the unknown, what else is there?

— Harold Pinter

The history of weak lensing is young; the first galaxy-galaxy lensing detection was reported only a decade ago (Brainerd et al., 1996). The field of weak lensing is just coming of age now in this exciting time for cosmology. This tool can be used to study mass on scales ranging from galaxies to large scale structure. It is interesting that while the cosmological parameters are becoming known with ever-increasing precision, there are still so many unanswered questions surrounding the details of baryonic physics and galaxy formation.

It is clear that cosmology must now move from a study concerned only with fundamental parameters to one that also studies the messy "gastrophysics" that is essential in the processes involved in galaxy formation. Understanding the link between the luminous galaxies we observe and the dark matter halos in

which they reside provides interesting constraints on galaxy formation and also important input for simulations. At present, simulations describe very well the formation and evolution of dark matter halos, but fail to capture all of the details in the evolution of their baryonic galaxies. Understanding which galaxies live in which halos will provide necessary constraints to the simulators, and weak lensing can aid in this understanding.

6.1 Summary of Results

This thesis has used weak lensing to study two very interesting mass scales – galaxy groups and galaxy halos. Most galaxies in the present-day universe live in galaxy groups and therefore understanding their properties leads to insights about the universe. Understanding the M/L ratio of galaxy groups is also important for insights into the nature of dark matter. The M/L ratio is constant as function of radius in galaxy clusters (Carlberg et al., 1997) but rises rapidly with radius on galaxy scales (Rubin, 1983). Thus, there is segregation between mass and light on some scale. We did not detect a varying M/L with radius in our sample of groups, but we did find a sharp rise in M/L as a function of group mass. This indicates that the mass scale $\sim 10^{13} M_{\odot}$ may mark the divide between actively star-forming field galaxies and more passively evolving cluster galaxies.

There are still many outstanding questions about galaxy groups which can be addressed with weak lensing. One challenge is the difficulty in identifying large well-understood sample of groups to be studied with lensing. Large red-

shift surveys are making this easier, particularly for low redshift groups where many group members can be identified and accurate velocity dispersions estimated. Ultimately a large sample of groups of varying redshifts and velocity dispersions is needed to try and understand the properties and evolution of galaxy groups.

We also carried out a study of galaxy dark matter halos using weak lensing with early CFHTLS data. We were able to detect a tangential shear signal at high significance and use this to infer an average velocity dispersion for an L_* galaxy. With more data we will be able to study the evolution of this velocity dispersion as well as constrain the size and shape of galaxy halos. Significant improvements to the galaxy-galaxy lensing measurements can be made by including photometric redshift information and doing a full maximum likelihood analysis to fit for the velocity dispersion and the extent of halos. Galaxy-galaxy lensing will remain a statistical measurement but with ever-increasing survey sizes it is becoming possible to divide the sample of lenses into many subsamples divided by luminosity, redshift, colour or morphology.

6.2 Future Work

The new field of weak gravitational lensing has an exciting future. There are many planned ground and space-based surveys. The strategy for lensing is to image huge fields with the best image quality possible, which creates a wealth of data useful for many scientific purposes. The main driver for many of the weak lensing surveys is the measurement of cosmic shear, and the estimation

of cosmological parameters. I am particularly interested in the use of galaxy-galaxy lensing to try and uncover some of the mysteries of galaxy formation.

With ever more data available for weak lensing studies understanding systematic errors becomes much more important. Historically, statistical errors were significant for weak lensing measurements, but we can see from the results presented here based on the early CFHTLS data that statistical errors are now very small. This means that innovative analysis techniques must be developed to better understand and correct for all possible systematics. One very promising new tool is the shapelets formalism (Refregier and Bacon, 2003) which is used to decompose the images of galaxies into a set of orthogonal basis functions. This method allows the more accurate determination of galaxy shapes (higher order than KSB) but the functions also have some useful mathematical properties which make them very convenient for estimating shear. Innovative analysis techniques, such as shapelets, will be useful for data with complicated PSFs, for example, but current analysis tools such as the KSB method have proven to have very small systematic errors (Heymans et al., 2005). The current limitation for galaxy-galaxy and cosmic shear lensing results is the determination of accurate source redshifts. The N(z) distribution must be very well understood in order to convert measured shear signals into physical quantities, such as mass, or cosmological parameters.

Systematic errors can also be minimized by escaping the atmosphere and carrying out observations from space. Space-based images generally have small and stable PSFs, and a larger number of sources at a given magnitude limit can be resolved compared with ground-based observations. However, space observations are limited by small fields and expense. At present the only

optical telescope in space is the Hubble Space Telescope, which has been used extensively for lensing. But it has a limited remaining lifetime and a relatively small field-of-view. The replacement for Hubble, the James Webb Space Telescope, is planned for launch sometime after 2013. This telescope will operate in the near-infrared and have a relatively small field-of-view imager. There is also a proposed Joint Dark Energy Mission (JDEM) which would launch around 2013 and would be a ~ 2 metre telescope designed to understand the properties of dark energy through studies of cosmic shear and type Ia supernovae. The telescope would be dedicated to the dark energy survey and would image roughly 1000 square degrees of the sky per year with a variety of filters, optimized for photometric redshift determination. While the ultimate goal of JDEM is to measure the dark energy equation of state and its evolution, the data will be ideal for galaxy-galaxy lensing measurements. The increased resolution will allow for very accurate shape measurements, but also the calculation of detailed morphologies for all of the lenses. This data will be well-suited for studying the weak lensing of galaxies as a function of their observed properties as well as their evolution to a redshift of ~ 1.

The prospect of huge imaging surveys from space is very exciting for galaxy-galaxy lensing, but in the near future there are many ambitious ground-based projects planned. Firstly, the area and depth of the CFHTLS will remain unmatched for the next few years. With all of the CFHTLS data in hand we will be able to detect the evolution in galaxy dark matter halos to a redshift of ~ 0.7 and constrain their sizes and shapes to unprecedented precision. The CFHTLS will be complemented by large survey programs in the south to be carried out in the optical with Omegacam on VST and in the infrared with VISTA. The VST

survey will not be quite as deep as CFHTLS but will image $\sim$ 1000 sq degrees. The near-infrared data from VISTA will be used to improve photometric redshifts. In the slightly longer-term, the large synoptic survey telescope (LSST) will image 20 000 sq degrees of the sky with repeated exposures to look for transient objects such as Kuiper Belt Objects and supernovae. The deep multi-band data will be ideal for photometric redshift and lensing measurements. The telescope is currently scheduled for completion in 2012.

The work in this thesis provides just a hint of what is to come for weak lensing on galaxy and group scales. Many of the remaining question in galaxy formation require an understanding of the relationship between observed galaxies and the unseen dark matter halos in which they reside. Weak gravitational lensing plays a very important role in linking these.

Bibliography

Agustsson, I. and Brainerd, T. G.: 2005, *e-print astro-ph/0509405*

Aharmim, B. et al.: 2005, *e-print nucl-ex/0502021*

Alcock, C. et al.: 2001a, *Astrophysical Journal* **550**, L169

Alcock, C. et al.: 2001b, *Astrophysical Journal Supplement Series* **136**, 439

Bacon, D. J., Massey, R. J., Refregier, A. R., and Ellis, R. S.: 2003, *Monthly Notices of the Royal Astronomical Society* **344**, 673

Bacon, D. J., Refregier, A. R., and Ellis, R. S.: 2000, *Monthly Notices of the Royal Astronomical Society* **318**, 625

Bahcall, N. A., Lubin, L. M., and Dorman, V.: 1995, *The Astrophysical Journal* **447**, L81

Barnes, J. E. and Hernquist, L.: 1992, *Annual Review of Astronomy and Astrophysics* **30**, 705

Bartelmann, M. and Schneider, P.: 2001, *Physics Reports* **340**, 291

Bekenstein, J. D.: 2004, *Physical Review D* **70**, 1

Benabed, K. and van Waerbeke, L.: 2004, *Physical Review D* **70**, 1

Bennett, C. et al.: 1992, *The Astrophysical Journal* **396**, L7

Benson, A., Cole, S., Frenk, C., Baugh, C., and Lacey, C.: 1992, *Monthly Notices of the Royal Astronomical Society* **311**, 793

Bernstein, G. M. and Jarvis, M.: 2002, *Astronomical Journal* **123**, 583

Bernstein, G. M. and Norberg, P.: 2002, *Astronomical Journal* **124**, 733

Bertin, E. and Arnouts, S.: 1996, *Astronomy and Astrophysics Supplement* **117**, 393

Birnboim, Y. and Dekel, A.: 2003, *Monthly Notices of the Royal Astronomical Society* **345**, 349

Bond, J., Cole, S., Efstathiou, G., and Kaiser, N.: 1991, *The Astrophysical Journal* **379**, 440

Bottema, R., Pestana, J. L., Rothberg, B., and Sanders, R. H.: 2002, *Astronomy and Astrophysic* **393**, 453

Bradac, M. et al.: 2005, *Astronomy and Astrophysics* **437**, 49

Brainerd, T., Blandford, R., and Smail, I.: 1996, *The Astrophysical Journal* **466**, 623

Brainerd, T. G.: 2005, *The Astrophysical Journal Letters* **628**, L101

Brainerd, T. G. and Wright, C. O.: 2000, *e-print astro-ph/0006281*

Branch, D. and Tammann, G. A.: 1992, *Annual Review of Astronomy and Astrophysics* **30**, 359

Briel, U., Henry, J., and Boehringer, H.: 1992, *Astronomy and Astrophysics* **259(2)**, L31

Brown, M. L., Taylor, A. N., Bacon, D. J., Gray, M. E., Dye, S., Meisenheimer, K., and Wolf, C.: 2003, *Monthly Notices of the Royal Astronomical Society* **341**, 100

Bullock, J. S., Kolatt, T. S., Sigad, Y., Somerville, R. S., Kravtsov, A. V.,

Klypin, A. A., Primack, J. R., and Dekel, A.: 2001, *Monthly Notices of the Royal Astronomical Society* **321**, 559

Carlberg, R., H.K.C.Yee, and Ellingson, E.: 1997, *The Astrophysical Journal* **478**, 462

Carlberg, R., H.K.C.Yee, Ellingson, E., Abraham, R., Gravel, P., Morris, S., and Pritchet, C.: 1996, *The Astrophysical Journal* **462**, 32

Carlberg, R. G., Yee, H. K. C., Morris, S. L., Lin, H., Hall, P. B., Patton, D. R., Sawicki, M., and Shepherd, C. W.: 2001, *The Astrophysical Journal* **552**, 427

Chen, J., Kravtsov, A. V., and Keeton, C. R.: 2003, *The Astrophysical Journal* **592**, 24

Cohen, J. G., Hogg, D. W., Blandford, R., Cowie, L. L., Hu, E., Songaila, A., Shopbell, P., and Richberg, K.: 2000, *The Astrophysical Journal* **538**, 29

Cole, S., Aragon-Salamanca, A., Frenk, C., Navarro, J., and Zepf, S.: 1994, *Monthly Notices of the Royal Astronomical Society* **271(4)**, 781

Cole, S. et al.: 2005, *Monthly Notices of the Royal Astronomical Society* **362**, 505

Cole, S., Lacey, C., Baugh, C., and Frenk, C.: 2000, *Monthly Notices of the Royal Astronomical Society* **319**, 168

Contaldi, C. R., Hoekstra, H., and Lewis, A.: 2003, *Physical Review Letters* **90**, 1303

Courbin, F.: 2003, in D. Valls-Gabaud and J.-P. Kneib (eds.), *Gravitational Lensing: a unique tool for cosmology*, A.S.P. Conference Series

Cowie, L. L., Songaila, A., Hu, E. M., and Cohen, J. G.: 1996, *Astronomical Journal* **112**, 839

Cretton, N., Naab, T., Rix, H.-W., and Burkert, A.: 2001, *The Astrophysical Journal* **554**, 291

Dar, A.: 1995, *Astrophysical Journal* **449**, 550

Davé, R., Spergel, D. N., Steinhardt, P. J., and Wandelt, B. D.: 2001, *The Astrophysical Journal* **547**, 574

De Lucia, G., Springel, V., White, S. D. M., Croton, D., and Kauffmann, G.: 2005, *e-print astro-ph/0509725*

Dekel, A. and Birnboim, Y.: 2004, *e-print astro-ph/041230*

Dubinski, J. and Carlberg, R. G.: 1991, *The Astrophysical Journal* **378**, 496

Eke, V. et al.: 2004, *Monthly Notices of the Royal Astronomical Society* **355**, 769

Eke, V. R., Baugh, C. M., Cole, S., Frenk, C. S., King, H. M., and Peacock, J. A.: 2005, *Monthly Notices of the Royal Astronomical Society* **362**, 1233

Fahlman, G., Kaiser, N., Squires, G., and Woods, D.: 1994, *The Astrophysical Journal* **437**, 56

Fernández-Soto, A., Lanzetta, K. M., and Yahil, A.: 1999, *The Astrophysical Journal* **513**, 34

F.Governato, S.Ghigna, B.Moore, T.Quinn, Stadel, J., and Lake, G.: 2001, *The Astrophysical Journal* **547**, 555

Fischer, P. et al.: 2000, *Astronomical Journal* **120**, 1198

Frei, Z. and Gunn, J. E.: 1994, *Astronomical Journal* **108**, 1476

Fukuda, Y. et al.: 1998, *Physical Review Letters* **81**, 1562

Gaitskell, R. J.: 2004, *Annual Review of Nuclear and Particle Science* **54**, 315

Gamow, G.: 1970, *My world line; an informal autobiography*, Viking Press

Gnedin, N. Y.: 2005, *Nature* **435**, 572

Hamana, T., Miyazaki, S., Shimasaku, K., Furusawa, H., Doi, M., Hamabe, M., Imi, K., Kimura, M., Komiyama, Y., Nakata, F., Okada, N., Okamura, S., Ouchi, M., Sekiguchi, M., Yagi, M., and Yasuda, N.: 2003, *The Astrophysical Journal* **597**, 98

Heymans, C. et al.: 2005, *submitted toMonthly Notices of the Royal Astronomical Society, e-print astro-ph/0506112* astro-ph 0506112

Hoekstra, H., Franx, M., and Kuijken, K.: 2000, *The Astrophysical Journal* **532**, 88

Hoekstra, H., Franx, M., Kuijken, K., Carlberg, R., and Gladders, H. Y.: 2003, *Monthly Notices of the Royal Astronomical Society* **340**, 609

Hoekstra, H., Franx, M., Kuijken, K., Carlberg, R., Yee, H., Lin, H., Morris, S., Hall, P., Patton, D., Sawicki, M., and Wirth, G.: 2001, *The Astrophysical Journal* **548**, L5

Hoekstra, H., Franx, M., Kuijken, K., and Squires, G.: 1998, *The Astrophysical Journal* **504**, 636

Hoekstra, H., Yee, H., and Gladders, M. D.: 2004, *The Astrophysical Journal* **606**, 67

Hoekstra, H., Yee, H. K. C., and Gladders, M. D.: 2002a, *The Astrophysical Journal* **577**, 595

Hoekstra, H., Yee, H. K. C., and Gladders, M. D.: 2002b, *New Astronomy Review* **46**, 767

Huchra, J. P. and Geller, M. J.: 1982, *The Astrophysical Journal* **257**, 423

Hudson, M. J., Gwyn, S. D. J., Dahle, H., and Kaiser, N.: 1998, *The Astrophysical Journal* **503**, 531

Jain, B., Seljak, U., and White, S.: 2000, *The Astrophysical Journal* **530**, 547

Jarvis, M., Bernstein, G. M., Fischer, P., Smith, D., Jain, B., Tyson, J. A., and Wittman, D.: 2003, *Astronomical Journal* **125**, 1014

Kaiser, N. and Squires, G.: 1993, *The Astrophysical Journal* **404**, 441

Kaiser, N., Squires, G., and Broadhurst, T.: 1995, *The Astrophysical Journal* **449**, 460

Kauffmann, G., White, S., and Guiderdoni, B.: 1993, *mnras* **264**, 201

Kleinheinrich, M., Rix, H.-W., Erben, T., Schneider, P., Wolf, C., Schirmer, M., Meisenheimer, K., Borch, A., Dye, S., Kovacs, Z., and Wisotzki, L.: 2005, *Astronomy and Astrophysics* **439**, 513

Knop, R. et al.: 2003, *Astrophysical Journal* **598**, 102

Kogut, A., Spergel, D. N., Barnes, C., Bennett, C. L., Halpern, M., Hinshaw, G., Jarosik, N., Limon, M., Meyer, S. S., Page, L., Tucker, G. S., Wollack, E., and Wright, E. L.: 2003, *The Astrophysical Journal Supplement* **148**, 161

Kravstov, A. V. et al.: 2004, *The Astrophysical Journal* **609**, 35

Kroupa, P.: 2001, *Monthly Notices of the Royal Astronomical Society* **322**, 231

Lin, H., Yee, H. K. C., Carlberg, R. G., Morris, S. L., Sawicki, M., Patton, D. R., Wirth, G., and Shepherd, C. W.: 1999, *The Astrophysical Journal* **518**, 533

Luppino, G. and Kaiser, N.: 1997, *The Astrophysical Journal* **475**, L20

Mandelbaum, R., Hirata, C. M., Broderick, T., Seljak, U., and Brinkmann, J.: 2005, *Submitted to MNRAS*

Maoli, R., Van Waerbeke, L., Mellier, Y., Schneider, P., Jain, B., Bernardeau, F., Erben, T., and Fort, B.: 2001, *Astronomy and Astrophysics* **368**, 766

Marinoni, C. and Hudson, M. J.: 2002, *The Astrophysical Journal* **569**, 101

McKay, T. A., Sheldon, E. S., Racusin, J., Fischer, P., Seljak, U., Stebbins, A., Johnston, D., Frieman, J. A., Bahcall, N., Brinkmann, J., Csabai, I., Fukugita, M., Hennessy, G. S., Ivezic, Z., Lamb, D. Q., Loveday, J., Lupton, R. H., Munn, J. A., Nichol, R. C., Pier, J. R., and York, D. G.: 2001, *e-print astro-ph/0108013*

Mellier, Y.: 1999, *Annual Review of Astronomy and Astrophysics* **37**, 127

Mellier, Y., Fort, B., and Kneib, J.-P.: 2003, *Astrophysical Journal* **598**, 102

Milgrom, M.: 2002, *New Astronomy Review* **46**, 741

Miyasaki, S. et al.: 2005, in Y. Mellier and G. Meylan (eds.), *Impact of Gravitational Lensing on Cosmology*, p. 57, IAU Symposium 225

Möller, O., Natarajan, P., Kneib, J.-P., and Blain, A. W.: 2002, *The Astrophysical Journal* **573**, 562

Moore, B., Ghigna, S., Governato, F., Quinn, G. L. T., Stadel, J., and Tozzi, P.: 1999, *The Astrophysical Journal* **524**, L19

Navarro, J. F. and Benz, W.: 1991, *The Astrophysical Journal* **380**, 320

Paczynski, B.: 1986, *Astronomical Journal* **304**, 1

Padmanabhan, T.: 1993, *Structure Formation in the Universe*, Cambridge University Press

Parker, L. C., Hudson, M. J., Carlberg, R., and Hoekstra, H.: 2005, *The Astrophysical Journal*

Peacock, J. A.: 1999, *Cosmological Physics*, Cambridge University Press

Perlmutter, S. et al.: 1999, *The Astrophysical Journal* **517**, 565

Postman, M. and Lauer, T. R.: 1995, *The Astrophysical Journal* **440**, 28

Refregier, A.: 2003, *Annual Review of Astronomy and Astrophysics* **41**, 645

Refregier, A. and Bacon, D.: 2003, *Monthly Notices of the Royal Astronomical*

Society **338**, 48

Refregier, A., Rhodes, J., and Groth, E. J.: 2002, *The Astrophysical Journal Letters* **572**, L131

Rhodes, J., Refregier, A., and Groth, E. J.: 2001, *The Astrophysical Journal Letters* **552**, L85

Rhodes, J., Refregier, A., and Grothe, E. J.: 2000, *The Astrophysical Journal* **436**, 790

Riess, A. G. et al.: 1998, *Astronomical Journal* **116**, 1009

Rines, K., Geller, M., Diaferio, A., Kurtz, M., and Jarrett, T.: 2004, *Astronomical Journal* **128**, 1078

Rubin, V.: 1983, *Science* **220**, 1339

Schechter, P. L.: 2005, in Y. Mellier and G. Meylan (eds.), *Impact of Gravitational Lensing on Cosmology*, p. 281, IAU Symposium 225

Schneider, P. and Rix, H.-W.: 1997, *The Astrophysical Journal* **474**, 25

Sheldon, E. S. et al.: 2004, *Astronomical Journal* **127**, 2544

Sheth, R. K., Bernardi, M., Schechter, P. L., Burles, S., Eisenstein, D. J., Finkbeiner, D. P., Frieman, J., Lupton, R. H., Schlegel, D. J., Subbarao, M., Shimasaku, K., Bahcall, N. A., Brinkmann, J., and Ivezić, Ž.: 2003, *The Astrophysical Journal* **594**, 225

Skordis, C., Mota, D. F., Ferreira, P. G., and Boehm, C.: 2005, *e-print astro-ph/0505519*

Smith, D. R., Bernstein, G. M., Fischer, P., and Jarvis, R. M.: 2001, *The Astrophysical Journal* **551**, 643

Somerville, R. S.: 2002, *The Astrophysical Journal* **572**, L23

Spergel, D. N. et al.: 2003, *Astrophysical Journal Supplement Series* **147**, 175

Springel, V. et al.: 2005, *Nature* **435**, 629

Springel, V., White, S. D. M., and Hernquist, L.: 2004, in *IAU Symposium*, p. 421

Tegmark, M. et al.: 2004, *The Astrophysical Journal* **607**, 655

Tinker, J. L., Weinberg, D. H., Zheng, Z., and Zehavi, I.: 2005, *The Astrophysical Journal* **631**, 41

Tucker, D. L. et al.: 2000, *The Astrophysical Journal Supplement* **130**, 237

Tyson, J., F. Valdes, F., Jarvis, J., and Jr., A. M.: 1984, *The Astrophysical Journal* **281**, L59

Tyson, J., R.A. Wenk, R. A., and Valdes, F.: 1990, *The Astrophysical Journal* **349**, L1

Valdes, F.: 1997, in G. Hunt and H. E. Payne (eds.), *Astronomical Data Analysis Software and Systems VI*, Vol. 125, p. 455, A.S.P. Conference Series

van den Bosch, F., Yang, X., and Mo, H. J.: 2004, in *Baryons in Dark Matter Halos*

van den Bosch, F. C., Yang, X., and Mo, H. J.: 2003, *Monthly Notices of the Royal Astronomical Society* **340**, 771

Van Waerbeke, L., Mellier, Y., Pelló, R., Pen, U.-L., McCracken, H. J., and Jain, B.: 2002, *Astronomy and Astrophysics* **393**, 369

Van Waerbeke, L., Mellier, Y., Radovich, M., Bertin, E., Dantel-Fort, M., McCracken, H. J., Le Fèvre, O., Foucaud, S., Cuillandre, J.-C., Erben, T., Jain, B., Schneider, P., Bernardeau, F., and Fort, B.: 2001, *Astronomy and Astrophysics* **374**, 757

Walsh, D., Carswell, R., and Weymann, R.: 1979, *Nature* **279**, 381

Weil, M. L., Eke, V. R., and Efstathiou, G.: 1998, *Monthly Notices of the Royal*

Astronomical Society **300**, 773

Weinmann, S. M., van den Bosch, F. C., Yang, X., and Mo, H. J.: 2005, *ArXiv Astrophysics e-prints*

White, S. and Frenk, C. S.: 1991, *The Astrophysical Journal* **379**, 52

White, S. and Rees, M.: 1978, *Monthly Notices of the Royal Astronomical Society* **183**, 341

Wilson, G., Kaiser, N., and Luppino, G. A.: 2001, *The Astrophysical Journal* **556**, 601

Wright, C. O. and Brainerd, T. G.: 2000, *The Astrophysical Journal* **534**, 34

Yee, H., Morris, S., Lin, H., Carlberg, R., Hall, P., Sawicki, M., Patton, D., Wirth, G., Ellingson, E., and Shepherd, C.: 2000, *The Astrophysical Journal Supplement* **187**, 425

Zhao, H., Bacon, D. J., Taylor, A. N., and Horne, K.: 2005, *e-print astro-ph/0509590*